ABSTRACT

Title of Dissertation: SYNTHESIS AND CHARACTERIZATION OF MULTIFERROIC THIN FILMS

Sung Hwan Lim, Doctor of Philosophy, 2008

Dissertation directed By: Professor Lourdes Salamanca-Riba and
Associate Professor Ichiro Takeuchi
Department of Materials Science and Engineering

Multiferroic materials and multiferroic materials systems which simultaneously exhibit ferroelectricity and magnetism have attracted great attention because of their exotic physical properties and their potential applications which utilize coupling of magnetism and ferroelectricity. The goal of this thesis was to study multiferroic materials systems in thin film and multilayer forms in order to explore the possibility of fabricating room temperature thin film devices.

In particular, we have focused on two types of multiferroic materials systems: 1) intrinsic multiferroic/magnetoelectric thin film materials and 2) magnetostrictive/ piezoelectric bilayer systems for investigation of the strain-mediated magnetoelectric (ME) effect.

$BiFeO_3$ is an intrinsic multiferroic which displays ferroelectricity and antiferromagnetism at room temperature, and thus of strong interest for ambient

device applications. In this thesis, we have extensively investigated the role of microstructure on the properties of $BiFeO_3$ thin films. We studied multiphase formation in Bi-Fe-O thin films, and found that formation of secondary phases such as α-Fe_2O_3, γ-Fe_2O_3, and Fe_3O_4 increased overall saturation magnetization and released the misfit strain of the $BiFeO_3$ grains in the films. We also observed large polarization in Bi-Fe-O thin films containing secondary phases that have almost fully relaxed the misfit strain.

We have studied several aspects of the ME effect which are directly relevant to possible novel device applications. Electric field tunable spintronic devices using the ME effect have been proposed. In one such device configuration, the desired effect is electric field tuning of giant magnetoresistance or tunnel magnetoresistance through control of exchange bias via the ME effect. We have investigated the feasibility of such a device using exchange-biased Co/Pt multilayers on Cr_2O_3 thin films.

The strain-mediated ME effect at the interface of magnetostrictive/ piezoelectric bilayers has been widely used to demonstrate magnetic field detection with extremely high sensitivity. Although the overall mechanism of such an effect is known, the details of the bilayer interfaces and how they affect the coupling is not understood. In order to directly observe the strain-mediated ME coupling effect, we fabricated bilayer thin film structures and performed in-situ dynamic observation of magnetic domains while an electric-field was being applied using Lorentz transmission electron microscopy. Electric-field induced motion of magnetic domain boundaries in the magnetostrictive layer was observed for the first time.

SYNTHESIS AND CHARACTERIZATION OF MULTIFERROIC THIN FILMS

By

Sung Hwan Lim

Dissertation submitted to the Faculty of the Graduate School of the
University of Maryland, College Park, in partial fulfillment
of the requirements for the degree of
Doctor of Philosophy
2008

Advisory Committee:

Professor Lourdes Salamanca-Riba, Chair / Advisor
Associate Professor Ichiro Takeuchi, Co-Advisor
Professor Manfred Wuttig
Assistant Professor John Cumings
Professor Richard Greene

Acknowledgements

I would like to express my sincere gratitude to my advisors, Prof. Lourdes Salamanca-Riba and Prof. Ichiro Takeuchi, for giving me the opportunity to work on exciting projects. I would especially like to thank both of them for their guidance and support throughout my Ph.D research at the University of Maryland. I have been working with Prof. Salamanca-Riba since the first year I came to the U.S. I benefited from her guidance in every aspect during my Ph.D study, including the discussions we held and intelligent suggestions she made regarding my research. I deeply appreciate all the time and effort she spent discussing my projects and advising me. I also appreciate all corrections to my papers and thesis, attentive consideration and encouragement she gave me. It would not have been possible to accomplish my scientific goals without her guidance. Also, the same gratitude goes to Prof. I. Takeuchi, who served as my co-advisor. It was a great honor to join his group and learn thin film synthesis and characterization. I have great respect for his knowledge and passion for research. He always encouraged me to go forward to achieve my academic goals.

I am also grateful for the insights and advice Prof. John Cumings shared with me. His suggestions and guidance were a great help for performing electron beam lithography and Lorentz TEM as related to the experiments in Chapter 5.

I would like to thank Prof. Manfred Wuttig for his kind assistance and advice on the theoretical calculations and understanding of the magnetoelectric coupling effect, also in Chapter 5.

I am also grateful to Prof. Samuel E. Lofland, Prof. Nagarajan Valanoor, Prof. Nigel Browning, and Prof. S. Sundar Manoharan for their valuable assistance in my research.

I would like to thank Prof. Richard Greene for taking time out of his busy schedule to serve on my committee and evaluate my work.

I would like to give my special acknowledgements to Dr. Todd Brintlinger as a collaborator. All the ideas we shared and discussed have proven very fruitful. Without his contribution this project would not have gone so well.

I would like to thank Dr. Makoto Murakami for his help and advice at the beginning of my studies. I would like to express my gratitude for the helping hands of my colleagues and collaborators: Anbusathaiah Varatharajan, Shenqiang Ren, Yi Qi, Volkan Ortalan, Dr. Daisuke Kan, Kamal Hussain Baloch, Dr. Ranjan K. Sahu, Dwight Hunter, and all other members in Prof. Takeuchi group and Prof. Salamanca-Riba group.

I would like to give my special thanks to Sheng-Yu Young and Kwan Lee as collaborators and also as best friends. All the help and cheer they showed have been very rewarding. All the friendship and delightful memories we share will be kept in my mind with the greatest care.

I especially appreciate my father, my mother, my brothers and my sisters for their understanding, encouragement, and endless love.

Finally, I want to thank my lovely wife, Mi-Sun Kim, and my son, Hyun-Bin Lim. I would never achieve anything without their deep love.

Table of Contents

List of Tables

List of Figures

List of Abbreviations

ME	Magnetoelectric
PLD	Pulsed laser deposition
PVD	Physical vapor deposition
FME	Flux-mediate epitaxy
P-E	Electrical polarization-electric field
I-V	Current-voltage
MOKE	Magneto-optical Kerr effect
VSM	Vibrating sample magnetometer
AFM	Atomic force microscopy
XRD	X-ray diffraction
TEM	Transmission electron microscopy
EDS	Energy-dispersive X-ray spectroscopy
EELS	Electron energy loss spectroscopy
EB	Exchange bias
MFC	Magnetic field cool
MEFC	Magnetic and electric field cool

Chemical Nomenclature

$BiFeO_3$	Bismuth ferrite
$SrTiO_3$	Strontium titanate
α-Fe_2O_3	Hematite
γ-Fe_2O_3	Maghemite
Cr_2O_3	Chromium oxide
FeGa	Iron gallium
$BaTiO_3$	Barium titanate

Greek Letters

2θ	Scattering angle
ε	Strain
σ	Stress
λ	X-ray wavelength
χ	Susceptibility,

Chapter 1

1. Introduction

1.1 Background

The focus of my study was fundamental materials science and device physics aimed at exploring possible room temperature device application of multiferroic/ magnetoelectric thin film materials and multiferroic composite thin films. I studied multiferroic properties of intrinsic multiferroic $BiFeO_3$ thin film which has a weak ferromagnetism and ferroelectricity at room temperature. I have explored the possibility of fabricating tunable spintronic devices using magnetoelectric Cr_2O_3 thin films which had been predicted to show electric-field tunable antiferromagnetism at temperatures near room temperature. I also studied direct observation of strain-mediated magnetoelectric (ME) coupling effect using multiferroic composite thin films.

Multiferroics are materials that exhibit two or three of the ferroic properties: ferroelectricity, ferromagnetism, and ferroelasticity.[1] *Ferroelectricity* is the phenomenon that involves electrical polarization. A ferroelectric material undergoes a phase transition from a high-temperature phase (paraelectric) state above the Curie temperature (T_C) to a low temperature phase (ferroelectric) that has a spontaneous polarization along a preferred direction. As electric field is applied, ferroelectric materials exhibit a saturation polarization (P_S) along the direction of the applied electric field. Once saturation is reached, remnant polarization (P_r) remains in the absence of an external electric field. This polarization direction can be reversed by

switching the external electric field. At the atomic scale, the existence or absence of ferroelectricity in an ionic material is determined by a balance between the short-range repulsions, which prefer the nonferroelectric (paraelectric) symmetric structure and long-range Coulomb forces, which prefer the ferroelectric state. The most widely studied and used ferroelectric materials are oxides with a perovskite structure, which has the form ABO_3. Ferroelectrics find a large range of applications, such as nonvolatile random access memories, capacitors, and transducers. Because many ferroelectrics also exhibit large electromechanical coupling, they are also widely used for piezoelectric applications.

Ferromagnetism is a phenomenon which involves spontaneous magnetization below a critical temperature. The spontaneous magnetization can be switched and saturated (M_s) along the direction of external magnetic field (H). There is a remanent magnetization (M_r) once the field is removed. The applications of ferromagnetic materials are strongly determined by the values of the remanent magnetization and coercivity (H_C). For example, a square-shaped hysteresis loop with high remanent magnetization and high coercive field is needed for permanent magnet applications, while materials with narrow hysteresis loops are needed for recording media.

Ferroelasticity is a phenomenon which involves a spontaneous deformation (ε). In ferroelastic materials, by applying a stress (σ) to a ferroelastic phase, a phase can be changed from one phase to an equally stable structure with different orientations, and this process involves formation motion of twin boundaries. This stress-induced phase change results in a spontaneous strain in the material. The shape memory effect and superelasticity are important phenomena which involve ferroelasticity.

The projects carried out in this thesis mainly focused on multiferroic materials in which ferroelectricity and ferromagnetism coexist. The *magnetoelectric (ME) coupling effect* is manifested in the control of spontaneous polarization by applying a magnetic field and/or control of spontaneous magnetization by applying an electric field. The multiferroic coupling effects are often related to strain in the materials. For example, coupling between ferroelectricity and ferroelasticity is known as piezoelectricity. Piezoelectricity gives rise to a change of polarization (P) by an applied stress (σ), or a change of strain (ε) by an applied electric field (E). Similarly, the coupling between ferromagnetism and ferroelasticity is called piezomagnetism, through which a change of strain can take place by an applied magnetic field, and vice versa. Also, this coupling is referred to as magnetostriction which corresponds to a change of strain as a quadratic function of the applied magnetic field.

Magnetoelectric materials which show ME coupling effects had been investigated earlier from the 1950s to 1970s.[4-6] However, recently there has been a surge of activities in this area because of discoveries of new materials and development of better understanding of the multiferroic properties. Magnetoelectric materials are also being pursued because the ability to couple the two order parameters (simultaneous ferroelectric and magnetic properties) allows an additional degree of freedom in device design.

All the magnetoelectric materials that have been studied to date can be classified into two categories: single phase multiferroics which show ferroelectricity and ferromagnetism simultaneously in one phase and multiferroic composites which are combinations of ferromagnetic and ferroelectric phases.

1.2 Intrinsic magnetoelectric materials and intrinsic multiferroic materials

There are various magnetoelectric materials and multiferroic materials. Magnetoelectric materials are not necessarily multiferroic since they can show the ME coupling effect without robust simultaneous presence of ferroelectricity. In 1960s, a linear magnetoelectric coupling coefficient was observed in Cr_2O_3, which is not a ferroelectric material.[11,12] In 1966, a boracite $Ni_3B_7O_{12}I$, which has weak ferromagnetic and weak ferroelectric ordering below 60 K was first used to demonstrate the magnetic reversing of electric polarization.[13]

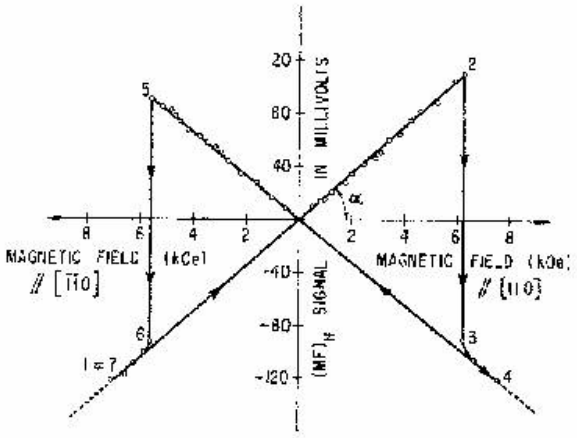

Figure 1.1 Example of magnetoelectric coupling in $Ni_3B_7O_{13}I$. The magnetoelectric $(ME)_H$ voltage signal (polarization) was reversed in a magnetic field (- 0.6 T < $\mu_0 H$ < 0.6 T) at 46 K.[13]

As shown in Fig. 1.1, a weak magnetic-field induced reversal of the magnetization was observed to flip the polarization. The magnetic field induced effect gave rise to switching of the polarization (~ 0.076 μCcm^{-2}), and the ME voltage

signal was flipped from about -100 mV to 100 mV by switching the magnetic field from -0.6 T to 0.6 T. These were some of the first investigation of ME effects.

Some of the more recently studied multiferroics include hexagonal rare-earth manganites with formula $MMnO_3$ (M = Y, Ho, Er, Tm, Yb, Lu, or Sc) which are intrinsic multiferroics which exhibit ferroelectricity and frustrated magnetic ordering.[14-17] The compounds $BaMF_4$ (M = Ho, Fe, Co, Ni) have an orthorhombic crystal structure at high temperatures with antiferromagnetic (weak ferromagnetic) ordering and antiferroelectric (ferro-electro-elastic) properties at low temperature.[18,19] Also, there are other perovskite multiferroic materials. A perovskite compound contains magnetic ions which fully (or partially) occupy the octahedral positions in the perovskite structure. For example, the compound $BiFeO_3$ has a rhombohedral, pseudoperovskite, structure with alternating layers of bismuth and oxygen and iron and oxygen. The octahedral positions contain Fe^{3+} ions which cause exchange interaction between the Fe^{3+} ions along the $Fe^{3+} - O^{2-} - Fe^{3+}$ chains (see Fig. 1.2).

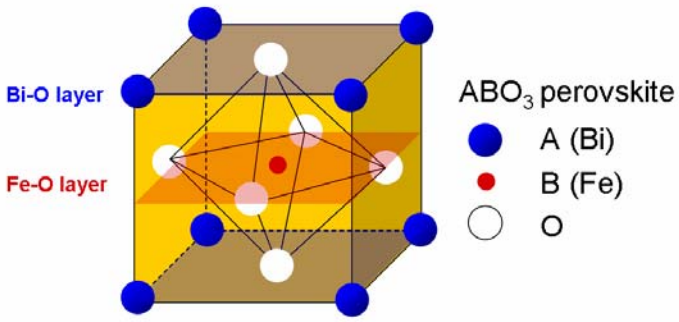

Figure 1.2 Schematic of the unit cell of $BiFeO_3$ which has the ABO_3 type perovskite structure.

Fig. 1.3 summarizes the occurrence of coexistence of ferromagnetism and ferroelectricity in a single phase. Figure 1.3(a) depicts a ferromagnet by a spin orientation of a charge and local magnetic moment m. Time reversal switches both the direction of orbit and moment, while spatial inversion leaves both orbit and moment unchanged. Figure 1.3 (b) represents ferroelectrics with local dipole moment P from asymmetrical displacement of positive and negative charges in the unit cell. Spatial inversion switches P, while time inversion shows no change. Fig. 1.3(c) represents multiferroics that have both ferroelectric and ferromagnetic properties with time reversal of magnetization and spin orbit and spatial inversion of polarization.

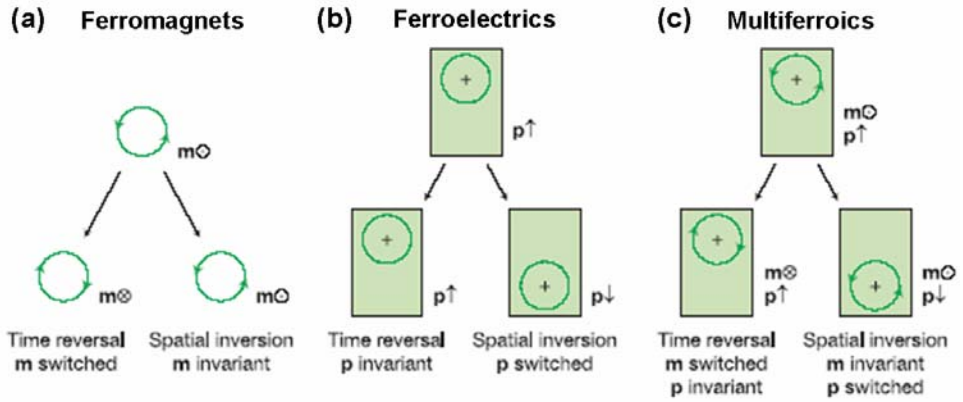

Figure 1.3 Time-reversal and spatial-inversion symmetry in multiferroic materials [W. Eerenstein, *et al.*, Nature 442, 17, 759 (2006)]

The possible coexistence of the spontaneous magnetization and polarization in the same phase does not contradict the general criteria for the appearance of ferromagnetism and ferroelectricity taken separately. Magnetic ordering is governed by the exchange interaction of the electron spins, while ferroelectric ordering is

governed by the redistribution of charge density in the lattice. However, a limited number of multiferroics exist in nature, or have been synthesized in the laboratory, and the reasons for the scarcity of ferromagnetic/ferroelectric coexistence has been explored by *Nicola A. Hill*.[7] She found that, in general, the *d* electrons in transition metals, which are essential for magnetism, reduce the tendency for off-center ferroelectric distortion. Consequently, an additional electronic or structural driving force must be present for ferromagnetism and ferroelectricity to coexist. In addition to the fact that such materials are rare, these materials exhibit multiferroic properties and magnetoelectric coupling at low temperatures (below room temperature) reducing the feasibility for practical applications. For example, $TbMn_2O_5$ is an intrinsic multiferroic material which shows magnetism-induced ferroelectricity and switchable polarization with magnetic field, but its polarization is very small (~ 80 $nCcm^{-1}$) and it is at a very low temperature (3 K).[8]

Single crystal $BiFeO_3$ has been known as an intrinsic multiferroic material which is a canted antiferromagnet (weak ferromagnetism) below its Néel temperature (T_N = ~ 640 K), and a ferroelectric below its Curie temperature (T_C = ~ 1100 K). However, recently a remarkable discovery has been reported in this material by J. Wang *et al.*[20] They found significant increase in its magnetization and electrical polarization in thin film structures of $BiFeO_3$, which make them a strong candidate for room-temperature operated multiferroic device applications. In thin film structures, P_S as high as ~ 55 $\mu C/cm^2$ was observed, compared to ~ 3.5 $\mu C/cm^2$ observed in single crystals earlier. In Wang's thin film materials, M_S was also found to be as high as 150 emu/cc at room temperature compared to ~ 2 emu/cc in single crystals.[21-24]

In subsequent reports, the misfit strain in the film induced from the lattice mismatch with the substrate as well as structural distortions from the transformation of rhombohedral to tetragonal crystal structures in $BiFeO_3$ thin films were attributed to as the dominant reason for enhancements of both ferroelectric and ferromagnetic properties.[20] However, clear evidences for the origin of increased intrinsic magnetization and polarization were not found. The observed properties were often not reproducible, and there had been a number of reports on the properties of $BiFeO_3$ thin films with conflicting results.

In the present study, we have studied the origin of enhanced ferromagnetism and ferroelectric properties in $BiFeO_3$ thin films. The results are presented in Chapter 3. To understand the enhancement of ferromagnetism, we studied multiphase formation in Bi-Fe-O thin film. We found that formation of secondary phases such as α-Fe_2O_3, γ-Fe_2O_3, and Fe_3O_4 takes place at relatively high growth temperature at lower oxygen pressure. The formation of ferromagnetic γ-Fe_2O_3 and Fe_3O_4 increased the overall saturation magnetization of the Bi-Fe-O thin films.

To understand the large polarization reported in $BiFeO_3$ films, we investigated the columnar structure of $BiFeO_3$ and Fe_2O_3 which showed large polarization and found that misfit strain in these films is remarkably relaxed by the formation of Fe_2O_3. Our results suggest that the origin of large polarization of the $BiFeO_3$ films is not misfit strain in the thin film structure (as had been reported prior to this study) but that it is an intrinsic property of $BiFeO_3$. To better understand the role of strain and grain size on domain switching, we also studied the ferroelectric properties of polycrystalline $BiFeO_3$ thin films grown at relatively low temperatures. These films

are less sensitive to misfit strain from the substrate and possess less impurities and defects due to the relatively low growth temperature. In these polycrystalline $BiFeO_3$ thin films, large polarization and effective switching of ferroelectric domains were observed in the films with nano-sized grains. The effect of grain size on ferroelectric properties and annealing effect was investigated. These results are presented in Chapter 3.6.

We have also explored tuning of the structural, electrical and magnetic properties in $BiFeO_3$ thin films. In order to improve the crystallinity of the films, the flux-mediate epitaxy method (FME) was introduced. Using the FME method, single crystal-like thin films with large grains and atomically smooth surface were synthesized. These films showed improvement of the dielectric properties compared to regular films. Also, phase transformation from antiferromagnetic α-Fe_2O_3 to ferromagnetic γ-Fe_2O_3 by annealing at hydrogen atmosphere was investigated in order to explore tuning of the ferromagnetic properties in films containing columnar structure of $BiFeO_3$-Fe_2O_3.

A possible device application of magnetoelectric materials using exchange bias is discussed in Chapter 4. Novel memory devices, magnetic read-head, and magnetic field sensors have been suggested as possible applications of the ME effect. In the memory device schemes, ferroelectric and ferromagnetic random access memories can be combined which can result in an increase in memory storage ability and functionalities. In the magnetic field sensor application, the modulation of electrical polarization is utilized, and this effect had been found to show extremely high sensitivities.

Magnetic read-head and some sensor schemes are based on giant magnetoresistance (GMR)[43-46] or tunnel magnetoresistance (TMR) effects[47], which show change of resistance when the magnetic configuration between two neighboring ferromagnetic layers is modified. Typically, one magnetic layer is pinned through exchange bias by an adjacent antiferromagnetic layer. Recently, there has been a growing interest in a direct method for magnetization reversal including spin transfer from spin-polarized current in the device.[48,49] An alternative is to combine GMR or a TMR device with a magnetoelectric thin film where the ME thin film is used as the antiferromagnetic pinning layer providing exchange bias.[50] In such a ME spintronic device, antiferromagnetic ordering in the ME thin film is not affected by a moderate external magnetic field. However, the magnetic configuration of a spintronic device can be tuned in the presence of an applied electric field by changing the antiferromagnetic property of the ME thin film layer. In theory, the magnetoresistance can then be controlled by changing the antiferromagnetic property of the ME thin film which in turn tunes the exchange bias to the adjacent ferromagnetic layer.

One embodiment of such a device scheme is depicted in Fig. 1.4. Here, the magnetic properties of ME layer are controlled by an applied voltage. This layer controls switching of the bottom ferromagnetic pinned layer. This in turn controls the magnetoresistance behavior of the device.

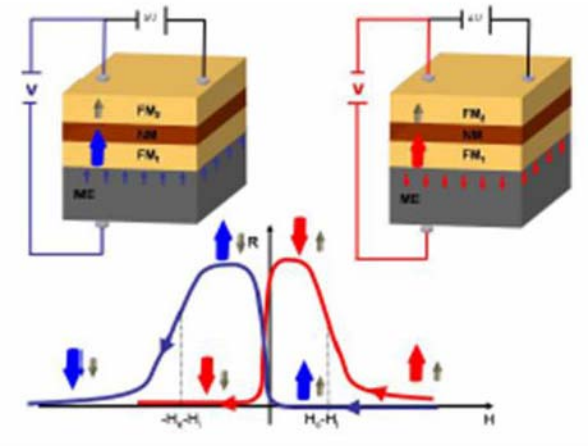

Figure 1.4 Schematic of a GMR device and its magnetoresistance curve involving an ME film as a pinning layer. Blue and red represent two states (of applied voltage).[119]

To explore the possible occurrence of such an effect, we have investigated the behavior of exchange coupled Co/Pt multilayers on Cr_2O_3 thin films. The idea is to see if we can observe tunable exchange bias using the ME coupling. We used Cr_2O_3 instead of $BiFeO_3$, because the ME coupling effects have not been unambiguously established to date in $BiFeO_3$, while Cr_2O_3 is well known as the first material which showed the magnetoelectric coefficient.[11,12] We achieved an extremely smooth interface between Co/Pt and the Cr_2O_3 layer (RMS ~ 0.3 nm) and applied a sufficiently high electric field of 77 MV/m after the structure is field cooled through the Néel temperature of Cr_2O_3 (T_N = 308 K). This electric field value is ~ 150 times higher than the applied field on an earlier reported exchange biased Cr_2O_3 single crystal experiment.[109] Despite the high quality of our samples, the thin film device exhibited no significant ME effect on exchange bias with in the measured sensitivity range even at the high electric field. We discuss the possible reasons for this null observation in Chapter 4.

Using the CoPt/Cr_2O_3 device configuration, we found an efficient technique for controlling the exchange bias field and its sign by sweeping a magnetic field with offset during cooling. We found that the sign of the exchange bias and the shape of the hysteresis loops, i.e. single/dual hysteresis loop of the out-of-plane magnetized Co/Pt layers can be delicately controlled by adjusting the magnetic field during cooling through the Néel temperature of Cr_2O_3.

1.3 Composite multiferroic materials

As mentioned above, intrinsic (single phase) multiferroics are relatively rare in nature, and a weak ME coupling effect usually can only be observed at low temperatures and high magnetic fields. In contrast, artificial multiferroic materials can be achieved by synthesis of multiferroic composites which consist of a ferroelectric (piezoelectric/electrostrictive) phase and a ferromagnetic (piezomagnetic/magnetostrictive) phase, and these two parameters are coupled via strain mediation at their interface as schematically shown in Fig. 1.5.[9,25]

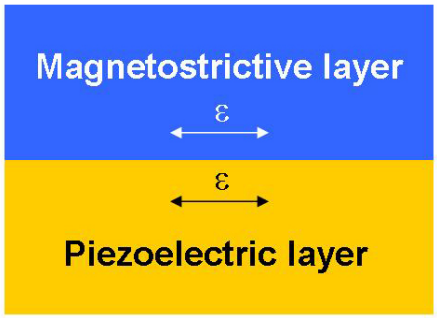

Figure 1.5 Schematic of a multiferroic composite for strain-mediated ME coupling.

In such a geometry, the distortion of the magnetostrictive phase by an applied magnetic stimulus is transferred to the piezoelectric phase and results in an electrical response. Conversely, by applying an electric stimulus, a magnetic response can be generated in the magnetostrictive layer. Such multiferroic composites[26] can be achieved in the form of laminates,[27,28] or epitaxial multilayers.[29] To date, $CoFe_2O_4$, $NiFeO_3$, Terfenol-D, and $La_{1-x}Sr_xMnO_3$ have been used for the ferromagnetic phase, and $BaTiO_3$, $Pb(Zr,Ti)O_3$ (PZT), $BiFeO_3$, $PbTiO_3$ have been used for the ferroelectric phase.[30-36] The magnetoelectric coefficient (α_{ME} = dP/dH) in PZT /Terfenol-D composite material was found to be as high as 2 $Vcm^{-1}Oe^{-1}$ = 5×10^{-8} sm^{-1} (or $Cm^{-2}Oe^{-1}$).[10] In a $La_{0.67}Sr_{0.33}MnO_3$ / $BaTiO_3$ system, the converse effect was observed with $\mu_0(dM/dE) = 2.3 \times 10^{-7}$ sm^{-1}.[41] These values are substantially larger than the highest ME coefficient observed in single-phase magnetoelectric material, Cr_2O_3 (α_{ME} = dE/dH = 0.01 $Vcm^{-1}Oe^{-1}$ = 2.67×10^{-12} sm^{-1} at near Néel temperature of 307 K)[37, 40].

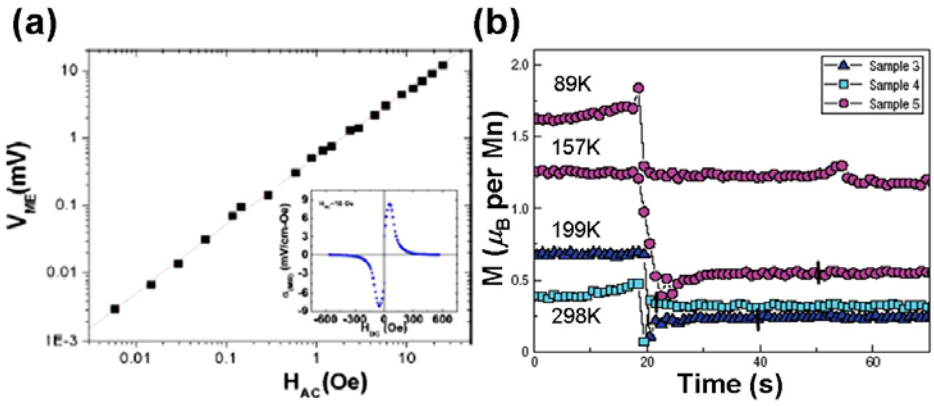

Figure 1. 6 (a) Induced voltage by an applied ac magnetic field on an ME sensor (metglas + polyvinylidene fluoride).[41] The inset shows a calibration scan of a ME device. (b) Large sharp change of magnetization measured by VSM due to an applied electric field in $La_{0.67}Sr_{0.33}MnO_3$-$BaTiO_3$.[42]

Fig. 1.6 (a) and (b) show methods for measuring ME effects using multiferroic composites. Using a piezoelectric polyvinylidene fluoride (PVDF) layer and a magnetostrictive metglas layer, J. R. Hattrick-Simpers *et al.* measured voltage in the polyvinylidene layer induced by an applied magnetic field [Fig. 1.6 (a)].[41] The slope of the curve indicates that the sensor has a sensitivity of 467 μV/Oe over an ac field range of $10^{-6} \sim 10^{3}$ T. In Fig. 1.6(b), W. Eerenstein et al. measured the change of magnetization using a vibrating sample micrometer (VSM) during the application of an electric field (6 $kVcm^{-1}$) on a $La_{0.67}Sr_{0.33}MnO_3/BaTiO_3$ heterostructure. After applying an electric field to the unpoled $BaTiO_3$ substrate, the population of 90 ^{o} domains was altered due to displacement of the Ti cation in the $BaTiO_3$ unit cell as determined from the X-ray diffraction spectra (not shown), and the sharp switching of magnetic moments was observed by applying an electric field on the sample.[42] While such structures are beginning to be common for exploring strain-mediated ME devices, the details of the state of the interface between the two layers are not well understood. In fact, it is generally accepted that the formation of the interface which shows good coupling effect is non-trivial and the mechanism of the coupling through a typically used adhesive agent such as silver paste is not understood.

There had been no direct and dynamic visual observations of strain-mediated ME coupling effect because such a study is non-trivial. In Chapter 5, we describe the direct observation of strain-mediated ME coupling using in-situ Lorentz transmission electron microscopy (TEM) in an unconstrained double layer of ferromagnetic iron gallium (Fe-Ga) and ferroelectric barium titanate ($BaTiO_3$) film. The bilayer coupling is due to the natural adhesion of room temperature deposited Fe-Ga layer on the

$BaTiO_3$ thin film. The strain propagation, domain boundary movement, and reversible switching of magnetic domains in the ferromagnetic layer were dynamically observed by applying an electric field to the ferroelectric layer in Lorentz TEM.

Chapter 2

2. Experimental Approach

To synthesize the films investigated in the work, pulsed laser deposition (PLD) was used. X-ray diffraction (XRD) and transmission electron microscopy (TEM) were used for structural analysis. Atomic force microscopy (AFM) and secondary electron microscopy (SEM) were used to investigate surface morphology such as roughness and/or grain size. The magnetic properties were measured using a vibrating sample magnetometer (VSM), a magneto-optical Kerr effect (MOKE) set-up, and a superconducting quantum interference device (SQUID). The electrical properties were measured using an RT6000 test system, and HP 4192 impedance/gain analyzer

2.1 Thin film fabrication

For the thin film fabrication, pulsed laser deposition (PLD) was used for the growth of the oxide thin films, and physical vapor deposition (PVD) was used for the growth if the magnetic or conducting metal thin films. As shown in Fig. 2.1, a PLD system includes a laser source such as an ArF, KrF, or XeF excimer laser or a Nd:YAG laser, an optical system which contains an aperture, a mirror, and a focusing lens. It also includes a vacuum chamber which has a heater, a heating stage, a rotating target holder, and a moving shadow mask inside. For this study, a KrF excimer laser

with a 248 nm wavelength and 30 ns pulse width was used. During the deposition process, the pulsed laser beam is focused onto a target to increase the laser energy density (energy/unit area at target surface) by a focusing lens. Typically the laser energy is in the range between 0.01 to 1.2 J at a frequency of 1 – 20 Hz during deposition. The focused laser beam which has higher energy than the ablation threshold value dissociates and ablates the target material and forms a plasma plume. The plume is directed normal to the target surface and collected on the heated substrate. High film quality can be achieved through the optimization of deposition parameters which include substrate temperature, base pressure, deposition gas pressure, laser energy density, and frequency. For the deposition of oxide thin films, oxygen must be introduced into the chamber in order to assist in the formation of the desired phase and obtain the correct film composition. The most important advantage of PLD is its versatility. Using the PLD technique, various materials such as oxides, semiconductors, and polymers can be easily grown. In general, the conditions are optimized to achieve stoichiometric transfer of the target composition to the film. Another advantage of PLD is the easy optimization process compared to other deposition techniques. Because of the short duration and high energy of the laser pulse, the target material plume is directed toward the substrate and different elemental components can have similar deposition rates, which help to make films with the same composition as the target. Also, PLD can be used to make multilayer structures by using multiple targets. PLD is primarily used in research laboratories to investigate new materials onto relatively small area substrate (up to 1 cm × 1 cm) because the highly directional plume makes it difficult to obtain uniform films over a large area.

In a combinatorial PLD chamber (Fig 2.1), the most important feature is the moving shadow mask located in front of a sample stage which allows the growth of films with gradients in the composition and/or thickness. The mask has a 10 × 10 mm square hole which is typically the same size as most commercial oxide substrates. By moving the shadow mask to cover and expose the substrate to the deposition plume, each position in the sample can have different exposure time to the plume, and this results in continuously varied compositions across one sample. Such a sample is called a composition spread. Also using a single target, one can easily make samples with a thickness gradient which is a very useful technique to study microstructural evolution during film growth or the change of physical properties as a function of heteroepitaxial constraint.

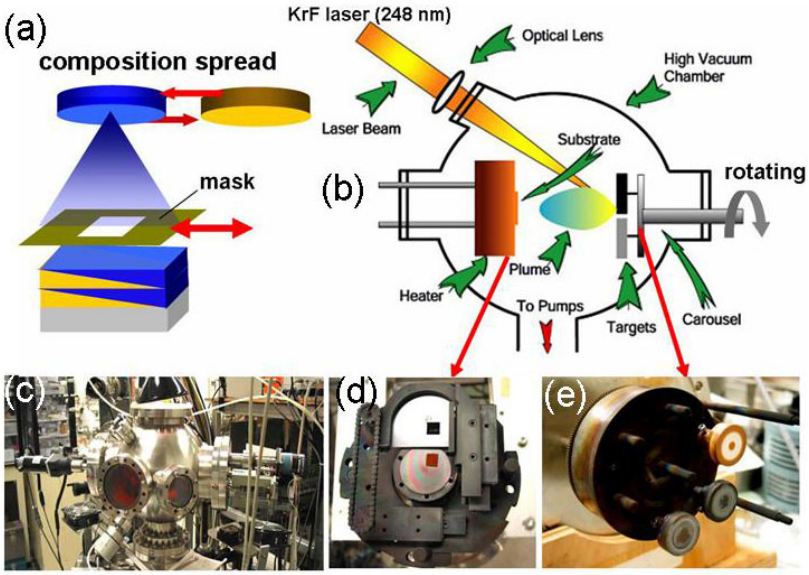

Figure 2.1 Schematics of (a) combinatorial pulsed laser deposition and (b) PLD system, which consists of (c) the chamber, (d) moving shadow mask, sample stage, and (e) multiple target stage.

2.2 Characterization techniques

2.2.1 Transmission electron microscopy (TEM)

In this thesis, transmission electron microscopy (TEM) was performed extensively to characterize the microstructure of the films. The morphological, crystallographic features as well as chemical information in the films have been obtained using TEM. The microscopes that were used in this study include a JOEL 4000FX TEM operated at 300 KV, a JEOL 2100F field emission TEM and a JEOL 2100 LaB_6 TEM operated at 200 KV.

A TEM operates similarly to an optical microscope, except that optical microscopes use light sources and focus light beams with glass lenses, while TEMs use electron sources and focus electron beams with electromagnetic lenses. The electrons emitted from the filament are accelerated by a high voltage (100 kV – 1000 kV) and focused through a set of condenser lenses onto the specimen. The electron beam is scattered by the specimen. The diffracted beams are then brought to focus by the objective lens on its back focal plane and form a diffraction pattern. A final TEM image or diffraction pattern can be produced on a fluorescent viewing screen by a series of objective lens, intermediate lens and projector and magnifying lenses. The main imaging and diffraction techniques include: 1. conventional imaging (bright-field and dark-field TEM); 2. electron diffraction (selected area electron diffraction, SAD); 3. convergent-beam electron diffraction (CBED); 4. phase-contrast imaging (high-resolution TEM, HRTEM); and 5. *Z*-contrast imaging. Besides diffraction and

spatial imaging, the high-energy electrons in TEM cause electronic excitations of the atoms in the specimen. Two important spectroscopic techniques make use of these excitations, i.e. energy-dispersive x-ray spectroscopy (EDS) and electron energy-loss spectroscopy (EELS). In this study, the conventional bright-field and dark-field imaging, SAD, and HRTEM are used to study the microstructures and EDS and EELS are used to study the chemical compositions of the films.

2.2.2 Lorentz transmission electron microscopy (LTEM)

We can also use TEM to study magnetic materials. If a sample is in-plane magnetized and has magnetic domains, the electron beam will feel a Lorentz force from the magnetic domains as it propagates through the sample. This force results in change of electron beam path. This deflection in the beam path allows the observation of magnetic domain by detecting the tilting of the electron beam. However, the electron beam can only be tilted by the component of the magnetic moments aligned perpendicular to the electron beam. Therefore, we can only see magnetic domains which are aligned along the in-plane direction in the thin film.

However, there is a limitation for magnetic domain observation in TEM. To tilt the electron beam and magnify the image, magnetic lenses are used in a TEM. To obtain relatively high magnification, the objective lens, which is the nearest lens to the sample, has to be used. However, when the objective lens is turned on, a few tesla of magnetic field along the out of plane direction is applied in the region where the sample is. This strong field results in switching of magnetic domains along the beam

direction. Therefore, we cannot see the magnetic domains at high magnification. Consequently, in Lorentz TEM, there is an upper limit in the magnification that can be used to observe magnetic domains. This magnification does not use the objective lens and only utilizes the lenses in low magnification mode.

As shown in Figure 2.2, there are two different methods to observe magnetic domain structures. One is called Fresnel imaging and the other is Foucalt imaging. In the Fresnel mode, by adjusting the focal length between under focus and over focus, the domain boundaries have more or less electron density and will appear as alternating dark and bright lines (by Lorentz force) in the TEM image [Fig. 2.2 (a)]. The contrast of the domain boundaries reverses as we change from underfocus to overfocus. In the Foucault imaging mode [Fig. 2.2 (b)], by selecting the tilted beam in the diffraction pattern using an aperture, one can obtain a dark field image of four differently oriented (± x, ± y) domains. Also in Lorentz TEM, one can apply a magnetic field along the in-plane and out-of-plane direction by tilting the sample and increase the current though the objective lens.

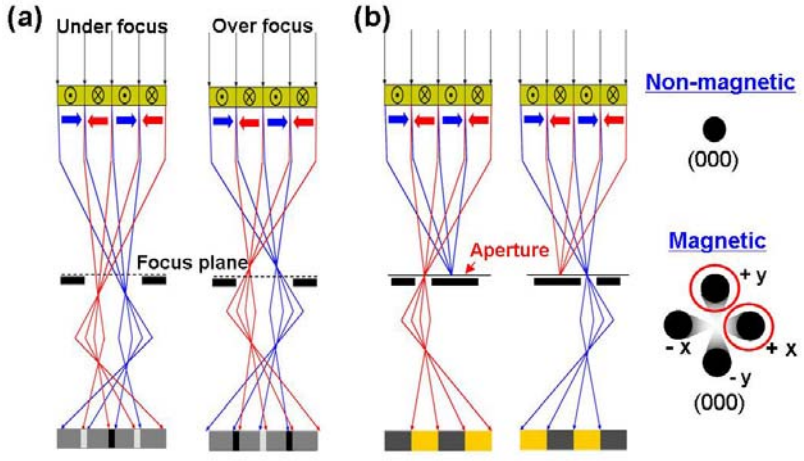

Figure 2.2 Two different methods to observe magnetic domains in Lorentz TEM. Schematics for Fresnel imaging (a) and Foucault imaging (b).

2.2.3 Atomic force microscopy (AFM)

AFM was also used to evaluate the surface morphology by measuring the forces between a cantilever tip and the sample surface. The atomic force microscope (AFM) has become a very important characterization tool in many fields since G. Binnig and co-workers invented it in 1986. The AFM scans over a surface by using a fine ceramic or semiconductor tip. Typically, the tip is located at the end of a cantilever with a laser beam focused at the end of the cantilever. As the tip is either repelled by or attracted to the sample surface, the cantilever deflects which results in a change of the laser beam position on a photodiode (see Figure 2.3). The photodiode detects the relative position of the laser on the photodiode face. The photodiode is composed of two major parts which separately detect normal motions and shear motions. The top half and bottom half of the photodiode detect normal and shear motions, respectively by the laser displacement along the x axis of the photodiode. A plot of the laser deflection versus tip position in the x, y, and z directions on the sample surface provides 2 or 3 dimensional surface images. A sensitive piezoelectric element controls the position and motion of the tip over the surface of the substrate.

There are three different modes in AFM. These are the contact mode, the non-contact mode, and the tapping mode. In the contact mode, the tip responds to Coulomb forces with the surface. An image of the surface topography is obtained by tracking the deflection of the cantilever as it is scanned over the surface. Maintaining the same force between tip and sample maintains the same distance between the tip and the surface. The Hooks law and Coulomb forces can be written, respectively.

$$F_H = -kx\,, \qquad \text{(}Hook\text{'s Law)}$$

$$F_C = \frac{q_1 q_2}{4\pi\varepsilon_0 r^2}\,, \qquad \text{(}Coulomb\text{ force)}$$

where k represents the elastic (spring) constant and q_1, q_2 are the charges of the tip and the sample and r is the distance between the charges. However, in the contact mode, the tip can cause damage to the sample. So the non-contact mode was developed to investigate samples with soft surfaces. In the non-contact mode, the AFM tip is held at a distance in the range 3-15 nm above a surface of the sample, and this distance is maintained constant by using the force signal. As the tip is scanned over a sample surface, long range attractive forces acting between the tip and the sample are detected, and a topographic image is recorded.

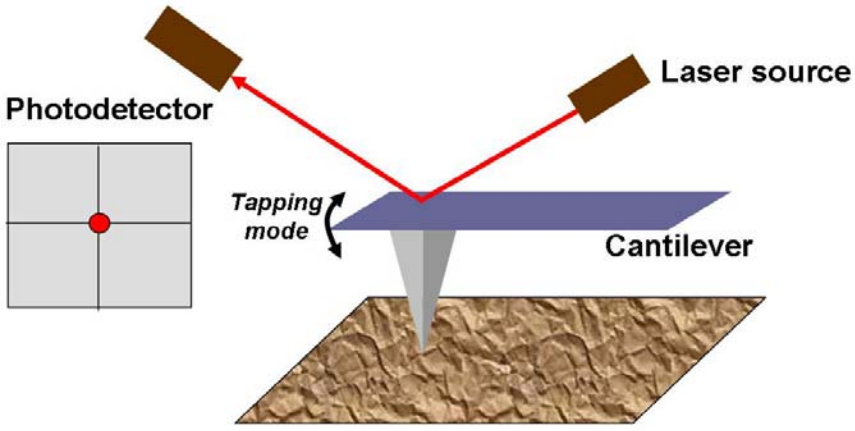

Figure 2.3 Schematic of an Atomic Force Microscope

In the non-contact mode, AFM measures van der Waals forces from the vibrating tip at a resonance frequency with nano-scale amplitude by detecting the change of amplitude. However, in the non-contact mode the data could be inaccurate due to weak van der Waals forces. Therefore, the tapping mode, another method, was

developed and has come to enjoy widespread use. This mode has advantages over the two modes mentioned above. In this method, the tip vibrates at a resonance frequency with an amplitude of 20 – 100 nm and taps the surface and detects the change of frequency due to the Coulomb force. A cantilever is oscillated at its resonant frequency and is in contact with a surface for only a very small fraction of its oscillation period.

In our experiments, AFM was also used to measure magnetic and electrical properties. To measure the electrical properties, the tip detects the piezoresponse from the surface of a ferroelectric material. This technique is called piezo force microscopy (PFM). In the PFM mode, an external voltage with a frequency ω is applied through the tip, which causes the ferroelectric sample under the electric field to vibrate at the same frequency due to the converse piezoelectric effect. This vibration then forces the AFM tip to oscillate, and the modulated deflection signal is detected using a lock-in amplifier. Using PFM, we can obtain quantitative values of d_{33} from the strain loop as a function of applied voltage as well as piezoelectric imaging. Also, using a magnetic tip, AFM can map local magnetization near the sample surface. This technique is known as magnetic force microscopy (MFM). In the MFM mode, magnetic domains are imaged from the contour of the magnetic force.

2.2.4 Magnetic and electrical properties measurements

Magnetic properties were also measured by a vibrating sample magnetometer (VSM) and a superconducting quantum interference device (SQUID) magnetometer.

In VSM, a sample is placed in a homogenous magnetic field, and then a magnetic moment is induced in the sample. If this sample is made to undergo a sinusoidal motion, the vibration induces a magnetic flux change. This in turn induces a voltage in a set of pick-up coils. So the magnetic moment determined by a VSM is related to the magnetization of the sample by its susceptibility.

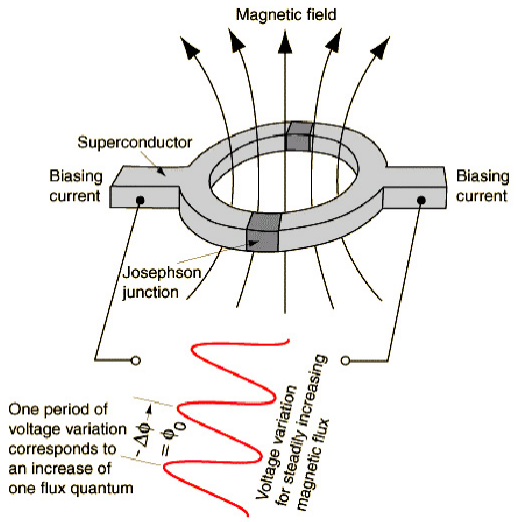

Figure 2.4 A SQUID device, which consists of two superconductors separated by thin insulating layers to form two parallel Josephson junctions.

The SQUID is the most sensitive device which can detect magnetic flux with sensitivity as high as ~ 10^{-14} T in terms of magnetic field. A SQUID consists of a Josephson junctions which have two superconductors separated by a thin insulating layer and acts as a flux-to-voltage transducer (schematically shown in Fig. 2.4).

For the electrical properties measurements, polarization – electric field (P-E) hysteresis loops were performed using a Radiant Precision LC ferroelectric probe station. An HP 4275A impedance/gain analyzer was also used to measure the dielectric properties.

Chapter 3

3. Multiphase formation in Bi-Fe-O thin films

3.1 Introduction

Although $BiFeO_3$ has the advantage that its magnetic and ferroelectric transitions are above room temperature, the small magnetization (from canted antiferromagnetism) and significant leakage current density are significant problems for practical applications. In addition, the high volatility of bismuth gives rise to bismuth deficient impurity phases and results in a narrow growth window for pure stoichiometric $BiFeO_3$. In the Bi-Fe-O system, there are several phases of different structures, compositions, and electrical and magnetic properties which can co-exist.[51,52] The presence of these phases can substantially affect the structural, electrical and magnetic properties of the overall material. This chapter presents growth conditions that give rise to multiphase formation and the effect of secondary phases on the properties of $BiFeO_3$ films. Films grown at low oxygen partial pressure show the canted antiferromagnetic phase α-Fe_2O_3 embedded in a matrix of $BiFeO_3$. The ferromagnetic phase, γ-Fe_2O_3 is found to precipitate inside the α-Fe_2O_3 grains. The magnetization of the Bi-Fe-O films is controlled by the presence of the γ-Fe_2O_3 phase.

The formation of these phases not only changes the magnetic properties of the films, it also reduces the misfit strain. The precipitation of α-Fe_2O_3 regions within the $BiFeO_3$ film reduces the compressive stress due to the smaller volume of α-Fe_2O_3

compared to that of $BiFeO_3$. These stain accommodation mechanisms affect the electrical properties such as leakage current and electrical polarization.

3.2 Oxygen pressure dependent multiphase formation

We have studied the coexistence of $BiFeO_3$ and Fe_2O_3 phases (α and γ) with a systematically varying degree of mixture controlled by the oxygen partial pressure during deposition. In order to fabricate bismuth iron oxide thin films by pulsed laser deposition, we used a stoichiometric $BiFeO_3$ target and $SrTiO_3$ (STO) (001) as the substrate, and the oxygen pressure was varied in the range of 0.025 – 100 mTorr while the temperature was kept at 650 ^oC.

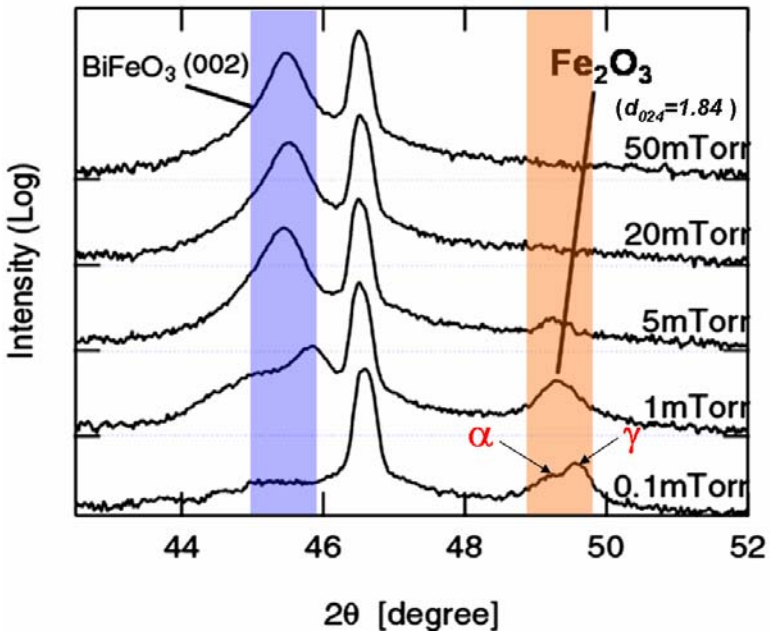

Figure 3.1 XRD spectra from $BiFeO_3$ films grown at different deposition oxygen pressures.

Figure 3.1 shows x-ray diffraction (XRD) spectra of a series of bismuth iron oxide thin films deposited under different oxygen pressures. Epitaxial and pure $BiFeO_3$ films were obtained at oxygen pressures higher than 5 mTorr, and the intensity of the (002) diffraction peaks of the $BiFeO_3$ increases as the pressure increases. At the oxygen pressure of 20 mTorr, single phase $BiFeO_3$ shows a monoclinically distorted (by about 0.5°) tetragonal structure. The lattice constants of the $BiFeO_3$ calculated from electron diffraction data (not shown) are a = 0.394 nm, c = 0.398 nm. As the oxygen pressure is reduced below 5 mTorr, peaks corresponding to the Fe_2O_3 phases [(012) of α-Fe_2O_3 and (024) of γ-Fe_2O_3] appeared, and the intensity of these peaks increases as the oxygen pressure decreases. This transition in the dominant phase reflects the change in the amount of Bi incorporation in the films due to the high volatility of Bi.

Fig. 3.2 shows TEM images of 200 nm thick bismuth iron oxide thin films grown at a low oxygen partial pressure. $BiFeO_3$ and Fe_2O_3 phases were found to have grown epitaxially with respect to the substrate as well as with respect to each other in the lateral direction in a columnar manner. We have found that the Fe_2O_3 domains grow with a mixture of α and γ phases, with α being the predominant phase. Fig. 3.2 (a) is a cross-sectional bright field image of a film showing the presence of $BiFeO_3$ and α-Fe_2O_3. This film was grown at 1 mTorr oxygen partial pressure. The corresponding SAD pattern from the sample was identified as the superposition of the (100) pattern from $BiFeO_3$ and that of the rhombohedral crystal structure of α-Fe_2O_3 (space group: $R\bar{3}c$) with lattice constants of $a = b$ = 0.505 nm, c = 1.319 nm, which are in good agreement with the published structure (i.e. JCPDS #33-0664). We have

also confirmed this result with energy dispersive x-ray spectroscopy (EDS). The epitaxial relationship of $BiFeO_3$ and α-Fe_2O_3 was determined from the electron diffraction patterns of the cross-sectional view (not shown here) and the plan view (Fig. 3.2 (c)): $[001]_{BiFeO3}$ is seen to be almost parallel (within 0.2°) to $[001]_{STO}$ (corresponding to the out-of-plane direction). However, [012] of α-Fe_2O_3 deviates by 2.1° from $[001]_{BiFeO3}$. Fig. 3.2 (b) is a plan view TEM image taken from the same sample grown at 1 mTorr. The interface between $BiFeO_3$ and α-Fe_2O_3 is parallel to the $[10\bar{2}]$ and $[1\bar{1}2]$ directions of α-Fe_2O_3 [see Fig. 3.2 (b)]. From the electron diffraction patterns, $[100]_{BiFeO3}$ is seen to be almost parallel to $[100]_{STO}$ (corresponding to the in-plane direction), with the in-plane lattice parameters of 0.394 nm and 0.3905 nm, respectively (see Fig. 3.2 (d)). However, $[10\bar{2}]$ of α-Fe_2O_3 makes an angle of ~2.1° with respect to the $[100]_{BiFeO3.}$ The measured interplanar distance between (000) and $(10\bar{2})$ of α-Fe_2O_3 is 0.370 nm, which is slightly larger than a published result (0.3684 nm, JCPDS #33-0664) for bulk α-Fe_2O_3. These results can be explained as a consequence of an in-plane tensile stress imposed by bismuth iron oxide on the α-Fe_2O_3. The increase of the $(10\bar{2})$ interplanar distance gives rise to a decrease in the (012) interplanar distance, which was measured as 0.364 nm. The lattice mismatch strain between $BiFeO_3$ and α-Fe_2O_3 is 6.4 %. After relaxation, a residual strain of 4.9 % in the Fe_2O_3 regions was calculated from our TEM and XRD results.

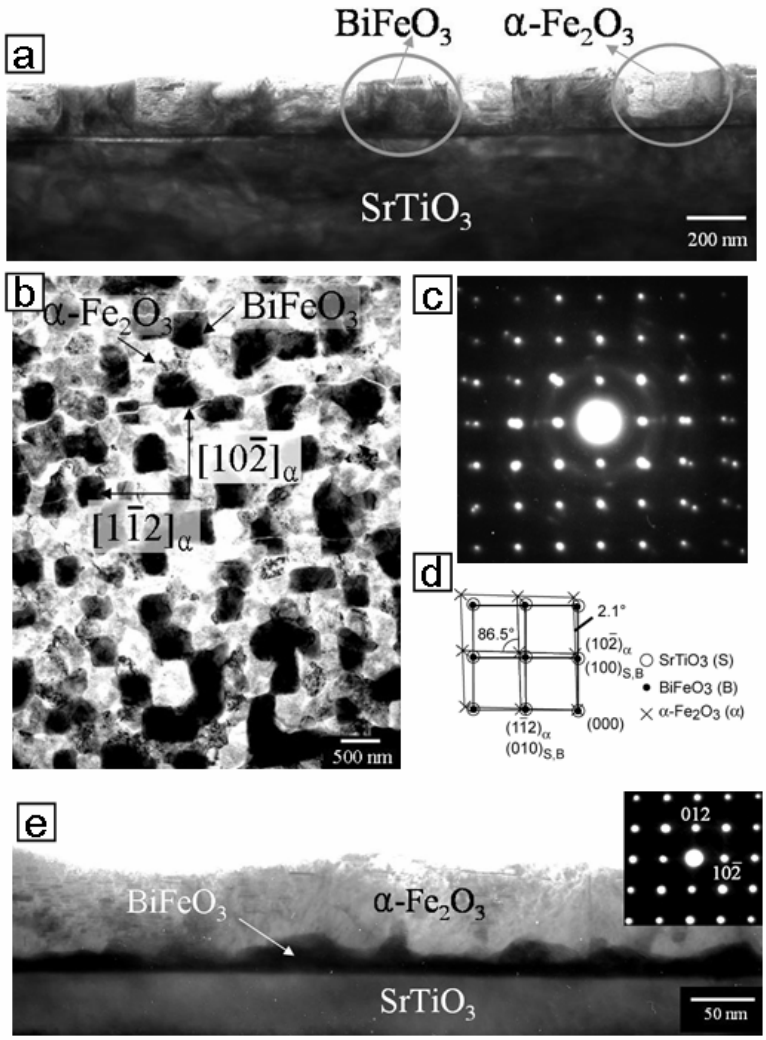

Figure 3.2 (a) Cross-sectional and (b) plan-view TEM images taken from a $BiFeO_3$ film grown at 1 mTorr oxygen pressure, and (c) diffraction pattern and (d) indexing of plan-view diffraction pattern. e) Cross-sectional TEM image and electron diffraction (inset) from a $BiFeO_3$ film grown at 0.1 mTorr oxygen pressure.

Fig. 3.2 (e) shows a $BiFeO_3$ thin film fabricated at 0.1 mTorr. At this low pressure, the dominant phase is α-Fe_2O_3 which forms a continuous layer on a thin layer ($\approx$ 5 nm) of $BiFeO_3$ above the substrate. The fact that α-Fe_2O_3 appears to have

grown above $BiFeO_3$ indicates that it nucleated at the top surface of the film as Bi atoms vaporized following deposition. The SAD pattern in the inset of Fig 3.2 (d) taken from the iron oxide area was indexed to α-Fe_2O_3, and the measured angle (~ 86.5°) between (012) and $(10\bar{2})$ agrees well with the calculated angle (86.0°) in rhombohedral bulk α-Fe_2O_3.

The magnified TEM images from cross-sectional and plan-view specimens in Figs. 3.3 (a) and (b) show γ-Fe_2O_3 in the form of precipitates with a plate-like shape embedded in the α-Fe_2O_3 phase. From indexing the SAD patterns (see Fig. 3.3 (c)), we obtained the following preferred in-plane epitaxial relations among $BiFeO_3$, α-Fe_2O_3, and γ-Fe_2O_3; $[100]_{BiFeO3}$ // $[10\bar{2}]_{\alpha}$ // $[120]_{\gamma}$, and $[010]_{BiFeO3}$ // $[1\bar{1}2]_{\alpha}$ // $[2\bar{1}\bar{1}]_{\gamma}$. The γ-$Fe_2O_3$ also showed other orientations with respect to $BiFeO_3$ and α-Fe_2O_3 in other areas of the sample. This is probably due to the fact that PLD is a non-equilibrium growth technique.

The SAD pattern and the schematic in Fig. 3.3 (c) are from one of the Fe_2O_3 regions where α-Fe_2O_3 and γ-Fe_2O_3 coexist. The out-of-plane and the in-plane parameters in γ-Fe_2O_3 as measured from a high resolution TEM image (see Fig. 3.3 (d)) were $d(120)$ = 0.37 nm and $d(2\bar{1}\bar{1})$ = 0.34 nm, respectively, which are in good agreement with published values (i.e. JCPDS #39-1346). The lattice mismatch between α- and γ-Fe_2O_3 is 8.1 %. Some distortion of the α-Fe_2O_3 lattice and strain concentration around γ-Fe_2O_3 was observed due to the large lattice mismatch.

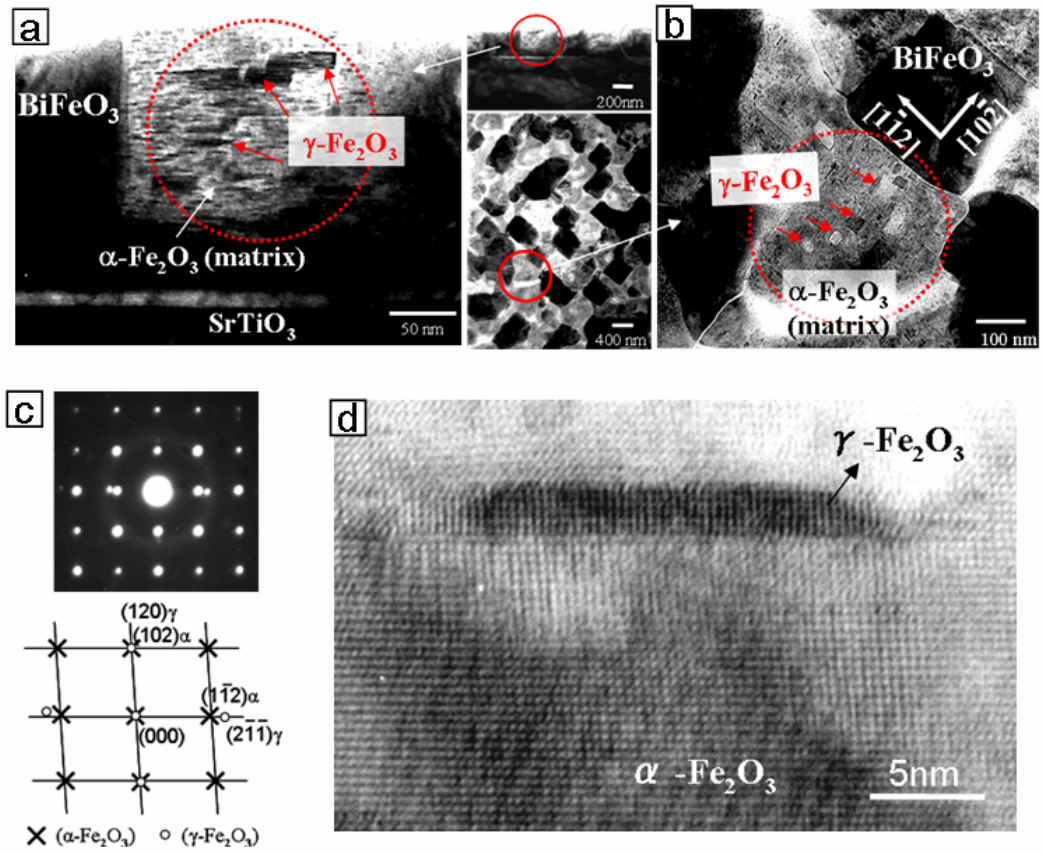

Figure 3.3 TEM bright field images and SAD pattern of bismuth iron oxide thin films fabricated on (001) $SrTiO_3$ substrates at 1 mTorr Po_2. (a) Magnified cross-section (left) and (b) plan-view (right) images showing γ-Fe_2O_3 precipitates and (c) SAD pattern and corresponding schematic of α-Fe_2O_3 and γ-Fe_2O_3 phases in the film deposited at 1 mTorr. (d) High resolution cross sectional TEM image of γ-Fe_2O_3 in α-Fe_2O_3 matrix.

3.3 Change of magnetic properties of Bi-Fe-O by multiphase formation

3.3.1 Formation of γ-Fe_2O_3 and Fe_3O_4

In some $BiFeO_3$ thin films, improved magnetic properties were observed in an earlier study caused by a change of spiral magnetic spin through epitaxial constraint.[48] However, in our study (see section 3.2), we found that the formation of ferri (ferro) magnetic phase, γ-Fe_2O_3 embedded in antiferromagnetic α-Fe_2O_3 grains in films grown at relatively low oxygen pressure or higher temperature is the dominant reason for the observed enhanced magnetization rather than epitaxial constraint by the substrate.[47,52] The saturation magnetization of various $BiFeO_3$ – Fe_2O_3 films were measured by a SQUID magnetometer at room temperature.

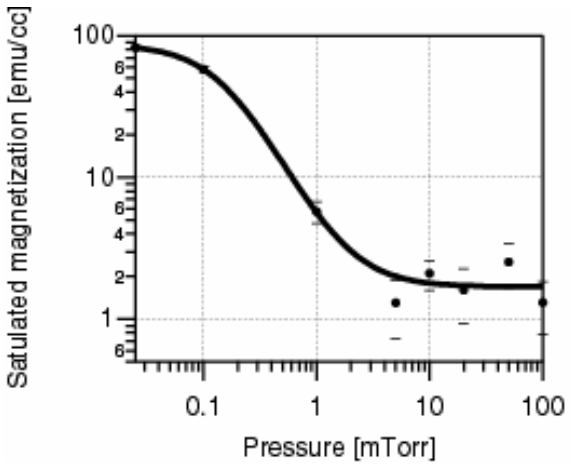

Figure 3.4 Oxygen pressure dependence of saturation magnetization in Bi-Fe-O films. As oxygen pressure decreases, magnetization increases.

As shown in Fig. 3.4, the magnetization observed in the $BiFeO_3$ films grown at oxygen partial pressures higher than 5 mTorr was about 2 emu/cc, which is consistent with the value reported for bulk $BiFeO_3$. However, as the deposition pressure decreases, the magnetization increased up to ~ 80 emu/cc. The enhancement was caused by the formation of γ-Fe_2O_3 at relatively low oxygen partial pressure condition as shown below. α-Fe_2O_3 (hematite) is known to exhibit weak ferromagnetism below the Néel temperature[53] ($T_N \approx 950$ K). In contrast, γ-Fe_2O_3 is known to be a ferro(ferri)magnetic phase with a strong magnetization at room temperature.[54]

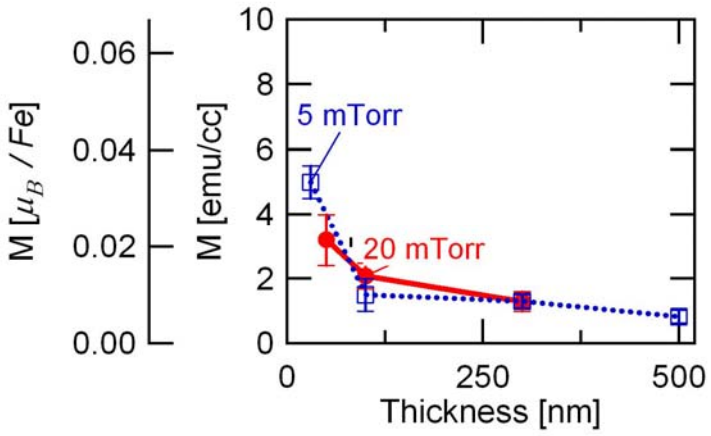

Figure 3.5 Room temperature saturation magnetization (emu/cc) of Bi-Fe-O films as a function of thickness for films grown at 5 mTorr and 20 mTorr.

Figure 3.5 shows the change in magnetization with thickness for films grown at 5 mTorr and 20 mTorr oxygen partial pressures. Pure $BiFeO_3$ films grown at 20 mTorr having thickness of 35 nm showed magnetization of about 5 emu/cc, which is smaller than the results of Wang *et al.*,[20], but is in agreement with other recent

measurements.[65] This slightly enhanced magnetization could result from the heteroepitaxial strain effect in the canted antiferromagnetic film. The magnetic moments of Fe in $BiFeO_3$ are ferromagnetically aligned on the (111) plane and antiferromagnetically switched along the [111] direction. Canting of the Fe magnetic moment allows weak ferromagnetism in $BiFeO_3$. *Ederer* and *Spaldin*[66] found through density functional theory calculations that weak ferromagnetic moments (0.1 μ_B per unit cell for about 1^o canting from the collinear direction) are induced by a structural distortion. Also, as the thickness of the film increases, magnetization in the films with multiple phases is expected to decrease faster than for pure $BiFeO_3$, due to the nucleation of α-Fe_2O_3. However, this reduction of magnetization might be partially compensated by the nucleation of γ-Fe_2O_3. The saturation magnetization decreases with increasing oxygen partial pressure up to 20 mTorr and remains constant above this pressure when the films become pure $BiFeO_3$.

The formation of Fe_2O_3 in $BiFeO_3$ films affected the electrical properties such as leakage current density and electrical polarization as discussed in Section 3.5. Measurements of P-E hysteresis loops were carried out from films grown on $SrRuO_3$ buffered $SrTiO_3$ or 5 % Nb-doped $SrTiO_3$ substrates. After growing $BiFeO_3$ films, optical lithography and deposition of Pt were carried out to deposit a top electrode. Electrical hysteresis loops were measured from the pure $BiFeO_3$ and multiphase Bi-Fe-O films, and the multiphase film showed larger polarization (~ 65 $\mu C/cm^2$) than the pure $BiFeO_3$ film (~ 2 $\mu C/cm^2$) (as shown in section 3.5 below). Also, lower leakage currents were obtained from the multiphase films than from pure $BiFeO_3$. The observed different electrical properties between the pure $BiFeO_3$ thin film and the

multiphase $BiFeO_3$ thin films are somehow related to the different strain relaxation mechanism given in section 3.4 and/or difference in stoichiometry presented in section 3.5.3.

3.3.2 Tuning of magnetic properties of Bi-Fe-O thin film

To enhance the magnetic properties of multiphase Bi-Fe-O film with the columnar structure, we explored the possibility of transforming α-Fe_2O_3 (antiferromagnetic phase) grains to γ-Fe_2O_3 (ferromagnetic phase) grains. Typically, Fe_2O_3 has two different crystal structures. One is a spinel structure (maghemite, γ-Fe_2O_3), and the other is a corundum structure (hematite, α-Fe_2O_3). In bulk, it is known that there is an irreversible transformation from γ-Fe_2O_3 to α-Fe_2O_3 occurring at temperatures above 400 ^oC via restacking of the oxygen layers and displacement of the Fe ions located in the interstices rather than recrystallization. This transformation occurs on the close-packed planes of α- and γ-Fe_2O_3 without diffusion, and thus the crystal orientation relationship between α- and γ-Fe_2O_3 in the bulk was reported as $(0001)_\alpha$ // $(111)_\gamma$, $[01\bar{1}0]_\alpha$ // $[1\bar{1}0]_\gamma$. In our experiments, however, we observed the coexistence of α-Fe_2O_3 and γ-Fe_2O_3 at room temperature, even though γ-Fe_2O_3 is the stable low temperature phase. As described in Fig. 3. 6, we have devised a two-step process to enhance the transformation of α-Fe_2O_3 to γ-Fe_2O_3.[67] The first stage is hydrogen reduction to transform α-Fe_2O_3 into Fe_3O_4, and the second stage is oxidation to transform Fe_3O_4 to γ-Fe_2O_3. The reduction was conducted by flowing a

mixture gas of Ar and H_2 (10_{Ar}:1_{H2}) for 1 hour while the film was kept at 300 ^oC. This was followed by oxidation at 300 ^oC in an oxygen ambient for 1 hour.

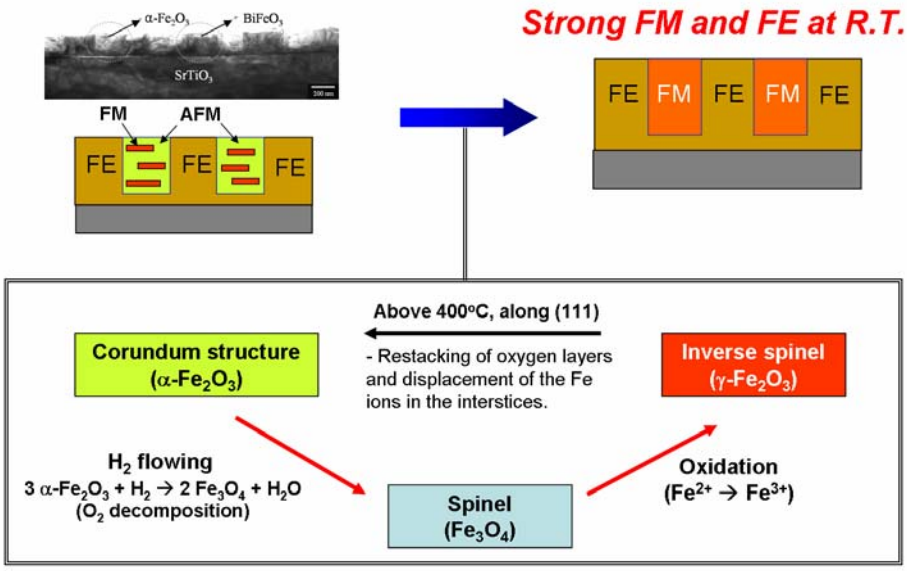

Figure 3.6 Top left image is a cross-sectional image of a Bi-Fe-O film grown at 5 mTorr oxygen pressure with schematic of FE and FM regions before (right) and after (left) annealing. Right schematic is the transformation of α-Fe_2O_3 to γ-Fe_2O_3 upon annealing. Annealing procedures to transform α-Fe_2O_3 into γ-Fe_2O_3 includes hydrogen flowing to transform α-Fe_2O_3 to Fe_3O_4, which is followed by oxidation to transform Fe_3O_4 to γ-Fe_2O_3.

The change of magnetization after the annealing process is shown in the Fig. 3.7. The annealed film showed increased magnetization (~ 6 emu/cc) due to the increase of the fraction of γ-Fe_2O_3 (less than 10 %). The magnetic domain image of the annealed multiphase Bi-Fe-O film was acquired using MFM to confirm the existence of magnetic domains (γ-Fe_2O_3) after annealing. The MFM image in Fig. 3.7 (a) shows the randomly oriented magnetic spins which originate from the γ-Fe_2O_3

phase in the absence of an external magnetic field, and the MFM image in Fig. 3.7 (c) shows the switching of magnetic spins along the out-of plane direction after poling with a field of 20 kOe. From these results, we conclude that the magnetic properties of the film can be controlled by converting α-Fe_2O_3 into γ-Fe_2O_3 through the described procedure. In fact, we found that by adjusting the annealing time and the concentration of hydrogen in the gas mixture, the fraction of γ-Fe_2O_3 and magnetization of the film can be controlled. The magnetization of Bi-Fe-O film can be increased up to ~ 160 emu/cc when all of α-Fe_2O_3 transforms to γ-Fe_2O_3.

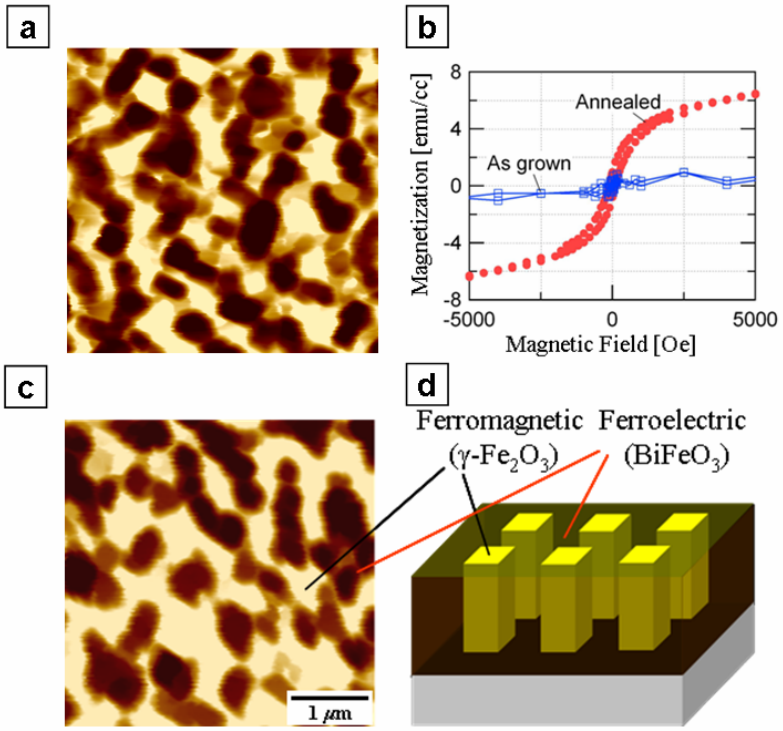

Figure 3.7 Magnetic force microscopy (MFM) images of an annealed multiphase film (a) before and (c) after magnetizing the film perpendicular to the surface by applying 20 kOe magnetic field. (b) Hysteresis loops of as grown and annealed multiphase Bi-Fe-O films. (d) Schematic of the microstructure of Bi-Fe-O multiferroic nanocomposites.

3.4 Change of misfit strain in $BiFeO_3$ thin films by multiphase formation

3.4.1 Thickness dependent misfit strain

To investigate the microstructural evolution in the Bi-Fe-O system and its effect on the structural and magnetic properties of the films, Bi-Fe-O thin films of different thicknesses (15 – 500 nm) were epitaxially grown on $SrTiO_3$ (001) substrates by pulsed laser deposition under various oxygen partial pressures.

Figures 3.8 (a) and (b) show, respectively, x-ray diffraction spectra obtained from films of different thicknesses grown at an oxygen partial pressure of 5 mTorr and corresponding TEM cross-sectional images. The 35 nm thick film grown at 5 mTorr oxygen partial pressure shows the pure epitaxial $BiFeO_3$ phase with the [001] orientation and a slightly larger lattice parameter (c = 0.407 nm) than that of the pure 300 nm thick $BiFeO_3$ film grown at 20 mTorr. As the film thickness increases, the intensity of the (002) diffraction peaks of the $BiFeO_3$ increases, and the peak shifts to a higher 2θ angle. This indicates that the out-of-plane lattice parameters of $BiFeO_3$ decreases with increasing thickness. We also observed peaks corresponding to the (024) plane of the α-Fe_2O_3 phase and the (240) plane of the γ-Fe_2O_3 phase. The α-Fe_2O_3 phase has a rhombohedral crystal structure (space group: $R\bar{3}c$) with lattice constants of $a = b$ = 0.505 nm, c = 1.319 nm, and the γ-Fe_2O_3 phase has the cubic (or inverse spinel) crystal structure that belongs to the space group P4132 (or $Fd\bar{3}m$) with

lattice parameter a = 0.83515 nm. The intensity of the peaks corresponding to α- and γ-Fe_2O_3 increases with increasing film thickness.

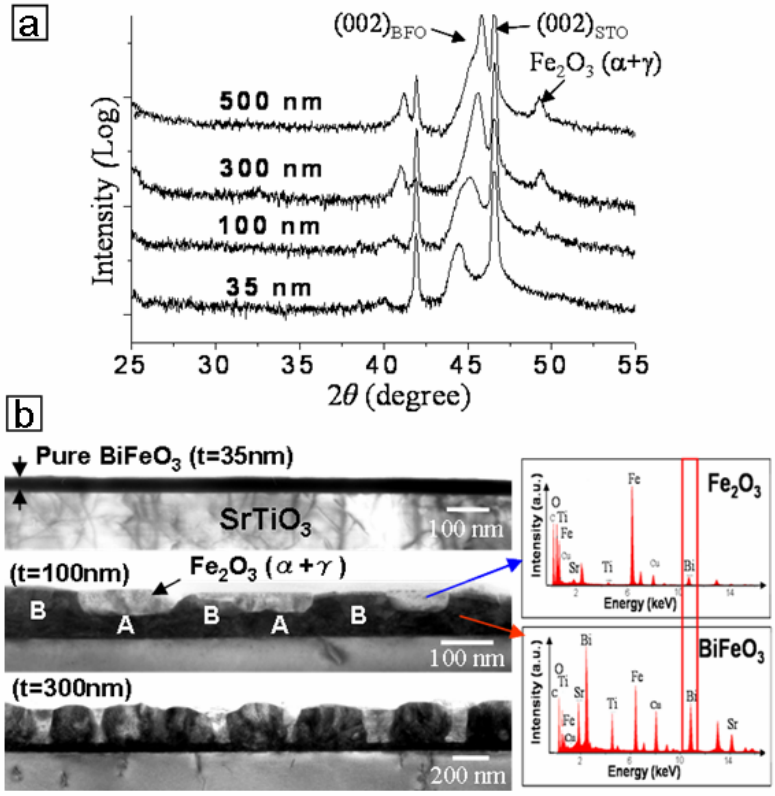

Figure 3.8 (a) X-ray diffraction spectra (in log scale) and (b) TEM cross-sectional images (left) and EDS spectra (right) of Bi-Fe-O films grown at 5 mTorr with different thickness. Nucleation of impurity phases starts at ~ 50 nm. The intensity of the peak labeled Fe_2O_3 in (a) corresponding to the impurity phases increases with increasing film thickness.

From the TEM cross-sectional images shown in Fig. 3.8 (b), we can see that the secondary phase, α-Fe_2O_3, forms in the surface region of films of thickness of 50 nm, and then it grows to have a columnar structure with continued deposition. The EDS spectra in Fig. 3.8 (b) obtained from the bright and dark columns of the film

confirmed the chemical composition of the separated phases. The EDS spectrum from the bright columns shows little bismuth content (5.5 at%), and the atomic ratio between iron (38.5 at%) and oxygen (56 at%) is 1:1.45, which is consistent with Fe_2O_3. The EDS spectrum from the dark columns, shows a 1: 1.1 ratio between bismuth (24 at%) and iron (26.3 at%), which is consistent with $BiFeO_3$.

To further understand the misfit strain relaxation mechanism, multiphase Bi-Fe-O films with different thickness (35 – 500 nm) were compared to a single phase $BiFeO_3$ film with a gradual change in thickness. The change of out-of plane lattice parameter with different thicknesses was obtained from the pure $BiFeO_3$ film and multiphase Bi-Fe-O film (see Fig. 3. 9).

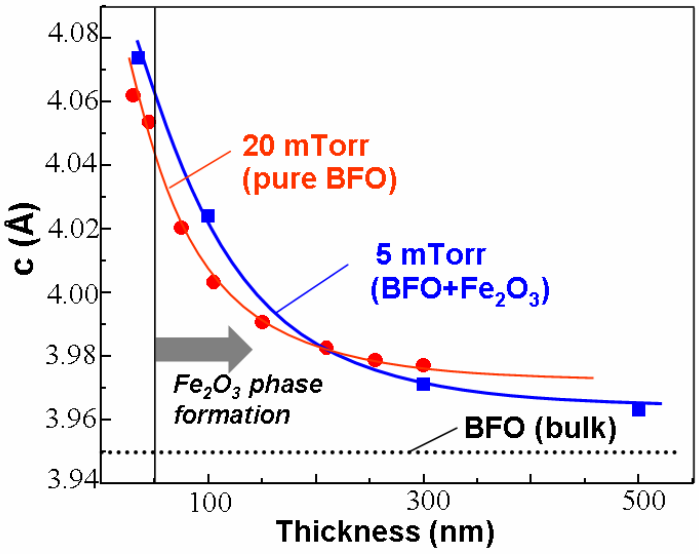

Figure 3.9 Out-of-plane lattice parameters in pure $BiFeO_3$ and $BiFeO_3$ with secondary phases as a function of film thickness.

The region of the film with 35 nm thickness showed a highly strained area. As the film thickness increases from 30 to 300 nm, the out-of-plane lattice parameter of pure $BiFeO_3$ film gradually decreases from 0.406 to 0.398 nm. However, in the multiphase films, the out-of-plane lattice parameter decreases from 0.407 to 0.396 nm with increasing film thickness from 35 to 500 nm. This result confirms that the α-Fe_2O_3 domains that form on the surface region of the film for films of thickness above 50 nm (grown at low oxygen partial pressure) enhance the relaxation of misfit strain in $BiFeO_3$ columns. As a result, the total misfit strain reduction is from 0.51 % (pure $BiFeO_3$) to 0.25 % (mixture of $BiFeO_3$ and Fe_2O_3) for films with thickness of 300 nm.

3.4.2 Gradient thickness samples

The existence of secondary phases can affect the relaxation of misfit strain in $BiFeO_3$ and result in significant changes of the ferroelectric and ferromagnetic properties of $BiFeO_3$ films. To compare the out-of-plane lattice parameter of multiphase Bi-Fe-O and pure $BiFeO_3$ with different thicknesses, $BiFeO_3$ films with gradual change in thickness were fabricated by the gradient deposition technique using a shadow mask. Oxygen partial pressure of: 20 mTorr was selected to fabricate pure $BiFeO_3$ films, and 5 mTorr to make multiphase Bi-Fe-O films. The thickness of these films varied in the range of 30 – 300 nm.

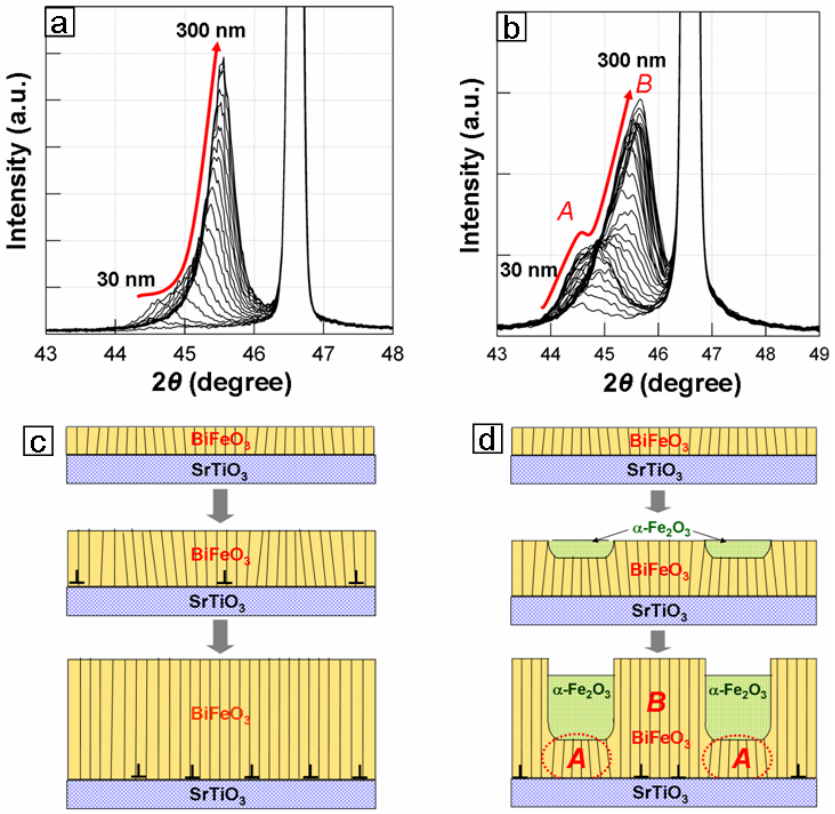

Figure 3.10 Superpositions of x-ray microdiffraction scans from regions of films with a thickness gradient grown at (a) 20 mTorr and (b) 5 mTorr. The thickness varied from 30 to 300 nm. Schematics of the misfit strain relaxation mechanism in (c) pure $BiFeO_3$ film and (d) multiphase Bi-Fe-O film are suggested. Multiphase film shows coexistence of highly strained region (A) and fully relaxed region (B).

Figures 3.10 (a) and (b) show superposition of x-ray microdiffraction scans from different regions of the pure $BiFeO_3$ film (a) and multiphase Bi-Fe-O film (b) with different thicknesses. In Fig. 3.10 (a), the position of the (002) peak of $BiFeO_3$ shifts from $2\theta = 44.6^o$ to 45.6^o as the film thickness increases. In contrast, the spectra in Fig. 3.10 (b) show a broad peak at $\sim 2\theta = 44.5^o$ in the thin regions of the sample which evolves into two peaks as the film thickness increases; the thicker regions

show a peak at ~ 45.7° which corresponds to $BiFeO_3$. However, a second peak at ~ 44.5° remains with weaker intensity even for thickness up to 300 nm. The observation of two peaks in Fig. 3.10 (b) is consistent with the coexistence of a strained region and a relaxed region in the film. More evidence of the two regions was obtained from TEM images as shown below. These results indicate that the multiphase film has a different relaxation mechanism than the pure $BiFeO_3$ films. Typically, the misfit strain between a film and a substrate is relaxed by the generation of misfit dislocations at the interface with increasing film thickness.[68,69] As shown in Fig 3.10 (c), pure $BiFeO_3$ showed typical relaxation mechanisms in which the strain gradually relaxes as the film thickness increases. The multiphase Bi-Fe-O film with small thickness showed a highly strained film as expected. However, the thicker region of the film showed both a relaxed region [represented by the x-ray peaks labeled "B" in Fig. 3.10 (b)] and a highly strained region [labeled "A" in Fig. 3.10 (b)] in the film even though the thickness of the film was above the critical thickness for relaxation to take place [see also Fig. 3.10 (d)]. This observation can be explained by the formation of the α-Fe_2O_3 regions, which appeared in the surface region of the film with thickness around 50 nm. The transformation to α-Fe_2O_3 in the surface region of the film reduces the thickness of the $BiFeO_3$ underneath. Therefore, the area below α-Fe_2O_3 [marked A in Fig. 3.8 (b)] showed higher misfit strain and a lower misfit dislocation density than the region with pure $BiFeO_3$ [marked B in Fig. 3.8 (b)] as determined by high resolution TEM images (not shown). In addition, the formation of α-Fe_2O_3 regions enhances the relaxation of misfit strain in the $BiFeO_3$ columns between α-Fe_2O_3 columns due to the reduction of unit volume as explained below.

The reduction of volume partially releases the compressive strain along the in-plane direction.

The observation of a broad peak in the XRD spectra in Fig. 3.10 (b) for thicknesses above ≈ 50 nm indicates that the bottom portion of the films under the Fe_2O_3 region (region A) in Fig. 3.10 (d) remains strained. In order to understand the higher degree of stain relaxation in the films with Fe_2O_3, we estimate the change in volume in these regions.

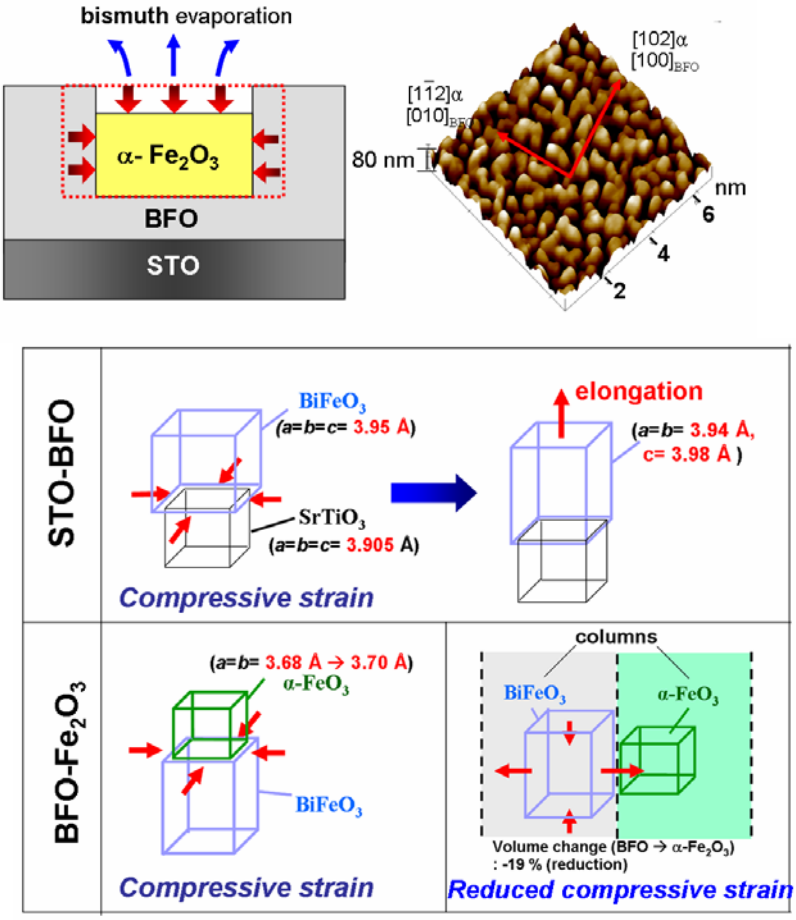

Figure 3.11 Schematics of two different strain relaxation mechanisms. In multiphase $BiFeO_3$, in-plane compressive stress of $BiFeO_3$ columns is relaxed by the formation of Fe_2O_3 phase with smaller volume. AFM image from the surface (upper right) also confirmed smaller volume of Fe_2O_3 phase from height difference between columns

A reduction in volume of ≈ -19 % by the formation of the Fe_2O_3 phase allows expansion of $BiFeO_3$ (which is under compressive strain with the substrate) which in turn reduces the misfit strain. Therefore, the formation of α-Fe_2O_3 by evaporation of the more volatile Bi metal at relatively low oxygen partial pressure enhances the relaxation of the compressive stress in $BiFeO_3$. The relaxation is accelerated as the α-Fe_2O_3 volume fraction increases (see Fig. 3.11).

3.5 Change of ferroelectric properties by multiphase formation

After the initial discovery of the increase in electrical polarization (~ 55 $\mu C/cm^2$) in $BiFeO_3$ thin films, the misfit strain and structural distortion of the $BiFeO_3$ lattice were suggested as the reasons for the large polarization.[20] The crystal structure in the films changed from the bulk rhombohedral to monoclinic due to the epitaxial strain induced by the substrate. There have also been a number of reports on thin films of $BiFeO_3$ with large electrical polarization, but the origin of the large polarization in these cases has not been unambiguously established. We also have fabricated numerous $BiFeO_3$ films with different conditions, and found that the $BiFeO_3$ films which are grown at relatively lower oxygen partial pressure and include Fe_2O_3 phase show large polarization. These films also show clear contrast change in switching of ferroelectric domains in PFM images as shown below. To further understand the role of multiphase formation on the electrical properties of $BiFeO_3$ films, we performed a systematic study of the electrical properties of $BiFeO_3$ films to understand the origin of the observed large polarization in an attempt to control and

improve the properties as shown below.

3.5.1 Ferroelectric properties in columnar $BiFeO_3 – Fe_2O_3$

To study the origin of the larger polarization in $BiFeO_3$, we compared two different types of $BiFeO_3$ films which were grown at 2 mTorr and 20 mTorr, because the films grown 20 mTorr are yellow in color and show weak polarization (less than 2 $\mu C/cm^2$), while the films grown at 2 mTorr are red in color and exhibit large polarization (~ 72 $\mu C/cm^2$) [see Fig. 3.12].

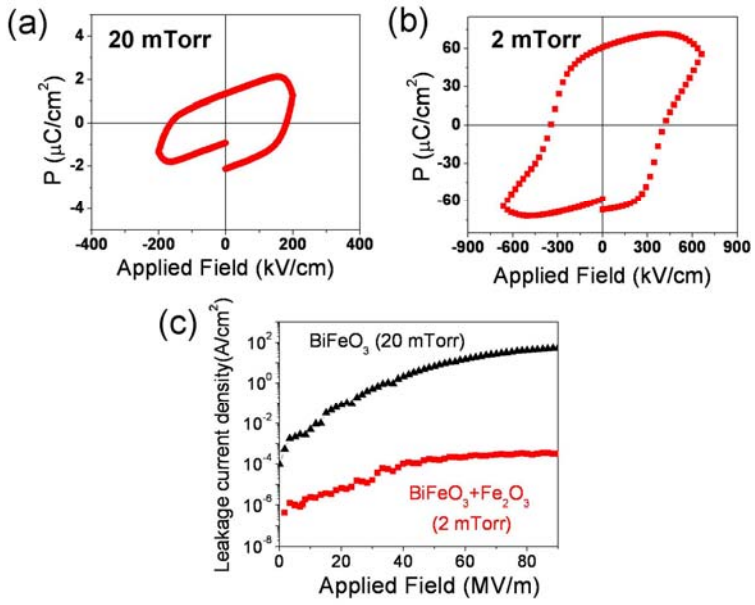

Figure 3.12 Electrical polarization vs. applied electric field from the samples grown at (a) 20 mTorr and (b) 2 mTorr. (c) Leakage current density measured from the two samples.

Typically, the films grown at low oxygen pressure have more oxygen vacancies and bismuth deficiencies in the films and result in poor insulating properties, but as shown in Fig. 3.12 (c), the columnar $BiFeO_3$ showed robust

insulating property even though the film was synthesized at low oxygen partial pressure.

To characterize the structure of the films, TEM and AFM were used. From our plan-view TEM images shown in Figs. 3.13 (a) and (b), the film grown at 20 mTorr oxygen pressure [Fig. 3.13 (a)] is pure $BiFeO_3$, but the film grown at 2 mTorr oxygen pressure [Fig. 3.13 (b)] has columnar structure of Bi deficient phase, Fe_2O_3 (bright region) and $BiFeO_3$ (dark region) as was presented in sections 3.1, 3.2, and 3.3.

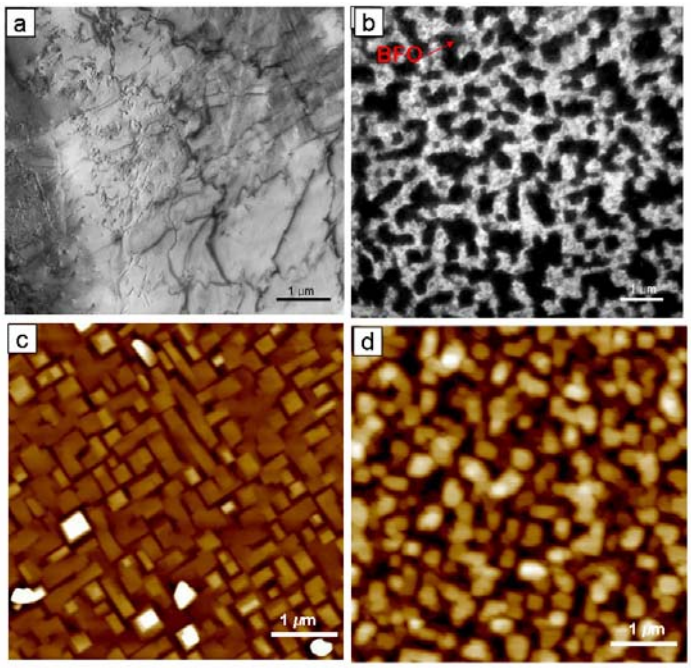

Figure 3.13 Bright field TEM images from $BiFeO_3$ films grown at (a) 20 mTorr and (b) 2 mTorr. Surface morphology of the films grown at (c) 20 mTorr and (d) 2 mTorr measured by AFM.

AFM images from both samples showed similar square shaped grains. However, the squares in Fig. 3.13 (d) represent the columnar structure of multiphase $BiFeO_3$, while the squares in Fig. 3.13 (c) correspond to roughness or texture of pure $BiFeO_3$ grains.

3.5.2 Ferroelectric domain switching analysis using piezo force microscopy (PFM)

Figures 3.14 and 3.15 show switching domain images and piezoelectric response from the $BiFeO_3$ films grown at 20 mTorr and 2 mTorr, respectively, using PFM. The multiphase $BiFeO_3$ film grown at 2 mTorr [Fig. 3.15 (b)] shows more clear contrast of switching in polarization than the pure $BiFeO_3$ film grown at 20 mTorr [Fig. 3.14 (b)].

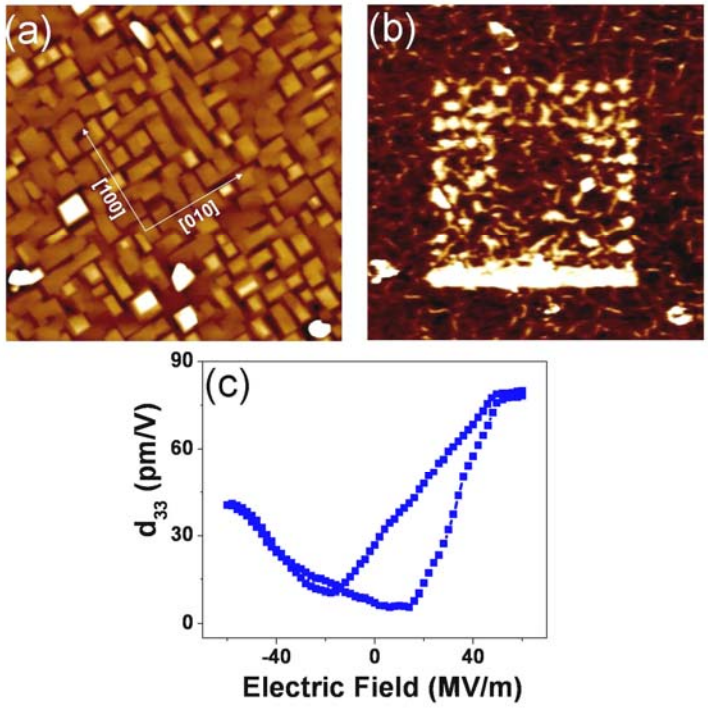

Figurer 3.14. (a) 5 × 5 μm^2 height image and (b) ferroelectric domain switching images from the $BiFeO_3$ thin film grown at 20 mTorr oxygen pressure. To obtain image showing switching of ferroelectric domains a + 10 V and – 10 V bias were alternately applied on 3 × 3 μm^2 and 1 × 1 μm^2 area, respectively. (c) The piezoelectric coefficient (d_{33}) was measured from strain loop.

As shown in the AFM image in Fig. 3.14 (a), the $BiFeO_3$ film grown at 20 mTorr showed texture along [100] and [010] orientation of $SrTiO_3$. From the

switching ferroelectric domain image in Fig. 3.14 (b), when the electric field in reversed from + 10 V to – 10 V and – 10 V to + 10V, the pure $BiFeO_3$ film showed non-uniform contrast and poor switching probably due to the large leakage current in the sample [see Fig. 3.12 (c)]. Also the d_{33} loop measurement showed asymmetric shape indicative of a poor ferroelectric.

However, the columnar $BiFeO_3$ films which have secondary phase (Fe_2O_3) exhibit clear change of contrast with reversing dc bias [see Fig. 3.15 (b)]. Also interestingly, the switching of ferroelectric domains show more clearly in the interface regions between $BiFeO_3$ and Fe_2O_3 columns than in the $BiFeO_3$ regions [see Fig. 3.15 (d)]. Furthermore, the strain loops obtained from the edge region showed a more symmetric shape than that from the middle of the $BiFeO_3$ domains. These facts indicate that the $BiFeO_3$ in the middle and edge of column might have different state of misfit strain, and/or chemical composition.

As shown in section 3.4.1, multiphase formation aids in the strain relaxation mechanism in Bi-Fe-O films. Furthermore, the formation of Fe_2O_3 induced non-uniform strain relaxation of the surrounding $BiFeO_3$ phase. The strain in the $BiFeO_3$ columns between the Fe_2O_3 columns was reduced due to the reduction in volume upon the formation of Fe_2O_3. Therefore, strain relaxation can be one reason for the large polarization. Furthermore, the observed large polarization might be an intrinsic property of $BiFeO_3$. Recently, there has been an attempt to reduce the strain in $SrRuO_3$ films and obtain a single-domain variant of the $SrRuO_3$ by using $DyScO_3$ substrates which have almost the same lattice constant as $SrRuO_3$,[55] These films showed increase in polarization. Their results also suggest that strain relaxation could

play a role in influencing the polarization. In addition, large polarization has been reported from bulk single crystal $BiFeO_3$ in recent papers.[56]

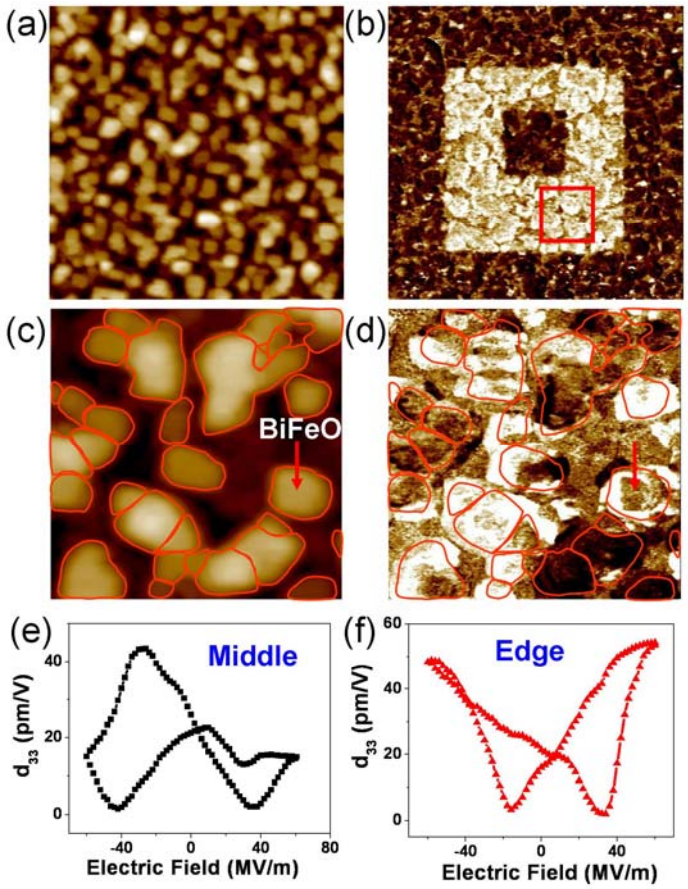

Figure 3.15. (a) 5 × 5 μm^2 AFM height image and (b) switching ferroelectric domain image from the $BiFeO_3$ film grown at 2 mTorr. Magnified (c) AFM height image and (d) corresponding PFM image of switching domains from the region marked in (b) d_{33} versus applied voltage obtained from (e) middle and (f) edge of a $BiFeO_3$ column.

However, there still exists another possible reason for the large polarization in films containing secondary phases, which is the local change of stoichiometry in the film. Volatile Bi can easily evaporate from the surface of $BiFeO_3$ during growth, and result in the formation of Bi deficient Fe_2O_3 phase. In this procedure, the $BiFeO_3$ region surrounding the Fe_2O_3 regions could also be off-stoichiometric and change the

volume of the unit cell and the Fe ion valence from 2+ to 3+. This possibility is investigated by electron energy loss spectroscopy as discussed in the next section.

3.5.3 Chemical analysis on columnar $BiFeO_3$ – Fe_2O_3 thin films using EDS and EELS in TEM

We used EDS and EELS, for the chemical analysis on the columnar structure of a $BiFeO_3$ thin film grown at 2 mTorr. The dark field scanning TEM (STEM) image in Fig. 3.16 (a) and EDS mapping image for Bi-L peak in Fig. 3.16 (b) identified the bright columns in an STEM image to be $BiFeO_3$. Therefore, an EELS line scanning was performed on a bright column in an STEM image for chemical information of $BiFeO_3$ across the interface between $BiFeO_3$ and Fe_2O_3. The Fe valence state (3+ and 2+) was investigated from EELS spectra acquired at × 3 M magnification measured point by point across the interface between $BiFeO_3$ and Fe_2O_3 columns. The ratio of Fe^{3+} and total Fe was calculated from the ratio between Fe L_3 and Fe L_2 peaks (Fe^{3+}/ $\sum$Fe) in the EELS spectra and are given in Fig. 3.16 (d). The values show the position at which each spectrum was collected. Higher values indicate a higher amount of Fe^{3+} state. The Fe^{3+}/ $\sum$Fe ratio decreases near the interface indicating an increase of Fe^{2+} and O^{2-} vacancies in the boundary area between $BiFeO_3$ and Fe_2O_3. The variation in Fe^{2+}, Fe^{3+} and O^{2-} could be responsible for the increase in polarization in $BiFeO_3$ thin films. A more detailed study of EELS should be followed to understand the role of Fe^{2+} and O^{-} vacancies in the ferroelectric properties of $BiFeO_3$ as discussed in the future work section of this thesis.

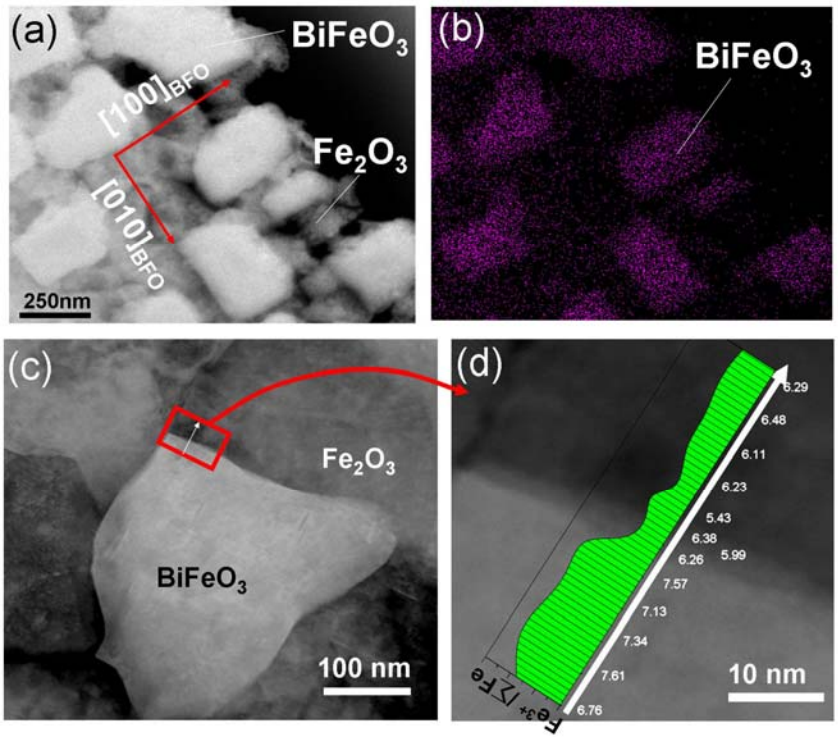

Figure 3.16. (a) Scanning TEM dark field image and (b) EDS elemental mapping of Bi-L edge. (c) Magnified dark field STEM image and (d) EELS line scan for $Fe^{2+}/\Sigma Fe^{3+}$.[118]

3.6 Multiferroic properties in polycrystalline $BiFeO_3$ thin films

In order to obtain the ferroelectric properties of unstrained $BiFeO_3$ films, the ferroelectric properties of polycrystalline multiferroic bismuth ferrite thin films were investigated. These films have no strain effects or impurities which can be easily introduced in epitaxial single crystal thin film growth due to the relatively high growth temperature and the epitaxial constraint from the substrate. We observed relatively large polarization (P_S = 106 μC/cm^2) in polycrystalline thin films grown at 400 ^oC which suggests an intrinsically excellent ferroelectric property of $BiFeO_3$. In

particular, effective switching of ferroelectric domains during poling of polycrystalline $BiFeO_3$ was observed only in films with nano-grains probably containing single domains. The low density of domain boundaries facilitates domain switching. Also, post growth annealing of films grown at 300 ^oC produced nucleation of nano-sized grains from non-crystallized bismuth ferrite with increase in saturation polarization (P_S) from ~ 8 (as grown) to 82 (after annealing) $\mu C/cm^2$.

The recent discovery of increase in polarization and magnetization in $BiFeO_3$ thin films [20] and bulk [117] have given $BiFeO_3$ a new outlook, especially since bulk $BiFeO_3$ had been known to exhibit weak ferroelectricity (P_S ~ 3.5 $\mu C/cm^2$ below T_C = ~ 1100 K) and canted antiferromagnetism (~ 2 emu/cc below T_N = ~ 640 K) at room temperature.[21-24] In recent reports, the misfit strain in the film induced from the lattice mismatch with the substrate as well as structural distortions from the transformation of rhombohedral to tetragonal crystal structure in $BiFeO_3$ thin films were believed to be responsible for the increase in both electrical polarization and magnetization. However, we observed that the increased magnetization is due to the presence of ferromagnetic phases (Fe_3O_4 and γ-Fe_2O_3) in the films resulting from the high volatility of bismuth.[76-78] The actual cause for the increase in polarization in $BiFeO_3$ films is still not fully understood, although very recent reports of bulk $BiFeO_3$ suggested that the high dielectric constant and polarization are intrinsic to $BiFeO_3$.[79]

There have also been reports of weak ferroelectricity of $BiFeO_3$ [23,80,81] based on unsaturated P-E hysteresis curves (P_S ~ 3.5 $\mu C/cm^2$) measured from single crystalline $BiFeO_3$. These investigations have attempted to solve the problem of

applying insufficient electric field to bulk $BiFeO_3$ and the issue of large leakage current found in earlier studies of bulk $BiFeO_3$. Recent studies reported larger polarizations in single crystalline films with reduced misfit strain and in single crystalline bulk $BiFeO_3$.[82,83]

In spite of much recent studies of the ferroelectric properties of $BiFeO_3$, its intrinsic properties are not well understood because of the complex dependence of its properties on the presence of impurities, strain and/or defects. In the current study, we systematically investigated the structural evolution of polycrystalline $BiFeO_3$ films and their intrinsic properties. The films used for our study were non-epitaxial to reduce the effects of strain with the substrate and grown at low temperatures to avoid the formation of impurity phase. More importantly, the work in this section explores the effects of grain size on ferroelectric domain switching which is crucial for practical applications. Moreover, polycrystalline $BiFeO_3$ thin films grown at low temperature have the advantage over single crystalline epitaxial films because they are not clamped by the substrate and are less likely to contain defects such as, oxygen vacancies produced to compensate for the evaporation of volatile bismuth atoms when the films are grown at high growth temperatures. In this current work, we observed switching of ferroelectric domains as well as large polarization in nano-grain polycrystalline $BiFeO_3$ films. The nano-grain structure was specially chosen in an attempt to achieve a statistically uniform domain size distribution and ultra high density which are requirements in the ferroelectric memory storage devices, such as the ferroelectric random access memory (FeRAM) or the probe base data storage (PBDS) applications.[84-86]

3.6.1 Size effects on electrical polarization and electrical properties

For the systematic study of the relationship between the domain size and ferroelectric properties of polycrystalline $BiFeO_3$, we deposited a series of films using PLD at low temperatures in the range 300 – 500 ^oC. The microstructure of the films was characterized by X-ray diffraction and transmission electron microscopy (TEM). Figure 3.17 shows bright field TEM images and diffraction patterns acquired from samples grown at different temperatures. As shown in Fig. 3.17 (a), the film grown at 300 ^oC has a semicrystalline or amorphous-like structure due to the low growth temperature. The high resolution TEM analysis from the sample (not shown) showed no contrast from grain boundaries or lattice fringes indicating that the film is amorphous-like. However, the films grown at 400 ^oC showed nano-sized (~ 40 nm) grains which nucleated and crystallized from the amorphous matrix. The diffraction patterns from the sample grown at 300 ^oC show continuous rings which partially change to spots due to grain growth at 400 ^oC. Based on X-ray diffraction spectra (not shown) and indexing of the electron diffraction patterns obtained from the films grown at 300 ^oC and 400 ^oC [shown in Fig. 3.17 (d)], the films show polycrystalline randomly oriented rhombohedral $BiFeO_3$ structure with no evidence of secondary phases. As the growth temperature increases further to 500 ^oC, the grain size increased to about 100 – 150 nm diameter [Fig. 3.17 (c)].

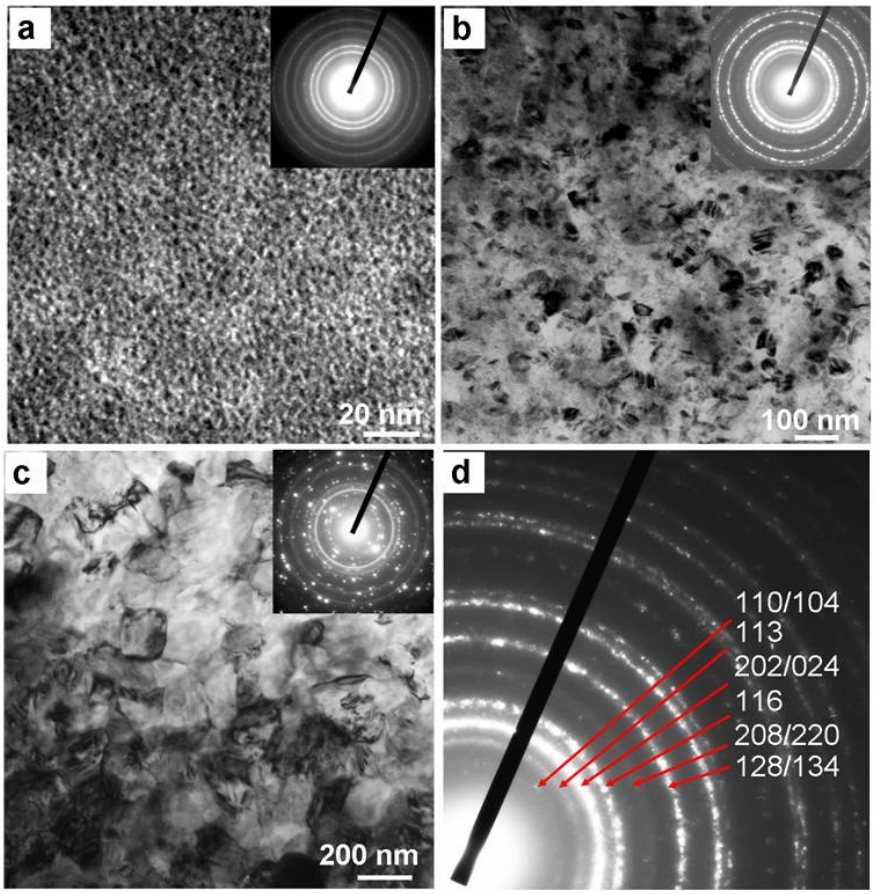

Figure 3.17. Bright field TEM images and corresponding electron diffraction patterns from the polycrystalline $BiFeO_3$ films grown at (a) 300 ^oC, (b) 400 ^oC, and (c) 500 ^oC. As the deposition temperature increases, the grain size increases from 40 to 150 nm. (d) The diffraction pattern from the film grown at 400 ^oC indicates randomly oriented polycrystalline $BiFeO_3$ with no impurities.

The diffraction pattern shown in Fig. 3.17 (c) indicates more nucleation and grain growth based on a dimmer continuous ring pattern with superimposed strong spots. However, even at 500 ^oC no evidence for secondary phases was observed.

The electrical polarizations corresponding to the films with different grain sizes were measured. As shown in the polarization-electric field (P-E) hysteresis

curves in Fig. 3.18, the semicrystalline film grown at 300 ^{o}C [Fig. 3.18 (a)] exhibits low saturation polarization (P_S ~ 8 μC/cm^2) with unsaturated hysteresis loops.

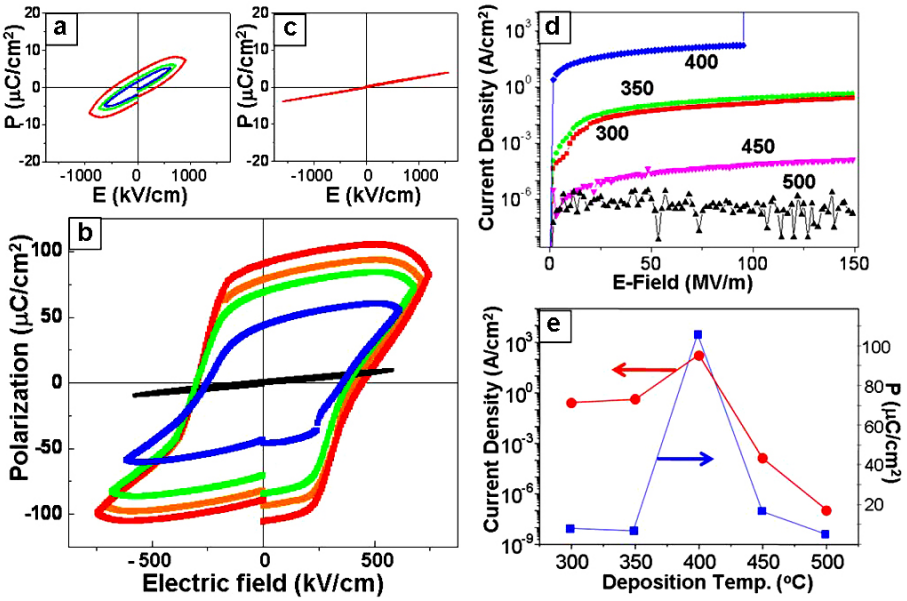

Figure 3.18. Electrical polarization hysteresis loops from the samples grown at (a) 300 ^{o}C (b) 400 ^{o}C, and (c) 500 ^{o}C. Each loop was acquired at different applied voltage (38, 44 and 55 V for (a) and 37, 41, 43 and 45 V in (b). (d) Leakage current density of each sample as function of applied electric field, and (e) relationship between saturation polarization and leakage current on deposition temperature. The film grown at 400 ^{o}C showed the largest polarization (Ps ~ 106 μC/cm^2) with 800 kV/cm of coercive field as well as highest leakage current density.

However, the film grown at 400 ^{o}C which has more crystallized area than the film grown at 300 ^{o}C consisting of nano-grains shows a dramatic increase in saturation polarization (P_s ~ 106 μC/cm^2) and a decrease of coercive field (~ 800 kV/cm) at an applied electric field of 750 kV/cm as shown in Fig. 3.18 (b). This value was the largest polarization observed in the series of polycrystalline $BiFeO_3$ films implying that the low polarization in bulk $BiFeO_3$ in early reports does not represent

the intrinsic saturation polarization of $BiFeO_3$. Our results also indicate that the observed increase in epitaxial single-crystalline thin film is not caused by the misfit strain and structural distortions from the substrate. Compared to bulk, smaller remanent polarization, reduced by ~ $(2^{-1/2})P_r$ is typically predicted in thin films.[87] However, the P_r obtained from our polycrystalline $BiFeO_3$ deposited at 400 ^oC was much higher (91 $\mu C/cm^2$) than the reported value for bulk (~ 3.5 $\mu C/cm^2$) as well as for thin epitaxial films and it is comparable to the recent reports from bulk $BiFeO_3$.[117]

As the growth temperature increases further to 500 ^oC, the films show a decrease in polarization without saturation [Fig. 3.18 (c)]. Even at the electric field of 165 MV/m, the hysteresis loop was not saturated. Typically, as the grain size decreases in submicron scale ($d < 1$ μm), the saturation polarization as well as the remanent polarization decrease because domain wall mobility decreases by a reduced number of domain variants in the fine grains. The leakage current density and saturation polarization as a function of growth temperature plotted in Figs 3.18 (d) and (e) show that as the growth temperature increases, the leakage current density also increases. This increase is probably due to the increase in grain boundaries in the films at higher growth temperature.[88] It is interesting to notice that the film grown at 400 ^oC showed the highest leakage current (0.91×10^2 A/cm^3 at an applied electric field of 50 MV/cm^3) as well as the largest polarization. As the growth temperature increased further, there was a rapid decrease of leakage current density due to grain growth and reduction of the grain boundary area. The large polarization in the film grown at 400 ^oC suggests that nano-grain formation might facilitate the ferroelectric

domain mobility by decreasing the domain wall density within the nano-grains. It is well known that the domain wall mobility is closely related to the relative crystallographic orientation between neighboring domains. In micron-size grains (d > 150 nm), each grain contains multi-domains and the average domain wall density (N_d) is known to be proportional to $N_d \sim d^{1/2}$. However, as the diameter of the grains approaches the nano-scale, each grain prefers to have single domain and the domain wall density equation follows $N_d \sim d^{-1/2}$. Therefore, a smaller domain wall density in a nano-crystalline structure might reduce pinning from domains oriented along different directions and result in the switching of ferroelectric domains.

3.6.2 Switching of ferroelectric nano-domains

Further investigation of the polarization reversal in the nano-sized grains was performed using piezo force microscopy (PFM). The $BiFeO_3$ with rhombohedral crystal structure is known to have a spontaneous polarization along the [111] direction below *T*c, with either 70 ^{o} or 109 ^{o} ferroelectric domain switching during poling.[90,91] Figure 3.19 shows the height images and corresponding images of switching of polarization domains acquired from the samples grown at different temperatures. From the height images in Figs. 3.19 (a), (b) and (c), the films showed increase of grain sizes and roughness as the growth temperature increased from 300 to 500 ^{o}C. As shown in Fig. 3.19 (a), the film grown at 300 ^{o}C has very smooth surface (root mean square roughness ~ 0.15 nm) without clear grain boundaries. The PFM images in Figs. 3.19 (d), (e) and (f) were obtained after applying a voltage of +

15 V to an area of 3 × 3 μm^2 and then – 15 V to an area of 1.6 × 1.6 μm^2 within the original applied voltage. Fig. 3 19(d) shows no contrast which would indicate change in polarization under the applied electric field. However, the film grown at 400 ^{o}C which showed the largest polarization with nano-grains also exhibited clear domain switching after writing [see Fig. 3.19 (e)]. As the applied bias field reverses from + 15 V in 3 × 3 μm^2 area to – 15 V in 1.6 × 1.6 μm^2 area to + 15 V in 0.8 × 0.8 μm^2 area, the contrast changed due to the change in orientation of the polarized ferroelectric domains [see Fig. 3.19 (e)]. Figure 3.19 (c) shows larger grains in the film grown at 500 ^{o}C. A higher contrast of the ferroelectric domains [Fig. 3. 19(f)] is observed due to the enhanced crystallinity of the film. However, the direction of polarization of the domains did not reverse after switching the dc bias from + 15 V to – 15 V alternately.

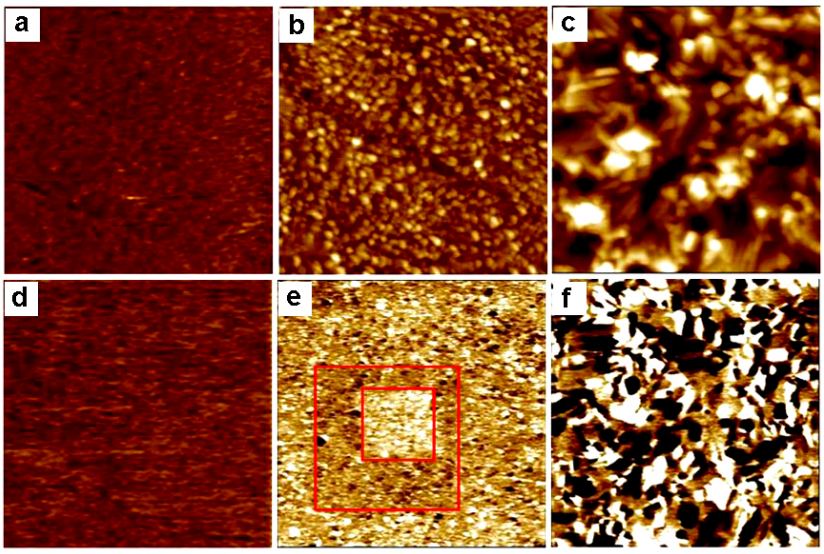

Figure 3.19. AFM height images (top) and PFM images (bottom) of switching electrical domain from the films grown at 300 ^{o}C (a, d), 400 ^{o}C (b, e), and 500 ^{o}C (c, f). For switching domains, a positive followed by a negative bias (± 15 V) were applied in 3 × 3, 1.6 × 1.6 and 0.8 × 0.8 μm^2 area, alternately. Only the film grown at 400 ^{o}C showed change of contrast with switching the applied bias.

Generally, in ceramic bulk and powder ferroelectric materials, it is observed that as the grain size decreases from micron to submicron scale (d < 1 μm), the saturation polarization as well as the remanent polarization decrease. This decrease can be explained from the decrease in domain wall mobility by a reduced number of domain variants in the fine grains. Therefore, switching domains in this system requires higher electric field because the domains have to switch against their preferred crystallographic orientation relation. This explanation can help understand our observation of paraelectric hysteresis curve with zero remanent polarization and no domain switching in PFM from samples with relatively large grain size grown at 500 ^{o}C. These results are in agreement with previous studies.[92] In general, there is an increase of free energy (ΔF) associated with the formation of nuclei polarized along antiparallel directions which can be expressed by the following equation,

$$\Delta F = -2EP_S V + \sigma_W A + \frac{1}{2} NP_S^2 V$$

where, P_S, σ_w, A, V, and N represent respectively, the spontaneous polarization, surface energy associated with domain wall, surface area, average volume of nuclei, and the depolarizing factor. When the grains are small and contain single domains, the depolarizing factor of each nuclei is negligible. Therefore, the critical nucleation size is determined by the first two terms in the equation for ΔF.

In the case of $BiFeO_3$, when the grain size approaches nano-scale dimensions (d < 150 nm), the films showed different tendency from the films with micron to submicron-sized grains. The films with less than 50 nm grains showed a dramatic increase in polarization as well as uniform domain switching, and as the microstructure approaches the critical domain size, the nano-grains tend to have a

single-domain and the domain wall density is greatly reduced within a grain.[89] This reduction in domain density might lead to a reduction of constraint in switching of the polarization by domains of different orientation.

From the results of electrical polarization and switching of domains, the observed large polarization in crystalline $BiFeO_3$ might be an intrinsic property of $BiFeO_3$ and the switching of ferroelectric domain significantly depends on the grain size when the grains are in the nano-scale. The domain boundaries inside the grains of submicron size might, more significantly, constrain the switching of domain by crystallographically fastening neighboring domains within a grain. Therefore, when grains are in the nano-scale surrounded by amorphous matrix and contain single domain, each domain can switch independently without interference from neighboring domains.

3.6.3 Annealing effects on the microstructure and electrical properties of polycrystalline $BiFeO_3$ films

To understand the effect of nano-grain size on the electrical properties of $BiFeO_3$ films and acquire uniform size and distribution of nanodomains, an annealing process was conducted on the films grown at 300 ^oC, which have semicrystalline microstructure. The films were annealed at 500 ^oC for a period of time in the range 2 to 8 hours at atmosphere to promote nucleation and grain growth.

Figure 3.20 (a) shows an increase in crystallinity with grains of ~ 5 – 10 nm in diameter upon annealing. The grains nucleated in different parts of the film and not

from the interface with the substrate. The grains have random orientation and are fairly uniformly distributed within an amorphous-like matrix [compare with Fig. 3.17 (a)]. As shown in Fig. 3.20 (c), the annealed films show an increase of leakage current density from 5.3×10^{-2} A/cm^2 to 1.4×10^{-1} A/cm^2 after annealing. This increase is mainly due to an increase of grain boundary area and the possibly the formation of oxygen vacancies upon annealing. However, the smaller grains (also domains) increased the electrical polarization compared to the as grown amorphous-like films, by about 10 times (~ 82 μC/ cm^2)

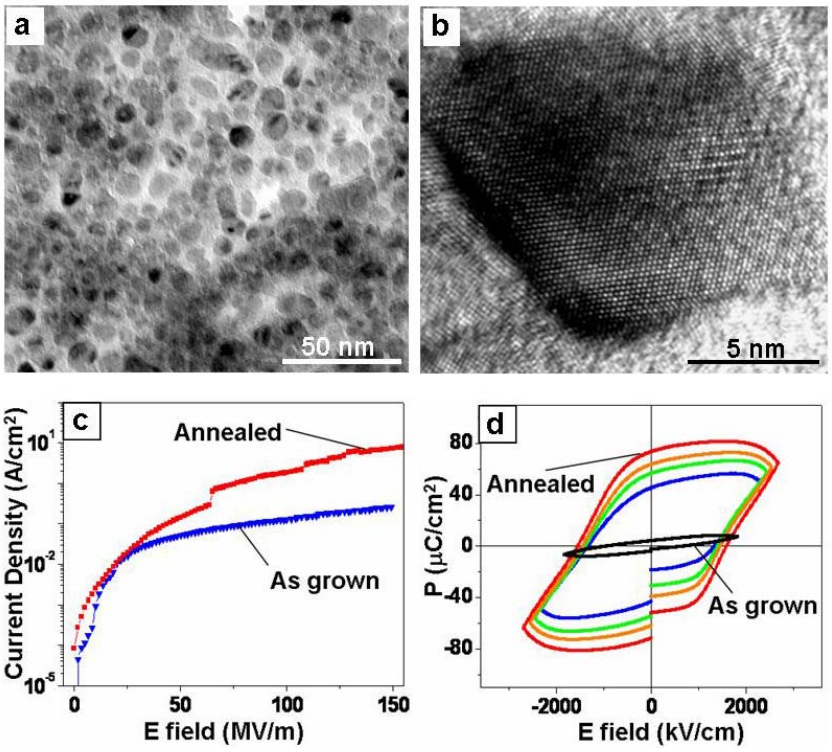

Figure 3.20. (a) Bight-field TEM image and (b) high resolution TEM image showing pure $BiFeO_3$ nanograins with size of 5 – 10 nm diameter after annealing at 500 ^oC for 8 hours. (c) Changes of leakage current and (d) electrical polarization upon annealing. Nucleation of nanodomain structure of polycrystalline $BiFeO_3$ enhanced the polarization, but also increased the leakage current density mainly due to an increase in the area of domain boundaries and evaporation of Bi^{3+} and O^{2-} upon annealing.

Therefore, our annealing results confirmed that the domain size is the most dominant factor for switching the electrical polarization, and the increase in boundary area is responsible for an increase in leakage current in polycrystalline $BiFeO_3$ thin films. Also the observed large polarization and switching in $BiFeO_3$ films with uniform nanoscale-grains (also nanoscale-domains) is important in the context that the nanosize domain structure enables the increase in data storage ability for ferroelectric memory storage devices, which require uniform domain size and shape for reliable writing and reading. However, the domain size for device application still has to be optimized together with the thickness of the film that will require lower operation voltage and leakage current.

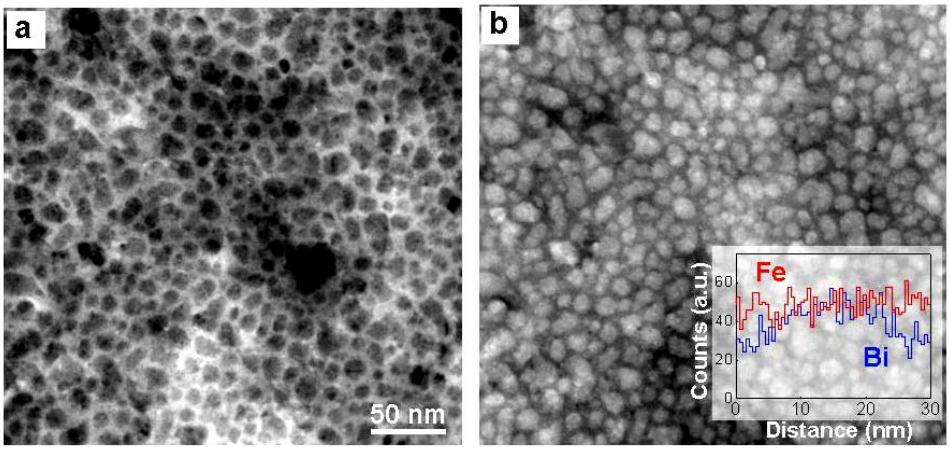

Figure 3.21. (a) Bright field and (b) dark field Scanning TEM (STEM) images from the same area in the annealed poly $BiFeO_3$ film. The inset to (b) represents the chemical composition through one of the grains with ~ 20 nm diameter in size using EDS line scanning.

We performed chemical analysis on the annealed $BiFeO_3$ thin film to investigate if off-stoichiometric phases formed upon annealing. The bright field [Fig.

3.21 (a)] and dark field [Fig. 3.21 (b)] Scanning TEM images were acquired from the same area to analyze the uniformity of the composition distribution. The dark area in the bright field image represents crystallized $BiFeO_3$ nanograins. From the dark field STEM image in Fig. 3.21 (b), this region is brighter in contrast compared to the matrix area, which indicates that this region contains more heavy elements, such as bismuth. An EDS line can was acquired across a grain which is about 10 nm in diameter. The EDS spectra show that the Fe element was fairly uniform both in the grain and the matrix. However, Bi showed slightly higher concentration in the central region of the grain, and the ratio of Bi:Fe was about 1:1 in this region. These results indicate that the matrix region is slightly Bi deficient and contains oxygen vacancies after annealing. The bismuth atoms might be easier to evaporate from the amorphous matrix than in the nucleated grains which fasten bismuth in their crystalline sites in the structure. This could be the reason for the observed higher leakage current together with an increase of grain boundaries in the annealed sample.

The electrical polarization and switching polarization in polycrystalline $BiFeO_3$ thin film with nanodomain size were investigated systematically. The domain size was controlled by varying the growth temperature in the PLD chamber. For small grain size at lower deposition temperature, the leakage current density is higher due to the increase in grain boundary area. Also larger polarization was observed when the $BiFeO_3$ grains are in the nano-scale. From the annealing and chemical analysis on the semicrystalline $BiFeO_3$ thin film grown at 300 ^oC, an increase in electrical polarization was observed because of the nucleation and growth of nano-grains. An increase in grain boundaries coupled with the evaporation of Bi and O during

annealing caused high leakage current density in the annealed films. Based on our results, the domain size is the most dominant factor for switching of electrical polarization and leakage current in polycrystalline $BiFeO_3$ thin films. Our results also suggest that the large polarization observed in polycrystalline $BiFeO_3$ films free of strain and of secondary phases is not induced by strain but it is an intrinsic property of $BiFeO_3$.

3.7 Enhancement of dielectric properties of $BiFeO_3$ films by flux-mediated epitaxy (FME) method

We have fabricated single crystal-like $BiFeO_3$ (BFO) thin films by flux-mediated epitaxy using pulsed laser deposition (PLD). The Bi-Cu-O flux composition and its thickness were optimized using composition spread, thickness gradient and temperature gradient libraries. The optimized BFO thin films grown with this technique showed larger grain size of ~ 2 μm and higher dielectric constant, in the range 260 – 340, than those for standard PLD grown films. In addition, the leakage current density of the films was reduced by two orders of magnitude compared to that of standard PLD grown films.

3.7.1 Introduction of FME method

As mentioned in chapter 1, multiferroic $BiFeO_3$ (BFO) thin films are widely studied because of their antiferromagnetic and ferroelectric ordering well above room

temperature.[57-60] In pursuing their device applications, it is critical to address and control their microstructural variation and the relatively large leakage current primarily due to the high volatility of Bi and heteroepitaxial constraints imposed by the substrate. The strain in the films together with the evaporation of bismuth can produce Bi deficient secondary phases such as antiferromagnetic α-Fe_2O_3, and ferromagnetic γ-Fe_2O_3 and Fe_3O_4 which form to compensate the local imbalance in chemical composition and structural distortion.[61-64] In this section we present the successful use of FME to grow high quality $BiFeO_3$ films by preventing the evaporation of Bi through the use of a CuO-Bi_2O_3 flux. With this technique, we obtained a substantial improvement of leakage current and dielectric properties ($\varepsilon \approx$ 260 – 340) in single crystal-like BFO films grown by flux-mediated epitaxy (FME).

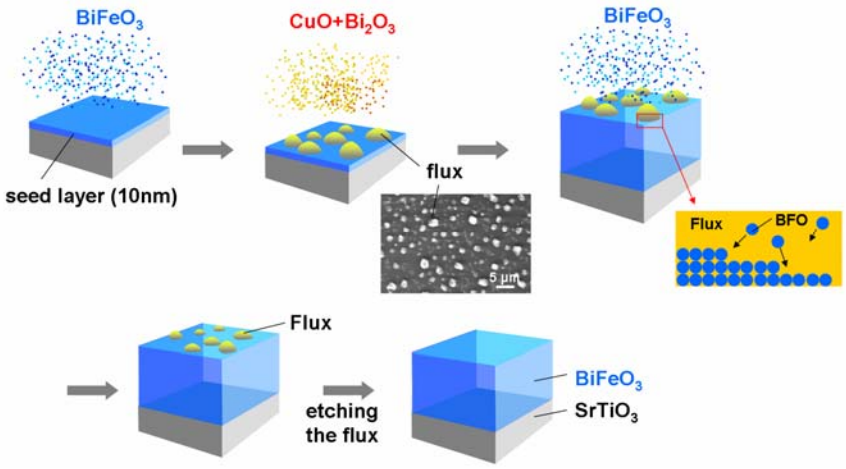

Figure 3.22. FME for $BiFeO_3$ growth. First deposition of $SrRuO_3$ bottom electrode (for electrical measurements) (50 – 80 nm). After the temperature is increased to 650°C, $BiFeO_3$ seed layer (~ 10 nm) is deposited on (001) oriented $SrTiO_3$ by PLD. Then the flux layer of a mixture of (Bi_2O_3 + CuO) is deposited on the seed layer. The temperature is then increased to 730°C, and $BiFeO_3$ is deposited on the flux layer. SEM image shows uniformly distributed flux droplets on the $BiFeO_3$ seed layer with a size ranging 2 – 4 μm diameter. Once the desired thickness of $BiFeO_3$ is deposited the remaining flux is etched off.

As shown in Fig. 3. 22, in the FME method, an oxide flux on the surface of the film plays a key role in improving the crystallinity of complex oxide films.[95] The vapor ablated from the target material by a pulsed laser meets the flux on the surface of the substrate, diffuses into the liquid intermediate phase and finally solidifies on a predeposited seed layer. The liquid phase (flux) prevents direct deposition of the vapor phase on the solid surface, and improves crystallinity. Compared to PLD, in the FME method, there is enhanced diffusion of the surface atoms in the flux above the quasi-melting temperature (~ 0.5 T_m) which leads to film growth in equilibrium even at high growth rates.[99-102]

3.7.2 Combinatorial approach for optimum growth conditions

3.7.2.1 Temperature gradient libraries

The schematic in Fig. 3.23 shows the deposition procedure for the combinatorial library used to optimize the composition, temperature and thickness of the Bi_2O_3-CuO flux. The oxygen partial pressure for the growth of the FME-BFO film was varied in the range of 0.05 to 1 Torr. A BFO seed layer (~ 10 nm) was deposited at 650 ^oC and 30 mTorr oxygen partial pressure before depositing the flux material to lead to growth of BFO. After increasing the temperature to 730 ^oC, a Bi_2O_3 layer (~ 1 nm) and a CuO layer (~ 1 nm) were deposited in an alternating manner to induce interdiffusion between the layers and to prepare a layer with a gradient in composition of the flux. The total thickness of Bi_2O_3 was fixed to 40 nm.

Using a moving shadow mask in the PLD chamber during the deposition of CuO, a layer with a thickness gradient was achieved. These conditions gave rise to regions with different ratios of Bi_2O_3/CuO in the flux which varied from pure Bi_2O_3 (without CuO) to $(Bi_2O_3)_{0.5}$–$(CuO)_{0.5}$. In addition, a temperature gradient from 560 ^oC to 805 ^oC was achieved on the substrate over a distance of 9 mm by heating one side of the sample stage using a semiconductor laser. Following the deposition of the flux, a 300 nm thick BFO thin film was deposited on the flux layer.

Fig. 3.23 (a) shows the intensity map of the (001) BFO diffraction peak as a function of position of the sample which corresponds to changes in CuO layer thickness (0 – 40 nm) and the sample growth temperature. The highest intensity of the (001) BFO peak was observed in the region with CuO thickness of 4.5 – 17 nm and temperature of 710 – 750 ^oC. To understand the effect of CuO on the Bi based flux growth, temperature dependent XRD spectra in the regions with 0 vol% CuO [line I in Fig. 3.23 (a)] and ~ 4.5 nm thick CuO (10 vol% CuO) [line II in Fig. 3.23 (a)] are compared in Figs. 3. 23(b) and (c), respectively. The regions with pure Bi_2O_3 flux show a strong Bi_2O_3 XRD intensity peak over a large range of temperatures below 730 ^oC. This region overlaps with the temperature range for Fe_2O_3 growth [see Fig. 3.23 (b)]. Fig. 3.23 (c) shows that addition of 10 vol% CuO in the flux plays an important role: namely, CuO decreases the melting temperature of the Bi_2O_3–CuO flux material thereby suppressing the precipitation of Bi_2O_3. Furthermore, the amount of Bi_2O_3 melt in the flux compensates for evaporated Bi thus suppressing the formation of Fe_2O_3.[103] The comparison of the shadow areas in Figs. 3.23 (b) and (c) illustrates the enlarged growth window of BFO for a flux with 10 vol% CuO.

Following the combinatorial optimization, a BFO thin film was grown by FME using the optimum flux composition (10 vol% CuO) and the optimized growth temperature (730 ^{o}C).

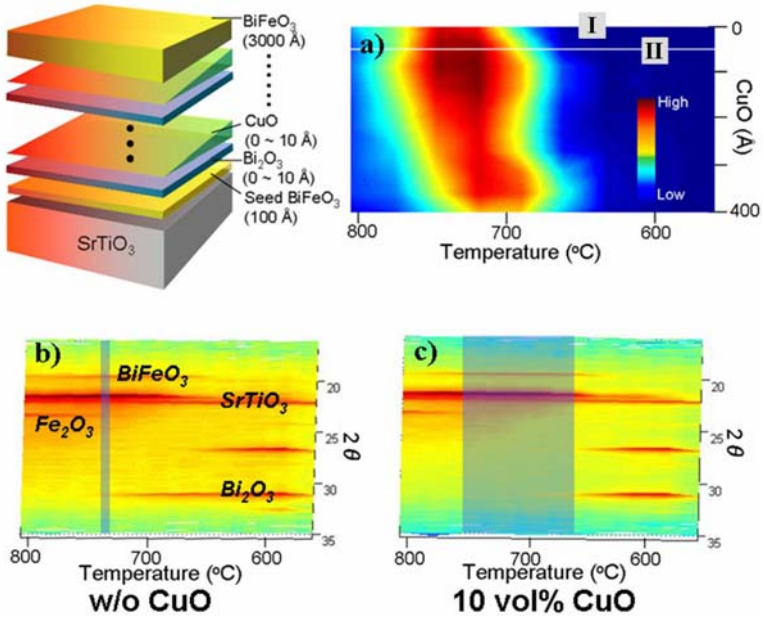

Figure 3.23. Schematic (top left) of the deposition procedure for temperature-gradient combinatorial analysis. The temperatures are varied from 580 to 810 ^{o}C with compositional spread of Bi_2O_3 (400 Å) and CuO (0 ~ 400 Å). (a) XRD map of combinatorial library shows the intensity of the $BiFeO_3$ (001) peak as a function of substrate temperature and flux CuO composition to decide the optimum condition for FME. (b) 2θ x-ray map in the region marked I in (a) for 0 % CuO. (c) Addition of 10 – 30 vol% Cu (XRD mapping result labeled II in (a)) shows highest intensity of the $BiFeO_3$ (001) peak enlarging the growth window of $BiFeO_3$ compared to the film deposited without Cu (labeled (I))

3.7.2.2 Pseudo Ternary composition libraries

To find the optimum amount of flux for the growth of $BiFeO_3$ by FME, we studied a pseudo ternary combinatorial system. The growth temperature of $BiFeO_3$ was fixed at 730 ^{o}C as obtained from temperature gradient combinatorial study

presented in the previous section. As shown in Fig. 3.24, two different shapes of moving shadow masks were used to make composition gradient along three different orientations in a triangle. The schematic in the top left of Fig. 3.24 shows the deposition procedure for the pseudo ternary combinatorial library. First, a 10 nm thick $BiFeO_3$ seed layer was deposited on $SrTiO_3$ at 650 ^oC at 30 mTorr oxygen partial pressure using standard PLD growth. Then, alternating layers of a Bi_2O_3 layer (~ 10 Å) and a CuO layer (~ 10 Å) were deposited to induce interdiffusion between the different layers and to make variant composition of flux. The total thickness of Bi_2O_3 and CuO varies from 0 to 400 Å, respectively. Then, the temperature was increased to 730 ^oC, and a thicker layer of $BiFeO_3$ with constant thickness (3000 Å) was deposited on the flux.

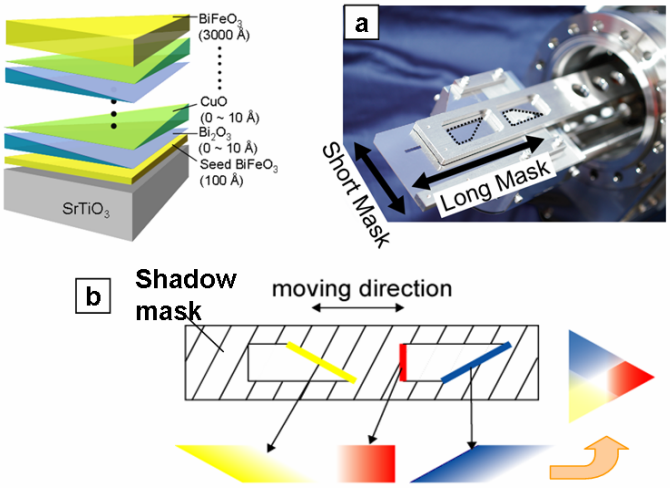

Figure 3.24 Schematic (top left) of the pseudo ternary composition spread procedure. (a) the picture and (b) schematic of the shadow mask used in combinatorial PLD system.

Figure 3.25 (a) shows an optical image of the real surface taken from the specimen of Bi_2O_3-CuO-$BiFeO_3$ ternary system. Scanning x-ray micro-diffraction

maps were obtained from the region inside the white triangle in (a). The 2-dimensional and 3-dimensional graphic images of the x-ray diffraction intensity of the (001) $BiFeO_3$ peak shown in Figs. 3.25 (b) and (c) indicate that the highest intensity for the 2 theta angle of $BiFeO_3$ is found in the region with high Bi_2O_3. Therefore, addition of small amount of CuO improved the crystallinity of $BiFeO_3$ thin film, which is coincident with the results obtained from the temperature gradient combinatorial study. From these combinatorial approaches, the optimum growth conditions were decided. We selected 730 ^oC for the growth temperature and ~ 45 Å thick CuO (10 vol% CuO) and 400 Å thick Bi_2O_3 for flux, and deposited a 3000 Å $BiFeO_3$ thin film on the flux.

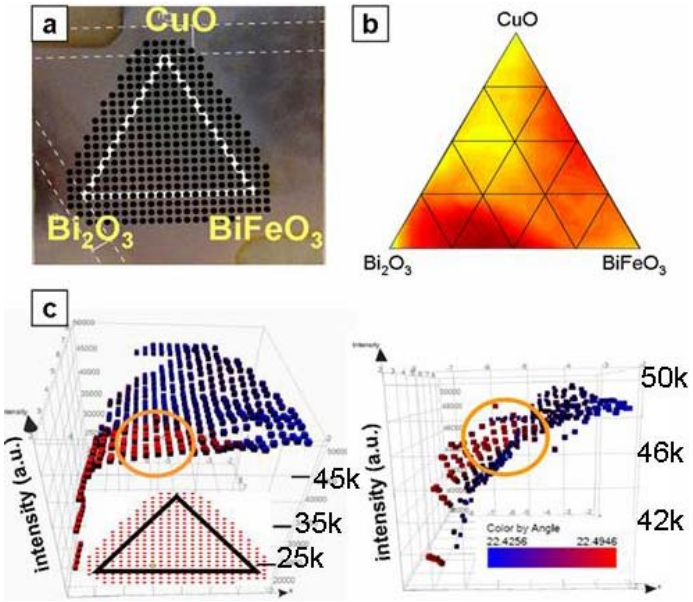

Figure 3.25. (a) The specimen of Bi_2O_3-CuO-$BiFeO_3$ ternary system. (b) 2-dimensional and c) 3-dimensional x-ray maps for the diffraction intensity and 2 theta angles of $BiFeO_3$ peak.

3.7.3 Enhanced structural and dielectric properties

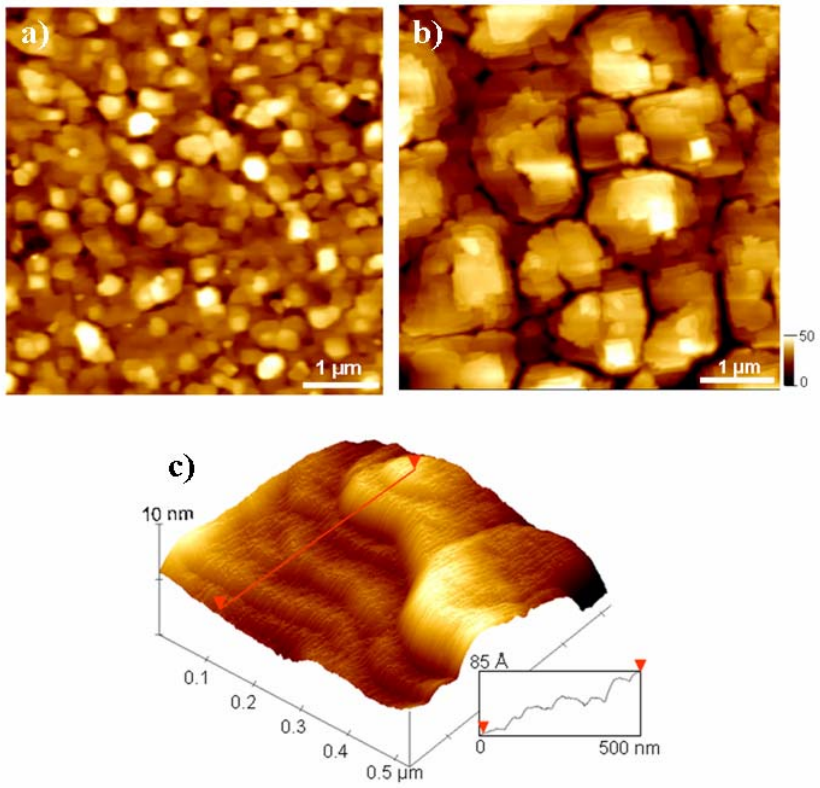

Figure 3.26. Atomic force microscopy images taken from 5 µm × 5 µm area of $BiFeO_3$ thin films grown (a) by conventional PLD and (b) by FME method. (c) The 3-D image of magnified $BiFeO_3$ domain in (b) shows atomic steps during growth of the film with grain size of ~ 2 µm (~ 10 times larger than that of $BiFeO_3$ grown by normal PLD).

The AFM image in Fig. 3.26 (b) shows much increased grain size (~ 2 µm) for the FME grown BFO film, which is more than 10 times larger than the grain size for films grown by standard PLD [shown in Fig. 3.26 (a) with typical grain size of 50 – 200 nm]. The height profile of the FME grown BFO film [Fig. 3.26 (c)] shows a fairly smooth surface (compared to the standard PLD grown BFO films) with an average step height of approximately 1.2 nm, which corresponds to 3 unit cells of

BFO [see inset to Fig. 3. 26 (c)]. The width of the terraces varies in the range from 70 to 100 nm.

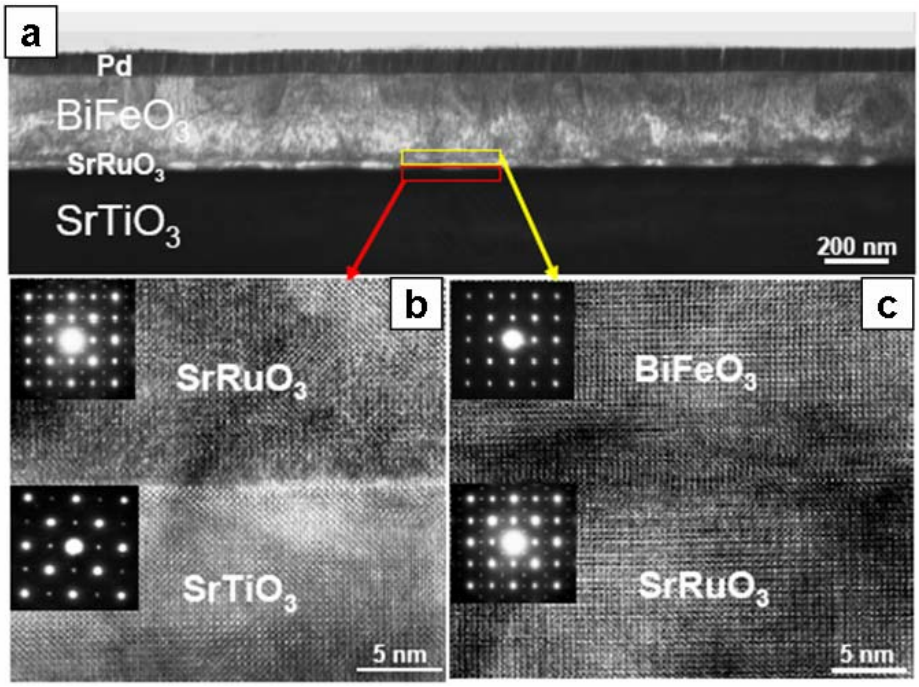

Figure 3.27. (a) Cross-sectional bright field TEM image showing smooth surface of the $BiFeO_3$ film which was grown on $SrRuO_3$ buffered (001) oriented $SrTiO_3$. 1000 Å thick palladium (Pd) was used as the top electrode. The high resolution lattice images of (b) interface between $SrTiO_3$ and $SrRuO_3$ and (c) interface between $SrRuO_3$ and $BiFeO_3$ show epitaxial growth. The corresponding diffraction pattern from each layer is shown as inset in (b) and (c)

A cross-sectional bright field TEM image (top) and high resolution images (bottom) of the FME grown BFO film in Fig. 3.27 exhibit epitaxial growth with very sharp interfaces and smooth surface of the BFO film. In the large area view [Fig. 3.27 (a)], the film grown by FME shows single crystal-like BFO film without grain boundaries, and we see no evidence of bismuth deficient secondary phases such as Fe_2O_3 (α- or γ-), or Fe_3O_4 as we have observed in films grown by PLD at low oxygen

partial pressure (see section 3.2).[62,63] The lattice constants of the BFO film determined from XRD and electron diffraction patterns are $a = b = 0.394$ nm (in-plane), and $c = 0.397$ nm (out-of-plane). These values indicate that the film grown by FME still suffers from some residual compressive strain (– 0.9 %), originating from the lattice mismatch (– 1.15%) between the substrate and the film, even though the film was grown under a quasi-equilibrium condition facilitated by the flux.

Figure 3.28 (a) shows the dielectric constant (ε) of BFO thin films grown by FME method (labeled 'FME-BFO') and by the standard PLD technique (labeled 'PLD-BFO') as a function of frequency. The dissipation factor (tan δ) values of the FME-BFO film and (100) oriented PLD-BFO film were 0.011 ± 0.009 and 0.012 ± 0.01, respectively, in the frequency range of 10 kHz – 10 MHz at room temperature. The dielectric constant values of the PLD-BFO thin films varied from 80 – 130 depending on the frequency and crystalline orientation of the films. These values are slightly higher than the values reported for bulk BFO.[104,105] In contrast, the dielectric constant of FME-BFO films is 3 times as large (260 – 340) as that of PLD-BFO films. This may be due to the enhanced crystallinity with the large grain size (~ 2 μm) in the FME grown films. The leakage current density of FME-BFO thin films is also improved by two orders of magnitude compared to that of PLD-BFO films at applied electric fields of up to 100 MV/m as shown in Fig. 3.28 (b). X-ray photoelectron spectroscopy analysis (not shown here) from a PLD-BFO film did not show any significant amount of Fe^{2+} ions which could explain leakage by double exchange interaction among Fe^{2+}–O^{2-}–Fe^{3+} ions. Therefore, the concentration of Fe^{2+} ions cannot be the dominant reason for the high leakage current in the PLD-BFO

films. One possible reason for the leakage current in PLD-BFO films could be the larger fractional area of grain boundary regions in these films, which allow current to pass through with less resistance than in the bulk of the grains. Another possibility is that oxygen vacancies and Bi deficiency in PLD-BFO induce impurity energy levels in the band gap that increase free carrier density by hopping of electrons to these defect levels.[106]

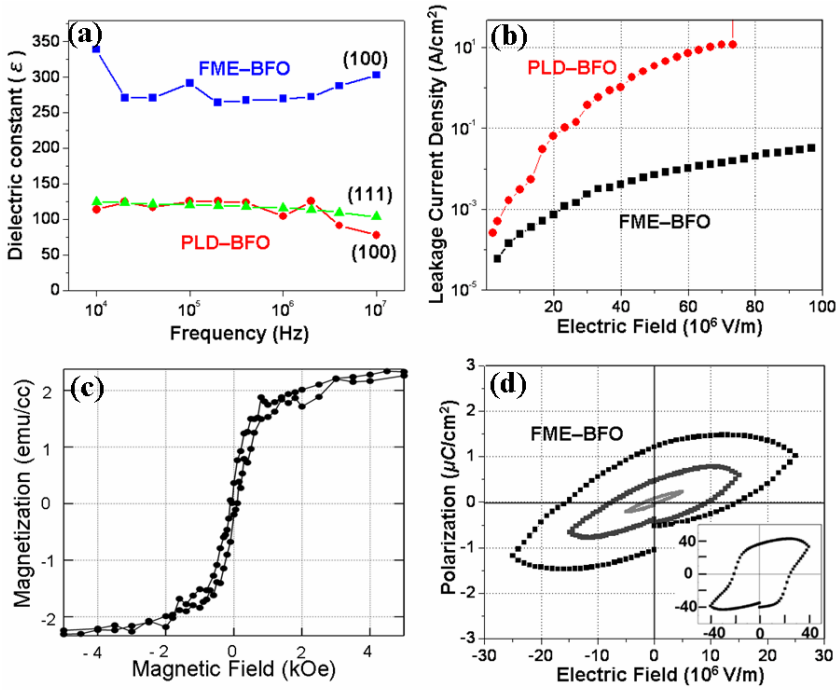

Figure 3.28. (a) Dielectric constant of $BiFeO_3$ thin films fabricated by typical PLD method on SrTiO3 (100) and (111), and by flux method on SrTiO3 (100) as a function of frequency (10 kHz – 10 MHz). (b) Leakage current density (A/cm2) vs. electric field (MV/cm) curves of $BiFeO_3$ thin films fabricated by typical PLD and flux method. (c) Magnetic hysteresis curve (in-plane) of $BiFeO_3$ thin film fabricated by flux method. (d) Electric field dependence of polarization loops of $BiFeO_3$ thin film fabricated by flux method measured at 1 kHz. The inset in (d) is the P-E loop from a PLD grown film.

In summary, we improved the crystallinity of $BiFeO_3$ films by flux-mediated epitaxy. For the FME growth, we optimized the growth conditions by the combinatorial method. The FME grown films exhibited single crystal quality with large grain size (~ 2 μm) and a flat surface as well as higher dielectric constant and lower leakage current than films grown by standard PLD. However, the P-E loop showed unsaturated polarization even for field of 25×10^6 V/m. (Fig. 3.28(d)). Also, the magnetization in the FME-BFO films was low as shown in Fig. 3.28(c).

Chapter 4

4. Application the ME effects for spintronic device application

4.1 Introduction of exchange bias

Many multiferroic materials exhibit antiferromagnetic (AFM) properties.[70,71] Therefore, one important application of these materials is related to exchange bias.[72] Exchange bias is the phenomenon associated with the exchange anisotropy created at the interface between an AFM layer and a ferromagnetic (FM) layer. Possible applications of exchange bias are domain stabilizer in recording heads based on anisotropic magnetoresistance or magnetic recording. The combination of exchange bias and magnetoelectric (ME) effects could allow control of exchange bias by an electric field. The ME controlled exchange bias was first reported in a Cr_2O_3 crystal and Co bilayer system.[102]

Exchange bias was discovered in 1956 by Meiklejohn and Bean in FM Co particles embedded in a CoO (AFM) matrix.[103] Generally, exchange bias results in the horizontal shift in the magnetization-magnetic field (M-H) hysteresis loop due to the pinned FM phase at the interface between a FM and an AFM phase layer when the materials are cooled in the presence of a static magnetic field through the Néel temperature (T_N) of the AFM layer which is lower than the Curie temperature (T_C) of the FM material. After the field cool procedure, the M-H loop is shifts along the field

axis in the opposite direction to the cooling field. Also the coercive field of the system increases after this cooling procedure.

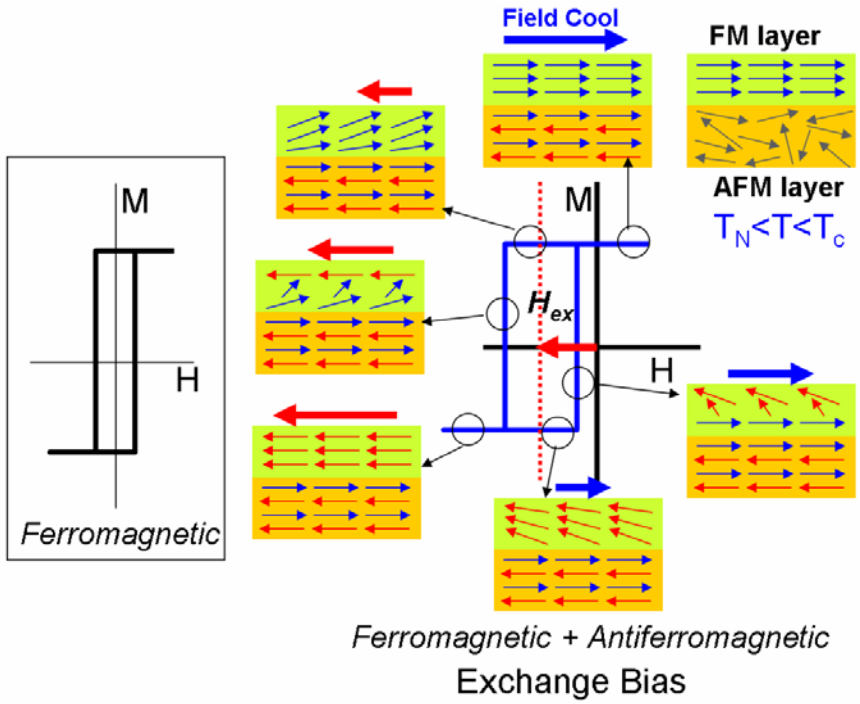

Figure 4.1. (a) Typical shape of M-H hysteresis loop of ferromagnetic materials. (b) Schematic diagram of the spin configuration of FM-AFM bilayer

Figure 4.1 shows a schematic diagram of the spin configuration in a FM-AFM bilayer structure. When a field is applied in the temperature range $T_N < T < T_C$, the FM spins align with the external field, while the AFM spins remain random. When cooling to $T < T_N$, the AFM spins next to the FM interface align along the direction of ferromagnetic spins due to the interaction at the interface. The other spins in the AFM material follow AFM order giving zero net magnetization.

When the field is reversed, the spins in the AFM try to keep the spins in the FM layer in their original direction (ferromagnetically aligned at the interface).

Because of this interfacial interaction, an extra field (H_{ex}) is needed to reverse spins in the FM layer. However, when the field is applied in the original direction, the spins in the FM would start to rotate at a lower field due to the interaction with the spin in the AFM. From these interfacial interactions between AFM and FM in the presence of an external field, the M-H hysteresis loop of the bilayer is shifted from the origin and has increased coercivity.

In the opposite case, when the coupling of FM-AFM at the interface has an antiferromagnetic order at the initial stage, the magnetic spins in the FM layer can change direction when the field is reversed below T_N. However, when the field is reversed to the original direction, a higher field is needed to switch the spins due to the ferromagnetic alignment at the interface. This behavior is called the positive exchange bias. In positive exchange bias, the M-H hysteresis loop shifts along the field axis in the same direction as the cooling field.

4.2 Control of magnetic moment and exchange bias in Cr_2O_3

Cr_2O_3 is a Heisenberg antiferromagnet (AFM) showing antiferromagnetic ordering of Cr^{3+} spins aligned along the *c* axis of its rhombohedral unit cell below the Néel temperature (T_N = 308 K).[104] Cr_2O_3 was the first compound in which the magnetoelectric (ME) effect was theoretically predicted and experimentally observed.[105-108] Recently, the ME effect on exchange bias was observed on a Co/Pt multilayer on a *c*-axis oriented Cr_2O_3 single crystal.[109,110] Such an effect

can be the basis for new type of memory and logic devices where both electric and magnetic fields serve as external control parameters.

Thin film multilayer devices are desirable over bulk since rather large electric fields can be applied to the AFM layer, and thus the ME effect on exchange bias is expected to be larger. To this end, in our study, we have fabricated Co/Pt multilayers on Cr_2O_3 thin films with extremely smooth interfaces. Out-of-plane magnetized exchange-biased dual hysteresis loops were clearly observed. Detailed features in the loops were found to be delicately controlled by demagnetizing ac magnetic field with different amplitude offset during magnetic field cooling (MFC). The effect of high electric field (~ 77 MV/m) cooling (EFC) as well as direct electric field *E* at a fixed temperature after magnetic field cooling were investigated.

130-nm thick Cr_2O_3 thin films were grown on Al-doped ZnO (Al-ZnO) buffered *c*-axis oriented sapphire (Al_2O_3) substrates by pulsed laser deposition. Cr_2O_3 and Al-ZnO targets were ablated using a KrF excimer laser with a typical fluence of 2 J/cm^2. The epitaxial Al-ZnO (170 nm) layer was used for the bottom electrode to apply an electric field on the Cr_2O_3 thin film, and [Co (~ 0.3 nm)/Pt (~ 1.5 nm)]$_3$ layers were deposited alternately on the Cr_2O_3 layer by electron-beam evaporation at 500 K. Pt (~ 0.5 nm) was the first layer deposited to prevent oxygen diffusion from Cr_2O_3 and subsequent potential formation of antiferromagnetic CoO.[111] To characterize the microstructure of the multilayer, phi (φ) scans and theta (θ) scans were performed with a 4-circle x-ray diffractometer (Bruker D8 Discover). Transmission electron microscopy (TEM) images and selected area diffraction (SAD) patterns of the films were obtained at an accelerating voltage of 200 keV with a JEOL

2100F field emission TEM. The Co/Pt multilayer atop the Cr_2O_3 layer was patterned into 200 μm × 200 μm square dots by ion milling to make capacitor devices. A magneto-optical Kerr effect (MOKE) system was used to detect the Kerr rotation of Co spins in the Co/Pt multilayer and measure the hysteresis loops directly on individual capacitor devices.

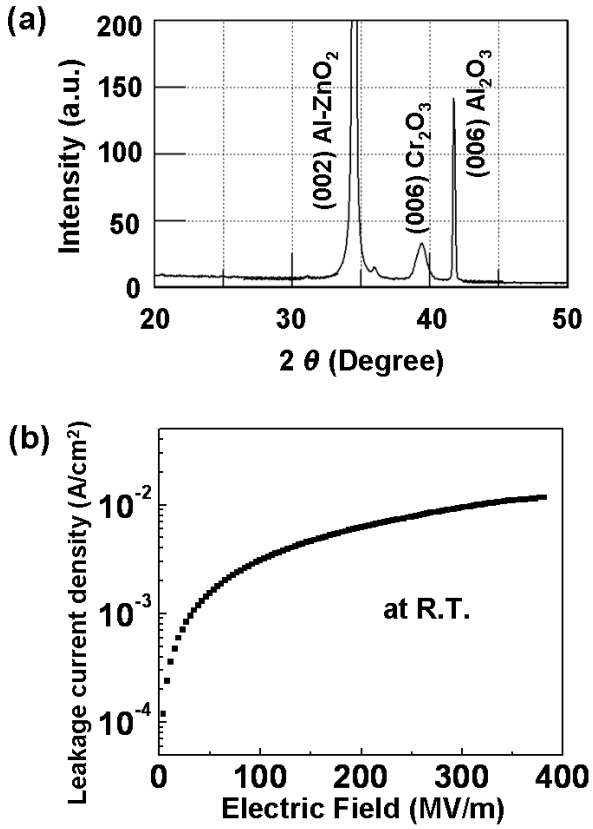

Figure 4.2. (a) XRD 2-theta scan of a Co/Pt/Al-ZnO/Cr_2O_3 film. (b) Leakage current density of Cr_2O_3 film measured using Pt (top) and Al-ZnO (bottom) electrodes at room temperature.

The $\theta - 2\theta$ x-ray diffraction (XRD) spectrum in Fig. 4.2 (a) shows that the Al-ZnO and Cr_2O_3 layers, which have the hexagonal and rhombohedral crystal structures, respectively, grew *c*-axis oriented on the (001) oriented Al_2O_3 substrate,

which has a rhombohedral crystal structure. The sheet resistance of the Al-ZnO bottom electrode layer was less than 10 kΩ. The Cr_2O_3 film showed sufficient insulation for applying a high electric field. As shown in Fig. 4.2 (b), the leakage current density of the Cr_2O_3 film measured at room temperature was ~ 10^{-2} A/cm^2 even for electric fields as high as 380 MV/m at room temperature. This allowed us to apply up to ± 100 MV/m continuously without breakdown.

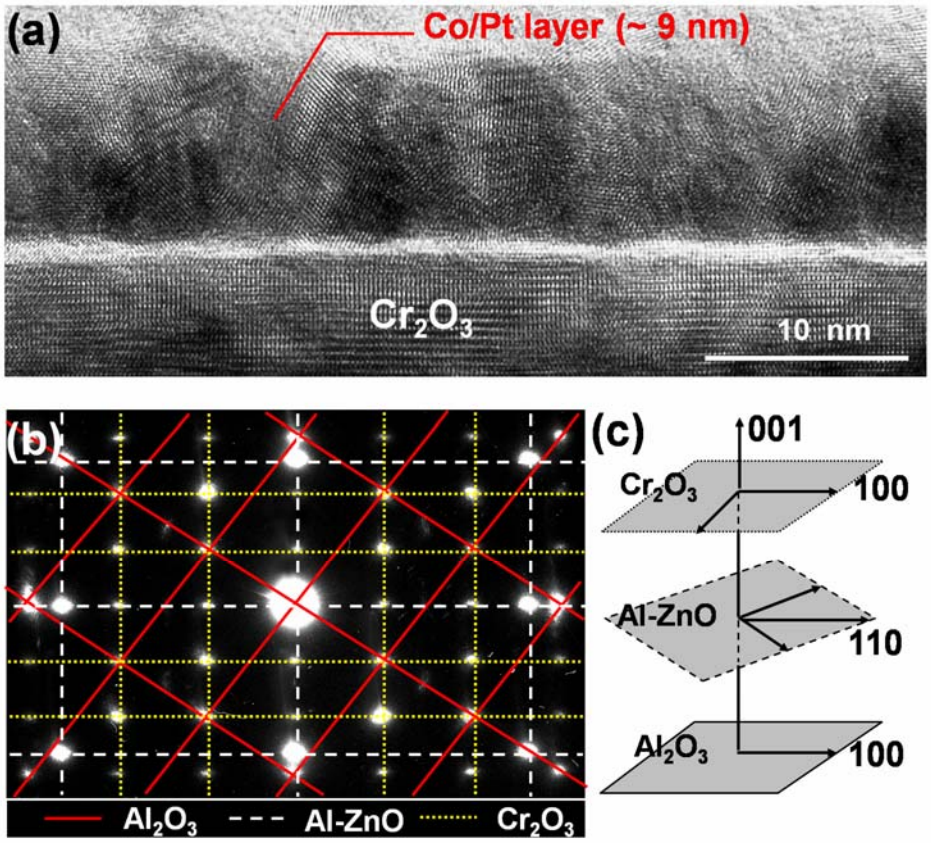

Figure 4.3. (a) High-resolution TEM image of Co/Pt layer/Cr_2O_3 interface. Co particles were embedded in a Pt matrix. The thickness of Co/Pt layer was ~ 10 nm. (b) Electron diffraction pattern and (c) schematic of the crystal orientation relation of the Cr_2O_3/Al-ZnO/Al_2O_3. The film showed epitaxial growth of Al-ZnO and Cr_2O_3 layers on *c*-axis sapphire substrate.

As shown in the electron diffraction pattern in Fig. 4.3 (b) and the schematic in Fig. 4.3 (c), the Cr_2O_3 and Al-ZnO layers grew epitaxially on the (001) oriented Al_2O_3 substrate. The growth orientation relationship between the layers indexed from the diffraction pattern is $[001]_{Al2O3} \parallel [001]_{Al\text{-}ZnO} \parallel [001]_{Cr2O3}$ along the out-of-plane direction and $[100]_{Al2O3} \parallel [110]_{Al\text{-}ZnO} \parallel [100]_{Cr2O3}$ along the in-plane direction [Fig. 4.3 (c)].

The interface roughness between the ferromagnetic (FM) and AFM layers is known to influence the AFM spin configuration and cause complex exchange bias behavior affecting the exchange bias field (H_E) and the coercive field (H_C).[112] In our sample, the Co/Pt layer on the Cr_2O_3 layer showed a continuous structure with a sharp interface over the whole lateral range (several hundred microns) visible in the TEM sample of the film which we attribute to the extremely smooth surface of the Cr_2O_3 layer. The surface roughness (root mean square) of a Cr_2O_3 layer deposited on an Al-ZnO film (170 nm) measured by atomic force microscopy was ~ 0.3 nm over a 10×10 $(\mu m)^2$ area. The selected area diffraction pattern (not shown here) obtained from the Co/Pt multilayer [Fig. 4.3 (a)] indicated that the multilayer was polycrystalline.

Figure 4.4 (a) shows the out-of-plane hysteresis loop of our (Co/Pt)/Cr_2O_3 structure at room temperature after magnetic-field cooling (MFC) through the Néel temperature following heating of the sample to 325 K, where H_C of the Co/Pt layer was 15 Oe. We found clear exchange bias with cooling in a field of only 20 Oe. As the temperature decreased from 325 K to 298 K, H_E was seen to gradually increase to ~ 170 Oe, and the sign of H_E was consistent with the direction of the applied field and

the AFM layer and the FM layer having ferromagnetic coupling. Even at 298 K, with the exchange bias present, H_C of Co remained narrow at 15 Oe. As the magnetic field was reversed (– 20 Oe) during MFC, H_C of the Co/Pt layer switched sign from the negative to positive side as shown in Fig. 4.4 (b). These results indicate that the applied magnetic field aligned the soft (Co) layers during MFC, and the configuration of the magnetic moments in this layer duplicated the pattern of the very top layer of Cr_2O_3 layer (see schematics in Fig. 4.4).

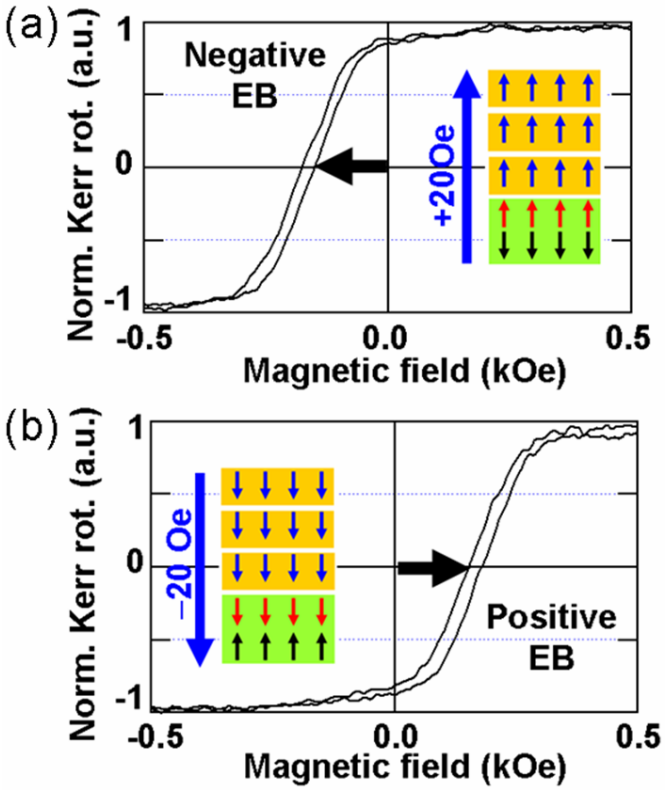

Figure 4.4. (a) and (b) show the out-of-plane hysteresis loops of our (Co/Pt)/Cr_2O_3 structure at room temperature after magnetic-field cooling (MFC) through the Néel temperature following heating of the sample to 325 K, where H_C of the Co/Pt layer was 15 Oe. We found clear exchange bias with cooling in a field of only 20 Oe. As the temperature decreased from 325 K to 298 K, H_E was seen to gradually increase to ~ 170 Oe, and the sign of H_E was consistent with the direction of the applied field. Even at 298 K, with the exchange bias present, H_C of Co remained narrow at 15 Oe.

As shown in the schematic in Fig. 4.5 (a), we found that we could control the overall configuration of the magnetic moments of the interface Co and Cr_2O_3 layers by an applied magnetic field during the MFC process for tunable exchange bias and hysteresis loops. Dual hysteresis loops result from an uneven up/down spin fraction set up in the AFM layer at the interface.[113] To achieve this, we have superimposed a slow (0.02 Hz) ac field with a constant amplitude of 0.7 kOe with dc offsets of either 0, ± 0.02, or ± 0.2 kOe [see Fig. 4.5 (a)]. The ac field during the cooling process (~ 30 minutes) provided a demagnetizing effect on the Co/Pt layer, and the dc offset created an uneven up/down spin fraction depending on its sign and amplitude.

Figure 4.5 (b) shows that for the + 0.2 kOe offset case, the ac magnetic field was made to oscillate between + 0.9 kOe and – 0.5 kOe. The net positive magnetic field swing (+ 0.4 kOe) in this case should be sufficient to saturate and align all magnetic spins of the Co layer along the positive field direction. This leads to the Co magnetic moments imprinting their homogenous magnetic spin orientation into the very top layer of spins of the AFM Cr_2O_3 during cooling and results in a fully uncompensated interface and a negative H_E. Similarly, in the – 0.2 kOe offset case, the magnetic field is swept between + 0.5 and – 0.9 kOe with a net negative magnetic field (– 0.4 kOe) which aligns all magnetic spins along the negative field direction resulting in a positive value of H_E.

For the case of zero offset, the magnetic field oscillates between + 0.7 kOe and – 0.7 kOe. After cooling, a dual hysteresis loop is observed. This is marked as "zero offset" in Fig. 4.5 (b). In this case, the demagnetizing process is consistent with domains in the Co/Pt multilayers such that there are equal numbers of up and down

spins. Upon cooling, these domains are imprinted onto the very top layer of Cr_2O_3. They in turn result in exchange biasing "half" of the Co spins in one direction while the other half is biased in the opposite direction,[113] giving rise to the double loop. For the intermediate offset values [± 0.02 kOe in Fig 4.5 (b)], uneven distributions of up and down magnetic domains become imprinted on the top layer of Cr_2O_3 resulting in vertically asymmetric dual hysteresis loops reflecting the distributions. Thus, by adjusting the dc field offset, we can tune the shape of the dual hysteresis loop.

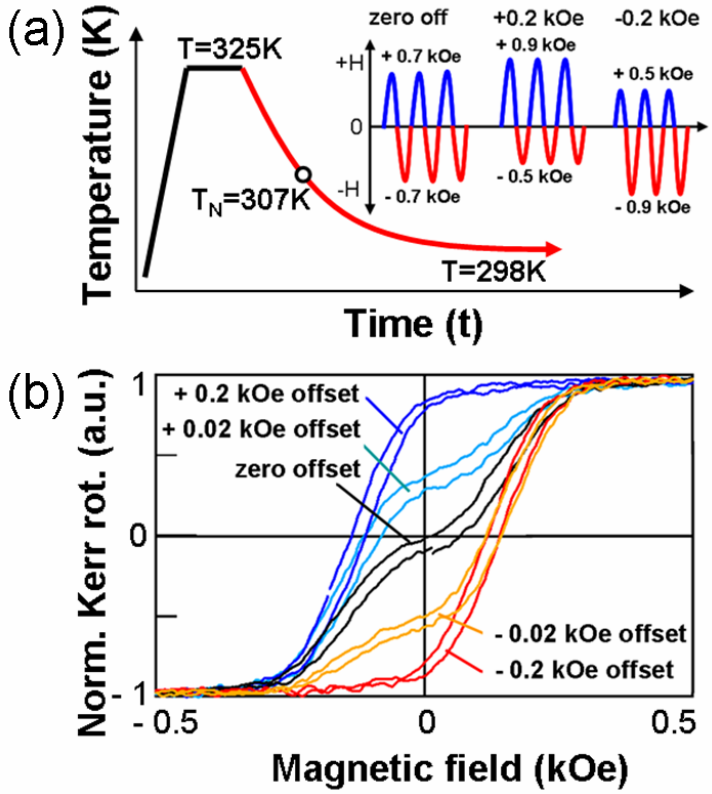

Figure 4.5 (a) The schematic of magnetic field cooling process with sweeping the magnetic field with various offsets and (b) Control of magnetic hysteresis by sweeping the magnetic field with various offsets during magnetic field cooling. The hysteresis loops gradually change from – H_E to + H_E and also from single loop to dual loop by changing offset from + 0.2 kOe to – 0.2 kOe.

4.3 Magnetoelectric effect on exchange bias in Cr_2O_3

To investigate the ME effect on exchange bias in the thin-film devices, the hysteresis loops were compared after different (simultaneous) magnetic and electric field cooling (MEFC) conditions (magnetic field = 0.7 kOe and E = ± 77 MV/m). Based on previous measurements of the ME susceptibility (tensor) in Cr_2O_3, we have performed the MEFC down to 250 K in order to maximize the ME effect in Cr_2O_3.[114] Typical H_E was 550 Oe in the Co/Pt multilayer at this temperature. However, no difference in the shape of the dual hysteresis was detected for the two MEFC conditions. Given the sensitivity of our measurement set up, we place the upper bound in the shift of the H_E to be less than 5 Oe. In addition, we have also looked for direct electric field effect under different constant magnetic field values (0, ± 0.13 kOe) at 298 K. We applied an ac electric field and used lock-in detection of the Kerr signal and found no detectable changes in H_E (sensitivity ~ 1 Oe) or magnetic moment (sensitivity better than 1% of total Co/Pt moment).

Thus, despite the fact that we have been able to apply electric field about 150 times higher than that used in the previous experiment on a Cr_2O_3 single crystal,[110] the apparent ME effect on the exchange bias appears to be minimal. One possible reason for the lack of electric field effect is that the magnetic spin orientations of the very top AFM layer in Cr_2O_3 are mostly affected by the magnetic spin configuration of the Co layer through exchange interaction rather than the ME effect in Cr_2O_3. Investigation of the possible ME effect on other exchange-biased AFM-FM multilayer multiferroic systems is also currently underway.

Chapter 5

5. Dynamic observation of ME effect using Lorentz TEM

The mutual control of magnetic and electric ordering in multiferroic (or magnetoelectric) materials recently has been reinvestigated because of its increasing potential for the applications in magnetoelectric (ME) or spintronic memory devices and sensors.[72-75] The keystone of these applications is based on the combination of magnetism and electricity using, for example, spin-polarized carrier effects and giant magnetoresistance (GMR) effects. Another possible application is to further increase the storage ability by tuning magnetic or electric properties in a multiferroic material by ME coupling effects.

In most cases the correlations between magnetism and electricity in ME materials have been evaluated from either magnetic field-induced voltage / electrical polarization ($P = \alpha H$) or electric field-induced magnetization ($M = \alpha E$). There has also been a report on the observation of the change in magnetization in a ferromagnetic layer upon an applied electric field on a multiferroic layer.[115] This report demonstrated change of magnetization in a CoFe layer due to an exchange type of interaction with $BiFeO_3$ which is antiferromagnetic. The change was produced when an electric field changed the direction of polarization in the $BiFeO_3$ layer. This change in polarization induced a change in the orientation of the magnetic moments in the $BiFeO_3$ layer. This last change gave rise to an exchange interaction with the CoFe layer. However, there has been no evidence, so far, for the direct observation of strain-mediated ME coupling, especially, control of magnetic domains by strain

induced from both magnetic and/or electric fields. This is a very important mechanism for ME memory storage devices. There are several difficulties that have prevented the observation of strain-mediated ME coupling. The main problems are the difficulty in applying a strong enough electric field for the bulk samples and clamping effect from the substrate that exists in thin film structures. Here, we describe direct observation of strain-mediate ME coupling in an unconstrained bilayer using in-situ Lorentz transmission electron microscopy. The strain propagation and reversible switching of magnetic domains in a ferromagnetic layer were dynamically observed under an applied electric field to a ferroelectric layer.

5.1 Strain-mediated ME effect using Fe-Ga/$BaTiO_3$ bilayer

For this experiment, we used a bilayer thin film structure of a ferromagnetic (magnetostrictive) phase and a ferroelectric (piezoelectric) phase. Firstly, for the ferroelectric layer, a 200 nm thick $BaTiO_3$ thin film was deposited on a $SrTiO_3$ substrate at 760 ^oC and 100 mTorr oxygen pressure using PLD. As shown in the X-ray diffraction spectrum in Fig. 5.1 (a), the $BaTiO_3$ film was heteroepitaxially grown on (001) $SrTiO_3$. $BaTiO_3$ is a ferroelectric material with a perovskite structure. The saturation polarization measured from a separately made $Fe_{0.7}Ga_{0.3}$(top electrode)/$BaTiO_3$/$SrRuO_3$(bottom electrode)/$SrTiO_3$ was $P_S \sim 17\ \mu C/cm^2$, and the remanent polarization was $Pr \sim 7\ \mu C/cm^2$ [see Fig. 5.1 (b)]. The piezoelectric coefficient measured for these films was $d_{33} = \sim 50$ pm/V.[118]

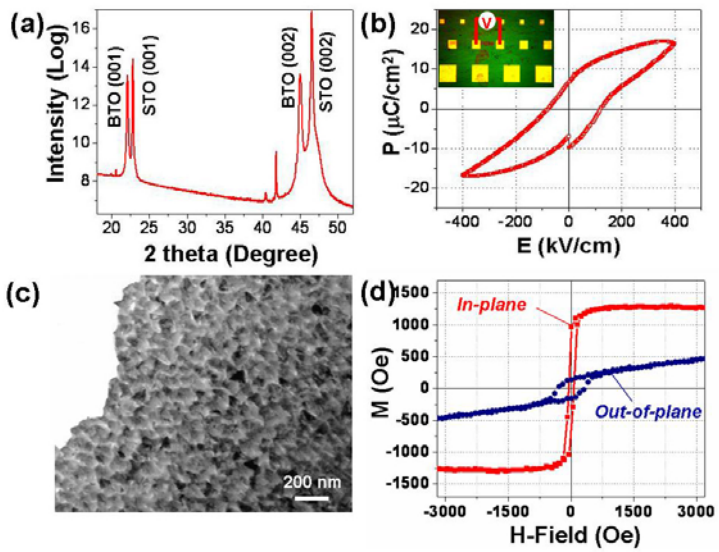

Figure 5.1 (a) X-ray diffraction spectrum showing epitaxial growth of $BaTiO_3$ thin film on (001) oriented $SrTiO_3$. (b) Electrical polarization versus applied electric field showing ferroelectric hysteresis curve of $BaTiO_3$. (c) Bright field TEM image of polycrystalline $Fe_{0.7}Ga_{0.3}$ thin film. (d) M-H hysteresis curves obtained from the 600nm thick Fe-Ga thin film along the out-of-plane and in-plane directions.

Over the $BaTiO_3$ film we deposited a 60 nm thick polycrystalline film of $Fe_{0.7}Ga_{0.3}$ for the FM layer by magnetron sputtering at room temperature. This layer was also used as top electrode for the application of voltage to the $BaTiO_3$ layer. As shown in the bright field TEM image in Fig. 5.1 (c), the grain size of the polycrystalline Fe-Ga film was about 50 nm in diameter. The in-plane and out-of-plane magnetization were obtained from a thicker Fe-Ga film (600 nm) using a vibrating sample magnetometer (VSM). The film showed strong magnetic anisotropy along the in-plane direction, and the anisotropy increased for films with smaller thickness. $Fe_{0.7}Ga_{0.3}$ is known to show relatively large magnetostriction. The magnetostrictive coefficient (λ_{eff} = ~ 150 ppm for thin film) was measured at room temperature by measuring the change of length along the magnetic field after

applying a magnetic field and saturating the magnetic moments from a film deposited on a cantilever.

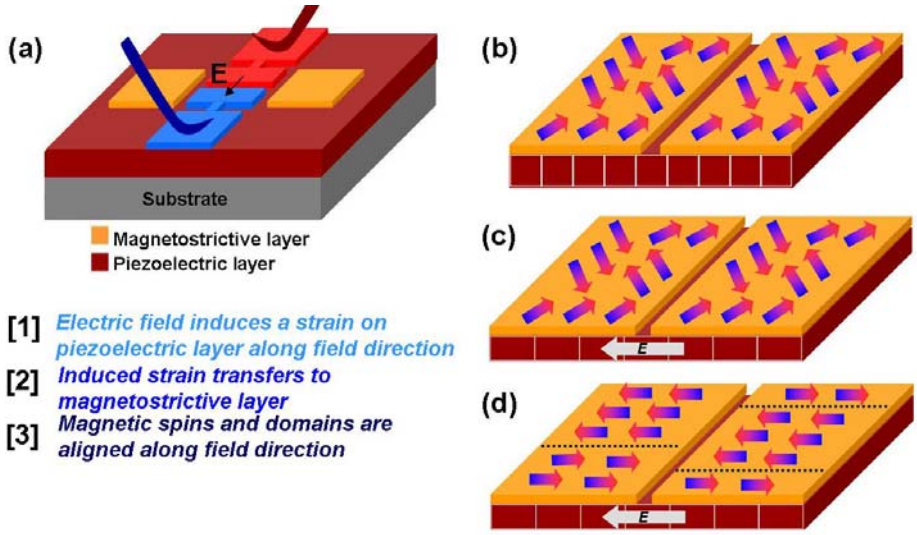

Figure 5.2 (a) Schematic for Lorentz TEM sample preparation. After deposition of FE and FM bilayer thin film structure, FM layer was patterned using optical lithography and electron beam lithography to apply an electric field. Schematics of (b) randomly oriented magnetic domains in the initial state, (c) induced tensile strain along field direction after applying an electric field (E), and (d) alignment of magnetic domains along tensile strain direction.

As shown in Fig. 5.2 (a), to apply an electric field along an in-plane direction, the conducting Fe-Ga layer was used as electrodes after patterning using photo-lithography and electron-beam lithography. To eliminate the clamping effect from the substrate, we removed the $SrTiO_3$ substrate from a 10 × 10 μm^2 window area using focused ion beam (FIB) milling and prepared a thin TEM sample to apply an electric field in the Lorentz TEM. $BaTiO_3$ and Fe-Ga are known to have positive values in piezoelectric and magnetostriction coefficients, respectively. Therefore, as shown in the schematics in Figs. 5.2 (b), (c) and (d), if we apply an electric field on this sample

along the in-plane direction, the $BaTiO_3$ will be polarized along the field direction and the displacement of Ti^{4+} cation along the field direction is accompanied by a tetragonal distortion of the perovskite structure also along the field direction. This distortion induces tensile strain along the same direction. This distortion and tensile strain will be maximized in this structure because there is no clamping effect from the substrate. The induced strain will be transferred to the upper Fe-Ga layer giving rise to alignment of the magnetic domains along the tensile strain direction [Fig 5.2 (d)].

5.2 Magnetic domain structure of Fe-Ga by MFM and LTEM

We performed further characterization of the Fe-Ga magnetic domain structure of a 60 nm thick Fe-Ga patterned by photolithography [see Fig. 5.3 (a)] using magnetic force microscopy (MFM). MFM is more sensitive to the magnetic moments which are oriented along the perpendicular direction to the surface (out-of-plane direction).

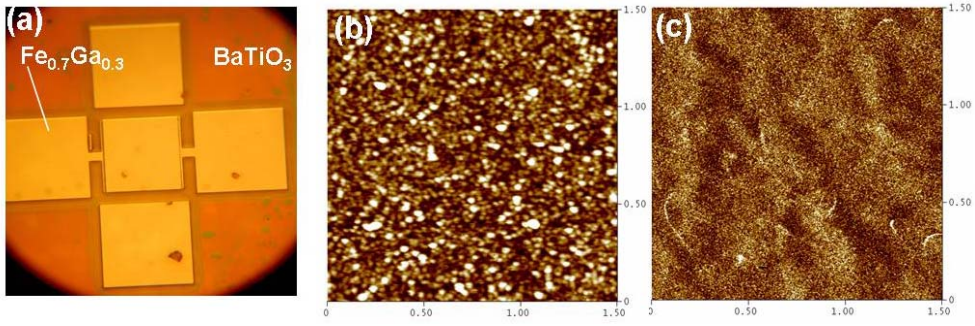

Figure 5.3 (a) Fe-Ga patterned on $BaTiO_3/SrTiO_3$. (b) Height image acquired from 1.5 ×1.5 μm^2 area in the middle pad. The data scale was 0 ~ 5 nm (c) MFM image from the same region. The data scale was 0 ~ 6 degree.

From the AFM height image in Fig. 5.3 (b), the grain size of Fe-Ga film was about 50 nm in diameter, which is in agreement with our TEM analysis from the sample. However, the magnetic domain image in Fig. 5.3 (c) shows very weak intensity indicating that the magnetic domains are preferentially aligned in-plane. We also investigated the magnetic domains which are mostly aligned along the in-plane direction using Lorentz TEM. In LTEM, we can only observe contrast from the magnetic domains which have easy axis in-plane by detecting the Lorentz force on the incident electron beam from the domains. As discussed in section 2.2.2, there are two different techniques for magnetic domain imaging in Lorenz TEM. One is Fresnel imaging and the other is Foucault imaging.

Fresnel image of polycrystalline Fe-Ga thin film

In the Fresnel imaging mode, by changing the defocusing value in the TEM, the domain boundaries can have more or less electrons, which give rise to bright or dark contrast of the domain boundaries, respectively. As shown in Fig. 5.4, clear contrast from the magnetic domains in Fe-Ga was observed using Fresnel imaging. From the in-focus image, we cannot see contrast from the magnetic domain walls, but by changing the defocusing value, bright and dark lines appear at the domain boundaries. The contrast from the domain boundaries changes from dark to bright and bright to dark by changing the focal length from under to over focus. From the magnified domain image and phase map reconstructed by transport of intensity equation,[116] we see 180 degree domain walls, cross-tie walls, and magnetization ripple in the polycrystalline Fe-Ga.

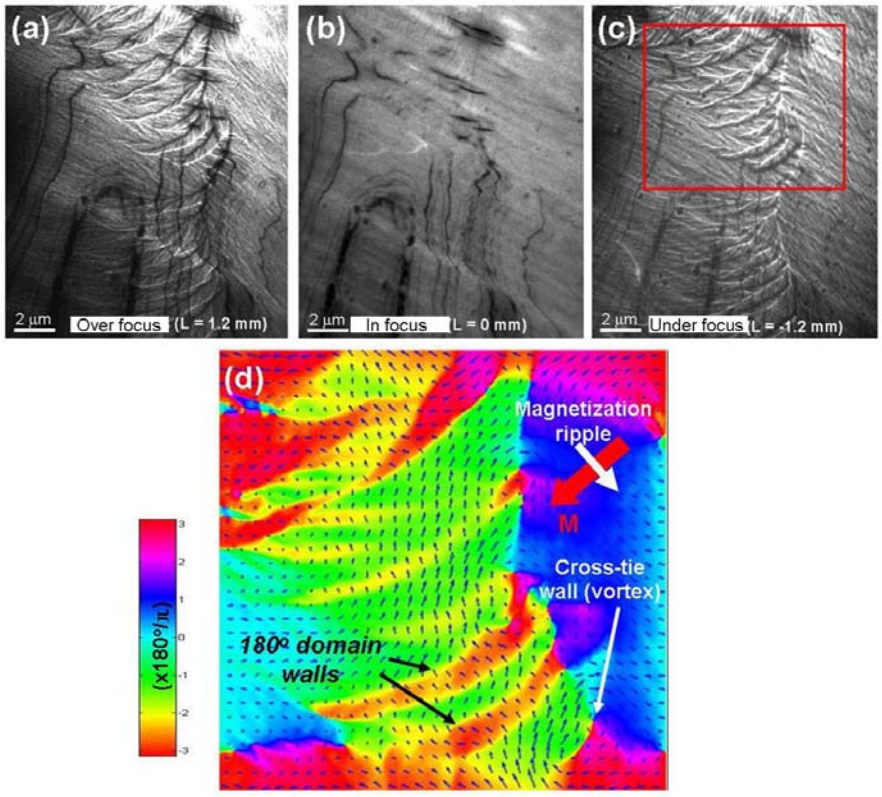

Figure 5.4. Fresnel images of Fe-Ga thin film obtained at various defocusing values of (a) over focus (+ 1.2 mm), (b) in focus (zero), and (c) under focus (– 1.2 mm). (d) Phase map from the area marked in (c) reconstructed by transport of intensity equation (TIE).[116]

Foucalt image of polycrystalline Fe-Ga thin films

We also investigated the magnetic domain structure using Foucalt imaging, as shown in the schematic of Fig 2.2 (b). Using an objective aperture, we can selectively allow one of the four (000) deflected electron beams in the diffraction pattern to form a dark field image of the corresponding magnetic domains. The dark and bright areas in each image in Fig. 5.5 exhibit magnetic domains oriented antiparallel to each other.

By changing the aperture from positive x (or y) position to negative – x (or – y) positions, the contrast of the magnetic domains changes from dark to bright and bright to dark.

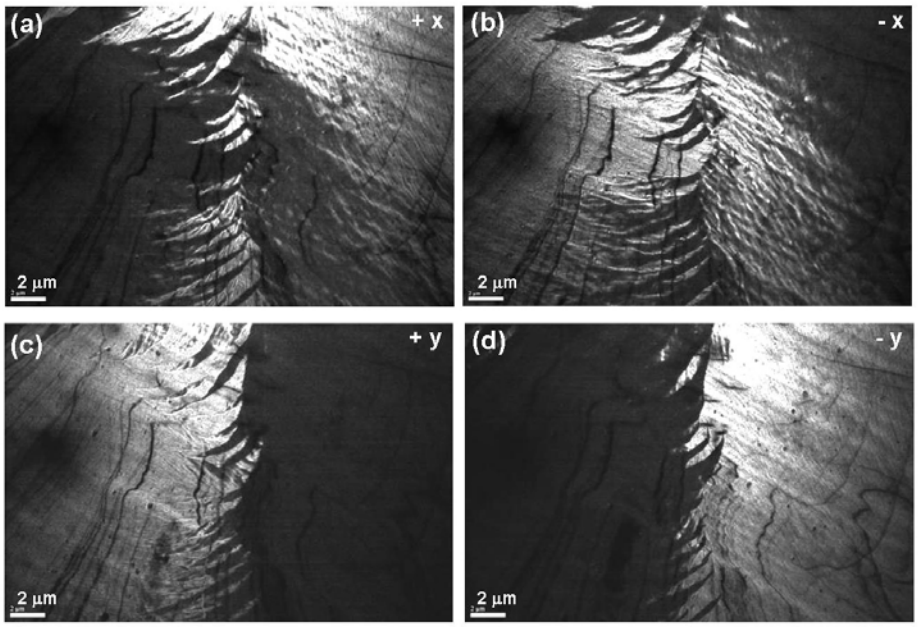

Figure 5.5. Foucalt images of Fe-Ga thin film. By changing the aperture position along x direction [(a) and (b)] and y direction [(c) and (d)], magnetic domains which are oriented along x direction or y direction show as bright and dark areas.

To further understand the magnetization of the domains, a magnetic field was applied along the in-plane direction. In Lorentz TEM, the current through the objective lens was adjusted to control the magnetic field on the sample. This field is perpendicular to the surface of the sample. Therefore, to apply a magnetic field along the in-plane direction of the sample as well as to control the applied field, one can tilt the sample to an arbitrary degree and then control the current through the objective

lens. One can also fix the current and change the tilting angle of the sample. Here, we used the latter method and increased the component of the magnetic field parallel to the film surface by increasing the tilting angle while keeping the current through the objective lens constant.

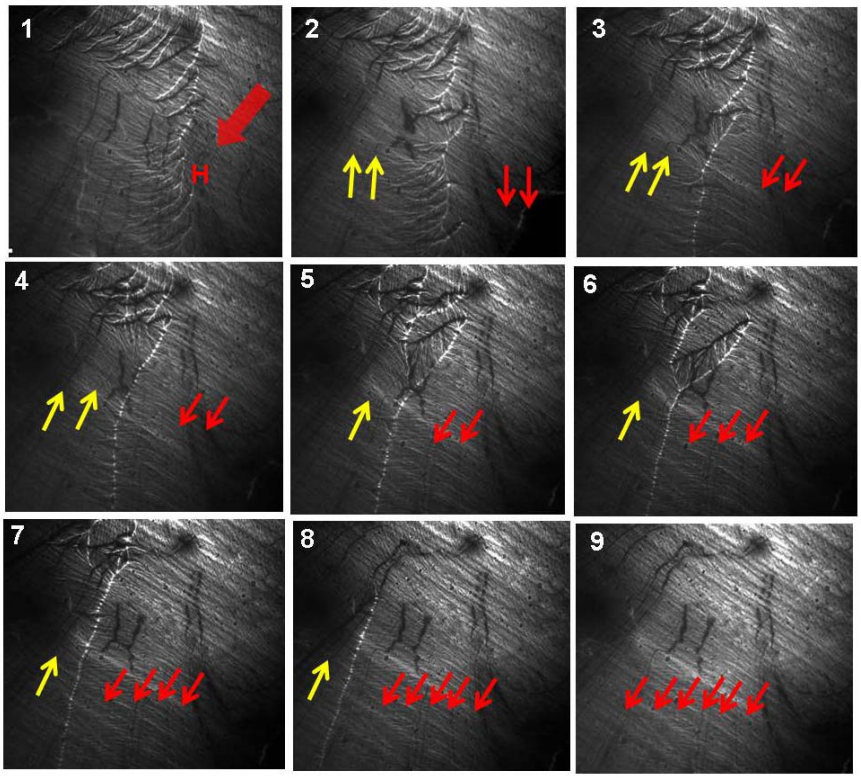

Figure 5.6. Change of magnetic domains in an Fe-Ga thin film under an applied external field. The magnetic field was applied along the in-plane direction (red arrow) and increased by increasing the tilt angle from 0 to 9 degrees. The number from 1 to 9 represents the sequence. The small arrows represent the direction of the magnetic domains

As shown in the Fig. 5.6, the magnetic domain boundaries moved in direction perpendicular to the field direction (towards the left of the image) by increasing the magnetic field component on the sample by tilting the sample from 0 – 9 degrees.

Finally, all magnetic moments were aligned along the field direction and the magnetic domain boundaries disappeared from the field of view. After tilting the sample back to zero, i. e., reducing the in-plane component of the magnetic field, the magnetic domain boundaries formed again (not shown here). Also, by tilting the sample in the opposite direction, the magnetic domains along the opposite direction (yellow arrow in Fig. 5.7) increased and the domain wall moved to the right hand side of the images.

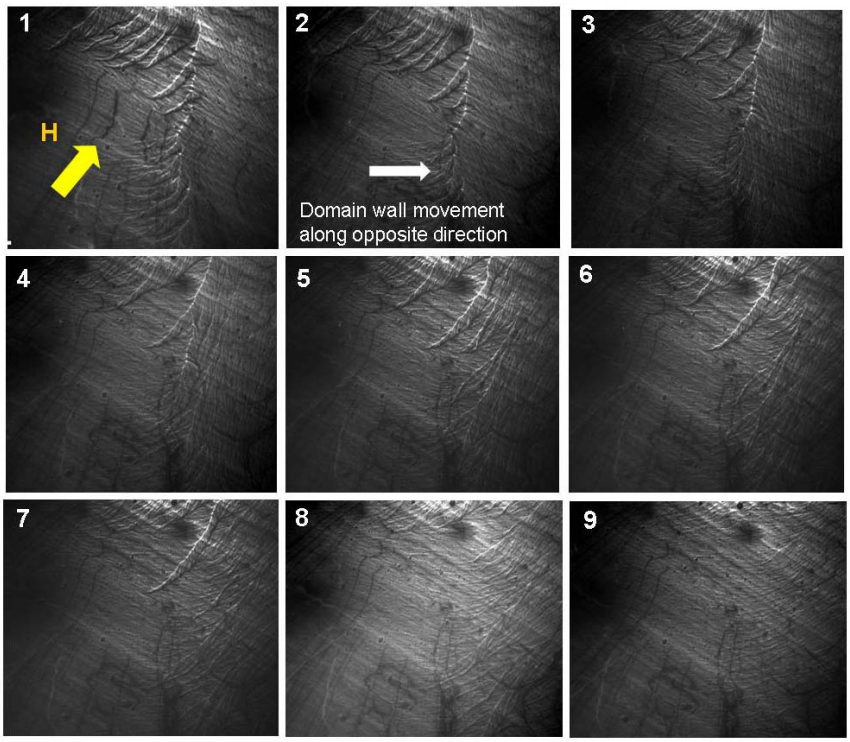

Figure 5.7. Change of magnetic domains in Fe-Ga thin film. The magnetic field (yellow arrow) was applied along opposite direction (compare to Fig. 5. 6) and increased by increasing the tilt angle from 0 – 9 degrees. The number from 1 to 9 represents the sequence.

5.3 TEM sample preparation using electron beam lithography and Focused-Ion Beam (FIB) milling

To apply an electric field on the $BaTiO_3$ layer, the Fe-Ga layer was patterned to form electrodes by photo lithography. Figure 5.8 shows the process for patterning. After cleaning the surface of $BaTiO_3$ using acetone, S1813 photo-resist was spin coated. A spin speed of 4000 rpm was used for 40 seconds for coating, and then the electrode was patterned by exposing it to ultraviolet light for 11 seconds in an MJB-3 mask aligner. After developing the pattern by soaking the sample into the CD 30 solution for 45 seconds, Fe-Ga was deposited by magnetron sputtering. After stripping, to make a gap in the middle of the pad, we spin coated alternating layers of PMMA 950 and PMMA 495 electron beam resists.

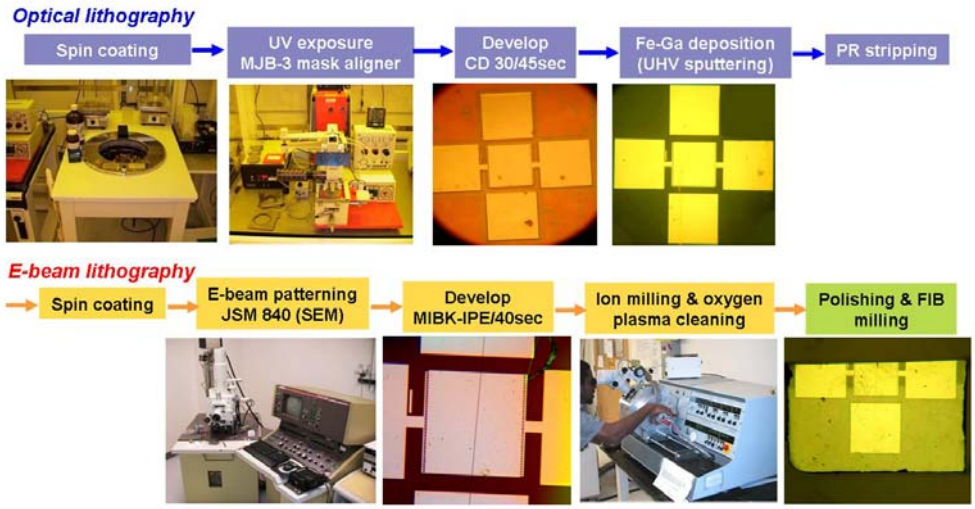

Figure 5.8 Process for deposition of Fe-Ga electrodes. First the electrodes were patterned using photo lithography. After developing the pattern Fe-Ga was deposited by magnetron sputtering at room temperature. Then, electron-beam lithography was used to pattern a gap on the middle Fe-Ga electrode. Finally, the TEM sample was prepared by mechanical polishing and FIB milling.

The multilayer of resist was used to protect the Fe-Ga layer from ion milling. After soft baking, a 1 μm wide gap was patterned using a JEOL JSM 840 scanner. The pattern was developed by soaking the sample in MIBK-IPE for 40 seconds, and then duplicated on the Fe-Ga using ion milling. The ion milling time to remove 60 nm thick Fe-Ga layer was about 210 seconds at 3.5 kV and 1.3 mA. After ion milling, the thickness and magnetic properties of the Fe-Ga layer were measured by AFM and MFM, respectively, and then oxygen plasma cleaning was performed to clean the surface and improve conductivity.

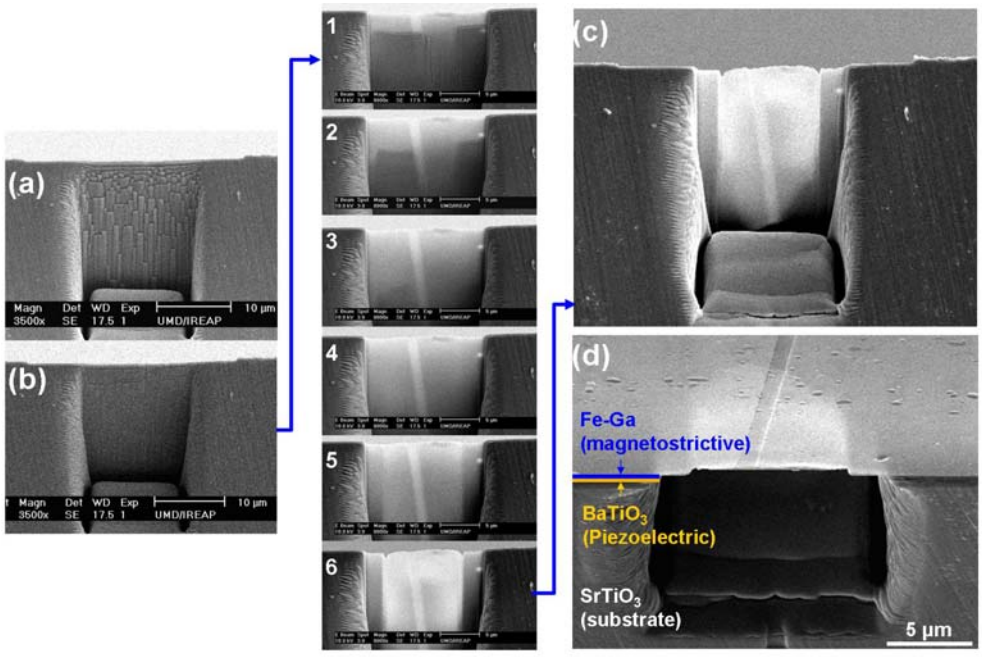

Figure 5.9 SEM images obtained at different stages of FIB milling. (a) after milling using a beam with largest beam current (11500 pA) and (b) second largest current (6600 pA). SEM images number from 1 to 6 show gradual change of contrast by decreasing thickness. (c) and (d) are SEM images from the bottom view and end view, respectively, after milling was completed.

To prepare the TEM samples, mechanical polishing and FIB milling (Dual beam 620, FEI) were used. By mechanical polishing, the size of the sample was reduced to less than 3 mm in diameter, which is the maximum sample size for TEM specimen holder. A slope with an angle of 45 degrees was made on the backside (substrate side) of the sample to avoid blocking the transmitted beam, and then the substrate was milled to form a window region of $15 \times 15 \times 15\ (\mu m)^3$ using focused ion beam with 11500 pA beam current [Figs. 5.9 (a)] and 6600 pA [Fig. 5.9 (b)]. As the $SrTiO_3$ thickness decreased more, we decreased the beam current, in steps of 6600, 2700, 1000, 350 and 157 pA, and the milled facet of $SrTiO_3$ became uniform and flat. The figures numbered 1 to 6 in Fig. 5.9, show the change of contrast due to the decrease of thickness of the $SrTiO_3$ and $BaTiO_3$ layers. After finishing the FIB milling [Fig. 5.9 (c) and (d)], the 1 μm size gap was clearly visible in the window area (15 μm × 10 μm). The $SrTiO_3$ was completely removed from this area and the total thickness of the remaining $BaTiO_3$ and the Fe-Ga was less than 200 nm.

5.4 Switching magnetic domains by applying a magnetic field

The magnetic domain structure of the unconstrained Fe-Ga/$BaTiO_3$ thin film was investigated using a JEOL 2100 LaB_6 TEM. Figures 5.10 (a) and (b) are Fresnel images of magnetic domain boundaries from as-grown sample. By changing the focal length from over ($\Delta F = +4500$ nm) to under focus ($\Delta F = -4500$ nm), the domain boundaries appeared and changed their contrast from dark line to bright line and vice versa. Figures 5.10 (c) and (d) are Foucalt images of the magnetic domains acquired

by placing the aperture along the y axis, which is parallel to the gap (trench) direction in the Fe-Ga layer. By changing the position from + y to – y, the contrast of magnetic domains which are oriented along the ± x direction (perpendicular to the gap) changed. Analysis of the Foucalt images indicates that there coexist 90 ^{o} domains (mainly on the left side of the gap) and 180 ^{o} domains on the right side of the gap which show clear boundaries.

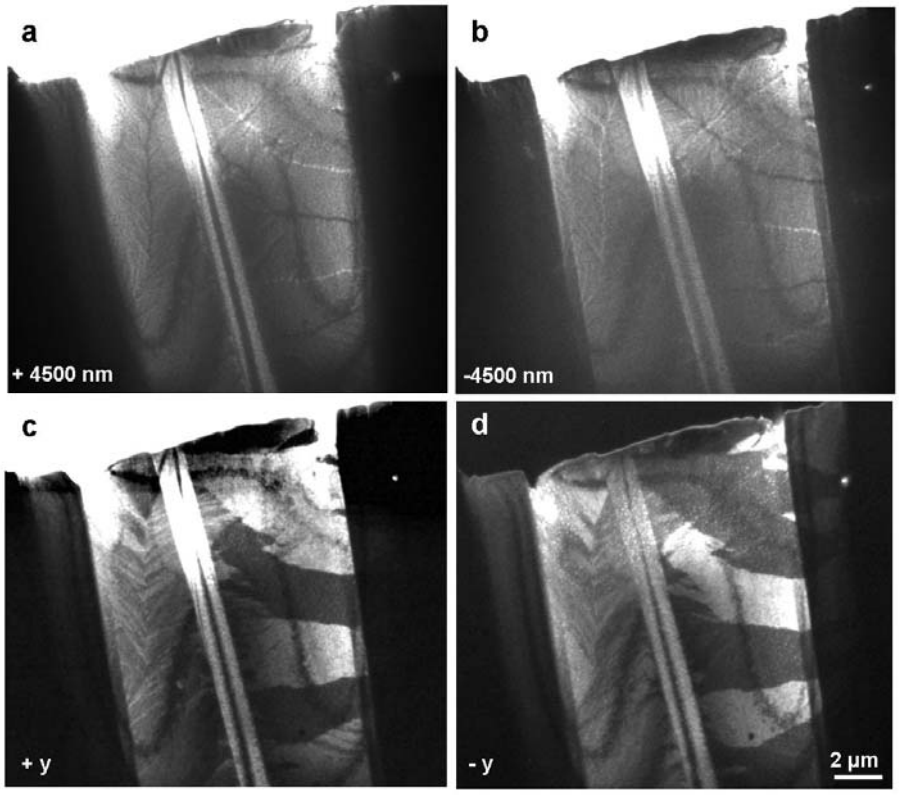

Figure 5.10 Magnetic domain structure of fully unconstrained Fe-Ga/$BaTiO_3$ thin film. Fresnel images obtained at (a) over focus (ΔF = + 4500 nm) and (b) under focus (ΔF= – 4500 nm). (c) and (d) are Foucalt images obtained by moving the aperture along ±y axis.

To further investigate the behavior of the magnetic domain structure of polycrystalline Fe-Ga, a magnetic field was applied in the sample area. To apply a magnetic field, the sample was tilted by + 9 degree, and then the focal length was changed to over focus. The current in the objective lens was increased in steps to increase the magnetic field on the sample and Fresnel images were obtained at every step as indicated in Fig 5.11. In this fashion, the component of the magnetic field along the in-plane direction of the sample was increased.

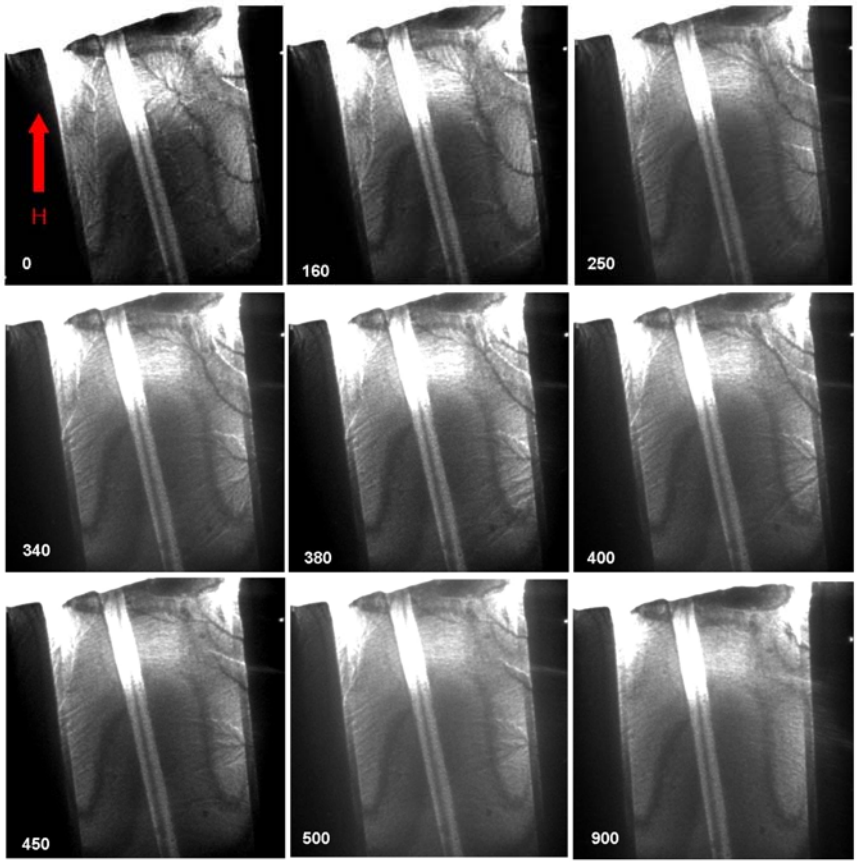

Figure 5.11 Increase of magnetic field component in-plane by tilting the sample to + 9.0 ^{o} and increasing the current though the objective lens (numbers in each figure).

As shown in Figs. 5.11, the magnetic domain boundaries moved in the direction parallel to the magnetic field direction and eventually all domain boundaries disappeared indicating that all magnetic moments were aligned along the direction of the field. After all the magnetic domains were aligned along the field direction, the magnetic field was decreased back to zero, and a multidomain structure of magnetic domains reformed with similar configuration to the initial state (see Fig. 5.12).

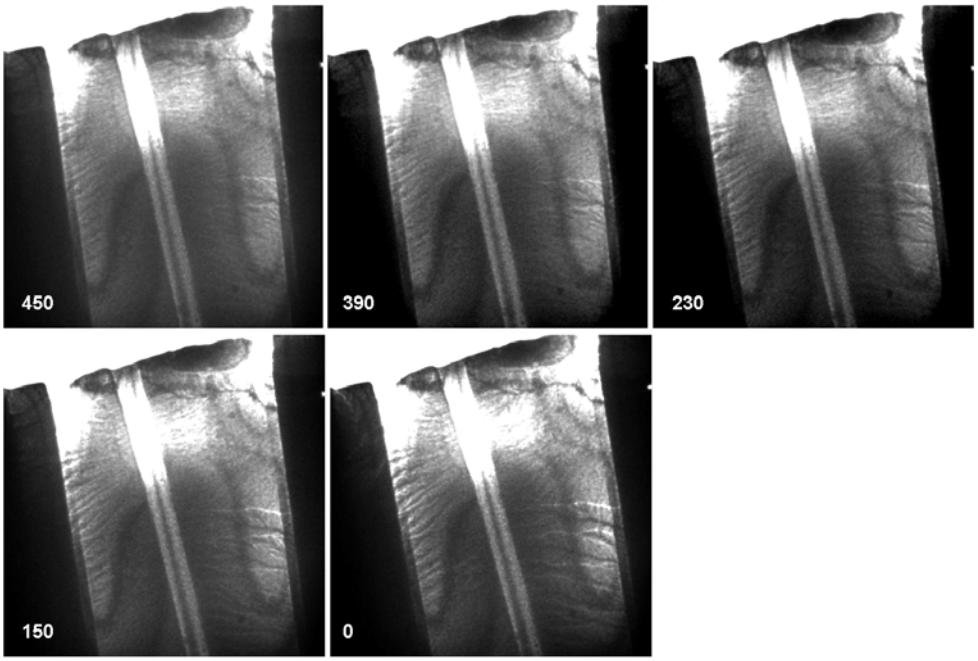

Figure 5.12 Decrease of magnetic field component in-plane by tilting the sample (+ 9.0 ^{o}) and decreasing the current through the objective lens (numbers in each figure).

To ascertain that the effect observed was due to domain wall motion, we applied in-plane magnetic field and observed the change of domain configuration in Foucalt imaging mode. After tilting the sample to zero and applying a magnetic field

along the out-of-plane direction through the objective lens current, we tilted the sample back to 9 degrees to induce an in-plane component of the magnetic field on the sample.

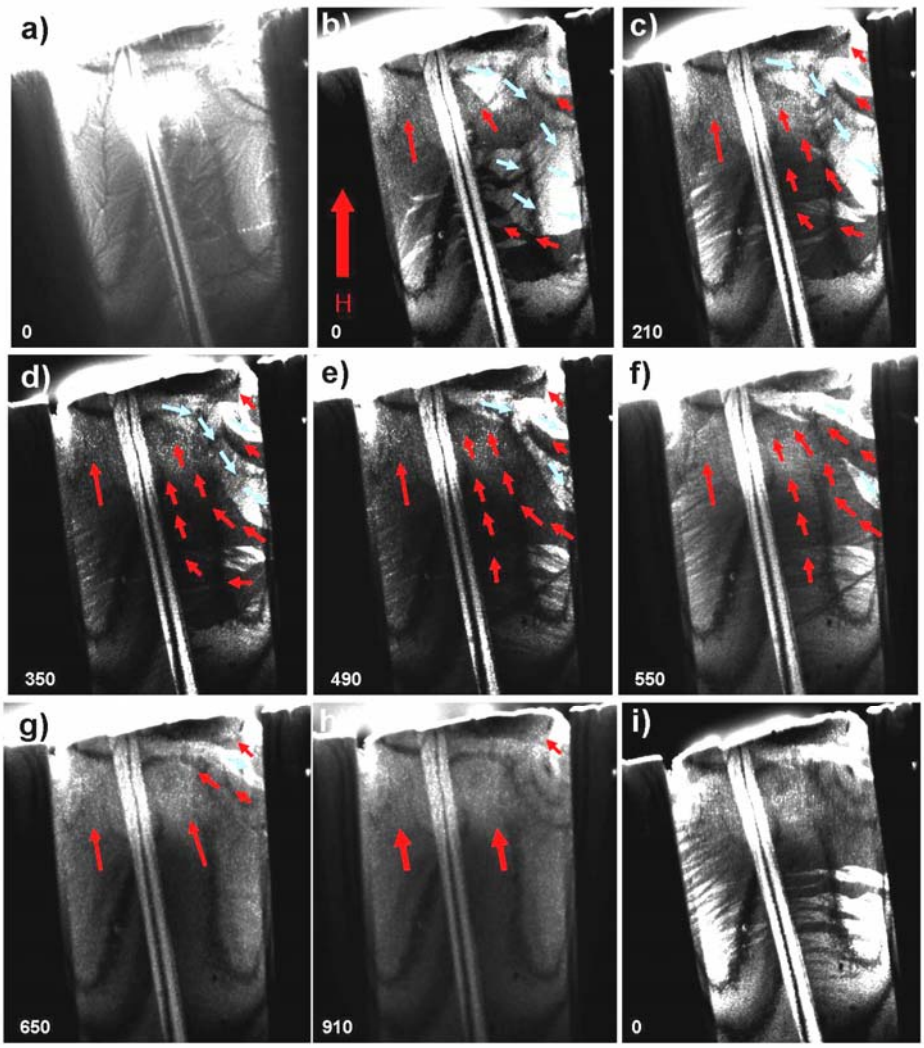

Figure 5.13 Increase and decrease of magnetic field along in-plane by tilting the sample (+ 9.0 ^{o}) and changing the current through the objective lens (numbers in each figure). (a) Fresnel mode at 0 ^{o} tilt. (b) Foucalt mode at 0 ^{o} tilt. (c) – (h) Foucalt images corresponding to an in-plane component of the magnetic domains. (i) The new magnetic domains after reducing the magnetic field back to zero. Red and light blue arrows indicate magnetic domains orientation.

The first two images in Fig. 5.13 represent the initial magnetic domain structure at 0 degree tilt obtained by Fresnel and Foucalt (with objective aperture around + x spot) imaging modes, respectively. By increasing the magnetic field [Figs. 5.13 (c – h)] along the y direction, the magnetic moments gradually switch to the direction of the field and eventually all magnetic domains were aligned along that direction. This observation corroborated the results obtained in Fresnel imaging mode. After reducing the magnetic field back to zero [Fig. 5.13 (i)], a multi domain structure similar to the initial state was obtained. From the relationship between electric current in the objective lens and the in-plane component of the magnetic field calibrated in Table 1, we established the maximum value of the applied in-plane magnetic field to be ~ 196 Oe which is close to the magnetic field required to saturate the magnetization of Fe-Ga thin film (~ 300 Oe).

I (current)	H_{out} (Oe)	H_{in} (Oe)
100	111	21.81244416
200	221	43.62488832
300	332	65.43733248
400	443	87.24977664
500	554	109.0622208
600	664	130.874665
700	775	152.6871091
800	886	174.4995533
900	997	196.3119974
1000	1107	218.1244416

Table 1. Relationship between the current through the objective lens in the LaB_6 TEM and the corresponding out-of-plane and in-plane components (by 9 degree tilting) of the magnetic field on the sample.

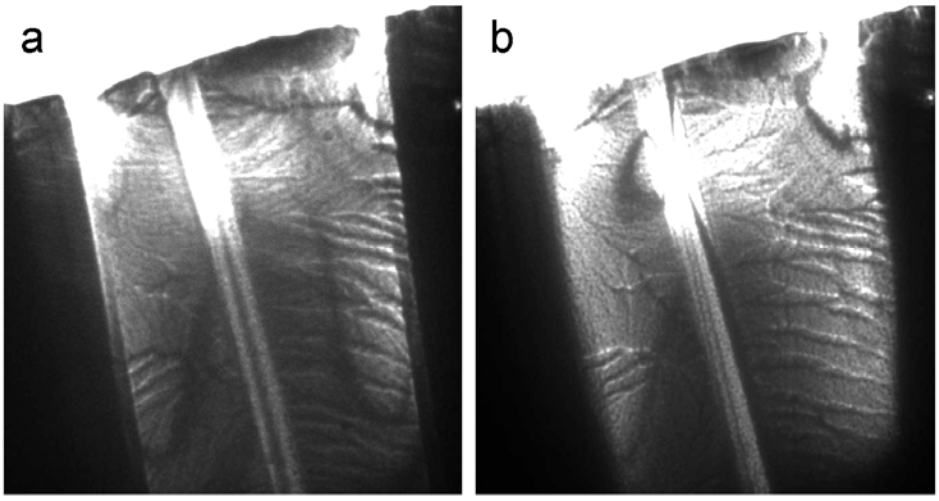

Figure 5.14 Change of tilting angle and focal length from (a) + 9.0 (F = – 6000 nm) to (b) – 9.0 degree (F = + 6000 nm).

Figure 5.14 shows Fresnel images at different tilting angles and focal lengths. To differentiate between the magnetic domain structure and bend contours, the sample was tilted from + 9 [Fig. 5.14 (a)] to – 9 degrees [Fig. 5.14 (b)] in field-free conditions. Tilting the sample did not change the contrast of the magnetic domain walls. However, the bend contours were completely changed. Furthermore, the change of focal length from – 6000 nm [Fig. 5.14 (a)] to + 6000 nm [Fig. 5.14 (b)], clearly distinguished the magnetic domain walls because of the change in contrast from bright to dark and dark to bright from the bend contours which did not change contrast.

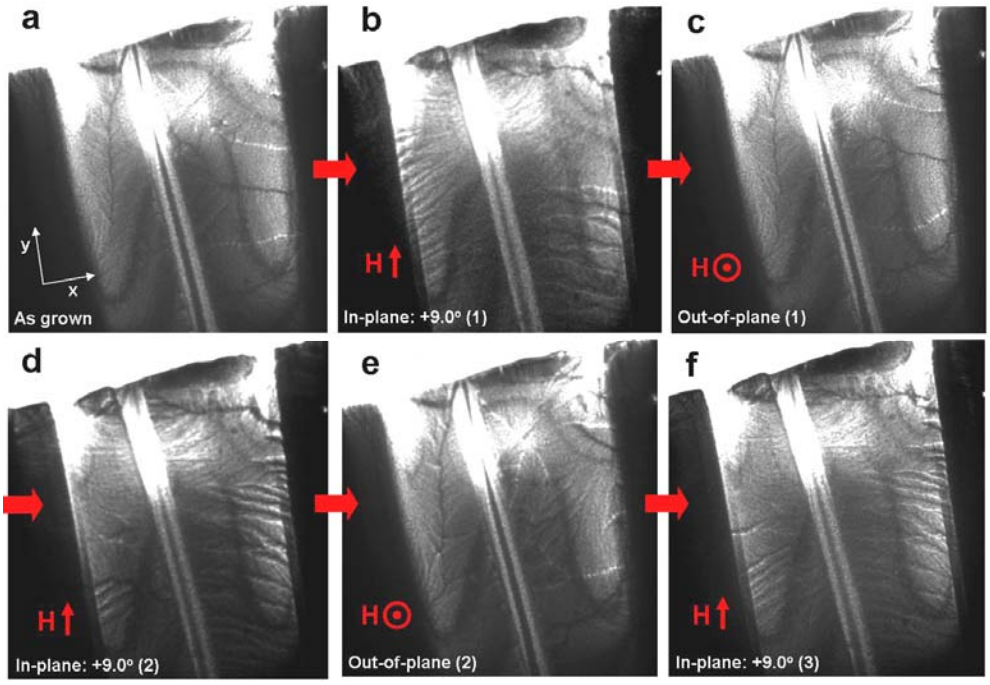

Figure 5.15 Change of magnetic domain structure according to applied magnetic field direction (indicated in the images).

The evaluation of magnetic domain structure with magnetic field direction is shown in Fig. 5.15. A magnetic field was applied along the in-plane direction [Figs. 5.15 (b), (d), and (f)] followed by an out-of-plane [(c) and (e) images in Fig. 5.15] direction of the magnetic field alternately to see the change of magnetic domain configuration with field direction. After removing the magnetic field, some magnetic moments switched back to the original direction (x-direction) and formed new domains which are aligned along the x-direction as shown in Fig. 5.15 (b), (d), and (f). This preferred orientation of the domains is related to the misfit strain relaxation of the unconstrained $BaTiO_3$ and clamping at the edges of the FIB prepared window

region. These complex interactions cause the asymmetric shape of $BaTiO_3$, i.e., elongation of $BaTiO_3$ along the x direction in the edge region and result in non-uniform strain distribution and the bend contour. We also applied a magnetic field along the direction perpendicular to the surface and then removed the field. As shown in Fig. 5.15 (c) and (e), the magnetic domains under this condition were similar to the as grown state. The bend contours also showed similar configuration before and after the application of the magnetic field.

5.5 Switching magnetic domains by applying an electric field (ME effect)

In order to investigate if we could observed the strain-mediated ME effect between $BaTiO_3$ and Fe-Ga, we analyzed the magnetic domain configuration under an applied electric field. For this purpose, we first applied a magnetic field in the y-direction (along the gap) perpendicular to the direction that the electric field would be applied next (x-direction). This configuration should give preferred orientation of the magnetic domains along the y-direction. Once the electric field is applied, we expect to see more domain re-orientation along the x-direction (the electric field direction).

After bringing the magnetic field back to zero, we increased the electric field from zero [Fig. 5.16 (a)] to 10 V [5.16 (c)], and we observed changes in the magnetic domains which had been pre-aligned along the y-axis (in-plane component of the magnetic field). The magnetic domain structure created by the H-field along the y-direction is less stable than the magnetic domain structure created by applying an out-

of-plane magnetic field. By applying an electric field, a tensile strain is induced in the $BaTiO_3$ thin layer along the x-direction. This tensile strain is transferred to the Fe-Ga layer and results in a change of the magnetic domains from the y-direction to the x-direction. During the application of voltage, there was no change in the magnetic domain configuration of the Fe-Ga layer until the voltage was raised to 7.5 volts [Fig. 5.16 (b)]. At this point, there was a sudden increase in volume of the domains with magnetic moment along the x-axis. With continued increase in voltage to 10 volts, there was another sudden change in the magnetic domain structure [Fig. 5.16 (c)]. These results indicate that there is a resistance of the domains to switch and only when enough strain energy has built up, the domains suddenly grow. The magnetic domains changed at an applied voltage of 7.5 V [Fig. 5.16 (b)] and 10 V [Fig. 5.16 (c)]. The leakage current versus applied voltage during this observation was measured and is shown in Fig. 5.16 (d). This curve shows a slight reduction in current at 7.5 and 10 volts when the domain boundaries moved. At a higher voltage of 11 volts the leakage current density increased dramatically and the sample experienced an irreversible break down.

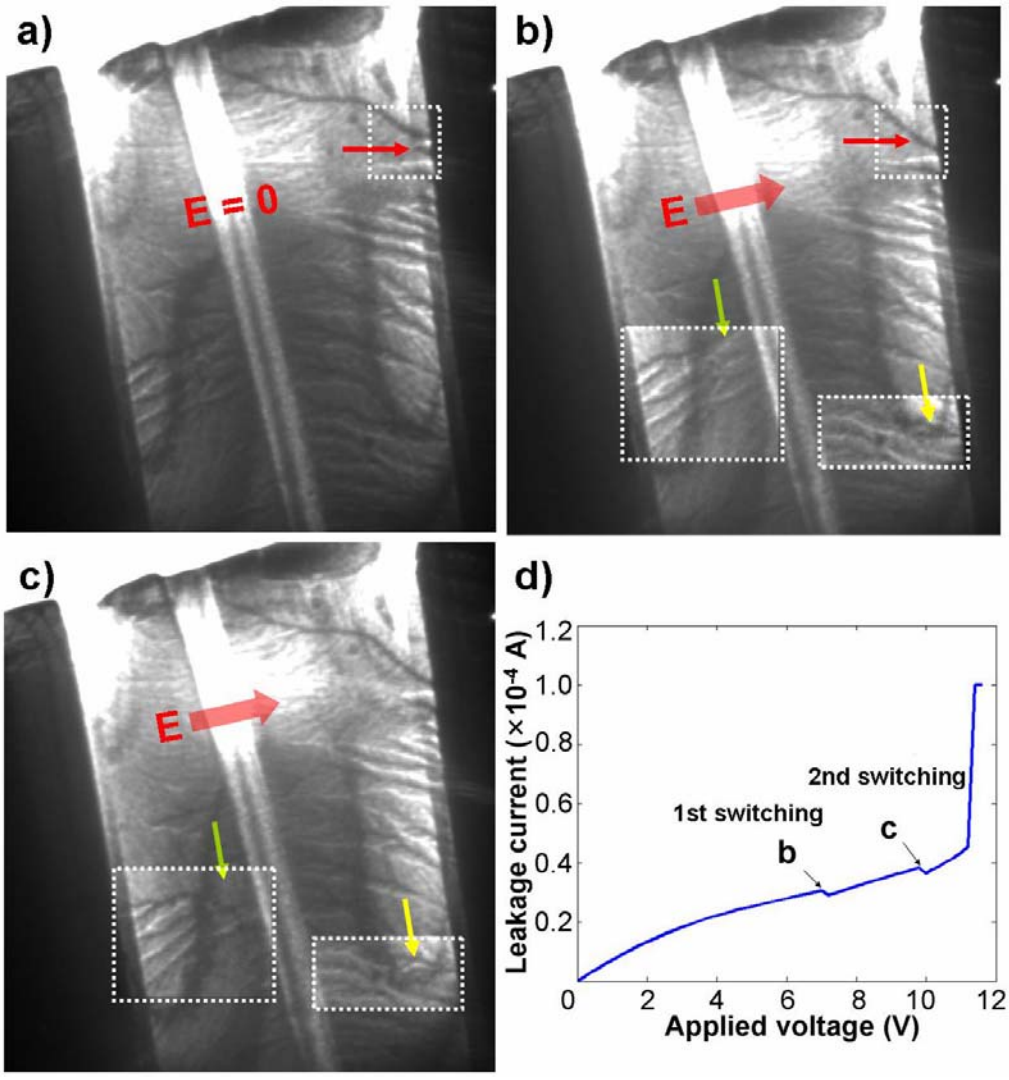

Figure 5.16 Switching of magnetic domains by the application of an electric field. (a) E = 0 V, (b) E = 7.5 V, and (c) E = 10 V. (d) Acquired leakage current versus applied electric field (voltage). The arrows indicate the changed regions.

The volume of the domains with magnetic moment along the x-axis was increased after applying an electric field. As shown in Fig. 5.17, the newly formed

domains (red-colored region) after removing the magnetic field (y-direction) are mainly oriented along x-direction. After applying an electric field and induce the strain along the x-direction, these domains merged and increased in volume (blue-colored region) by switching the magnetic moment of neighboring domains from the y-direction to the x-direction

Therefore, our results show dynamic observation in Lorentz TEM of strain-mediated magnetoelectric effect by the application of an electric field on the sample.

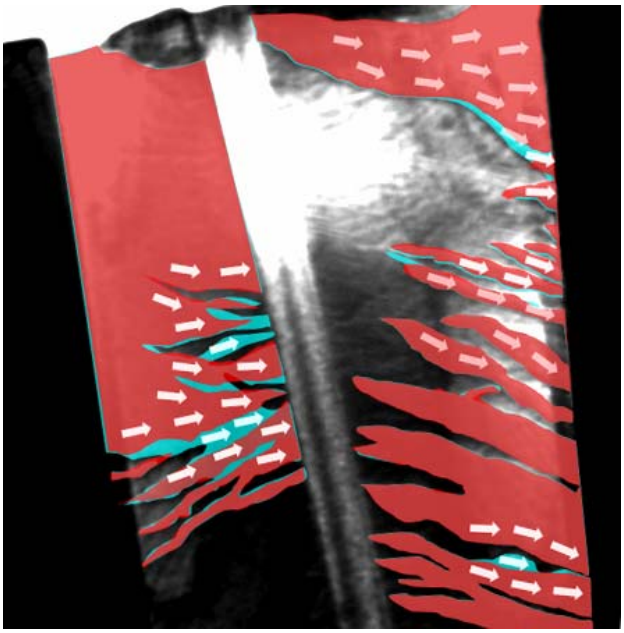

Figure 5.17 Comparison of the magnetic domains before and after applying an electric field. Red-colored region represents the magnetic domains with magnetization along x before applying an electric field (E = 0 V) and the blue-colored region represents the increased area of magnetic domains after applying an electric field (E = 10 V). The arrows indicate magnetic domains orientations.

Chapter 6

6. Summary and future work

In this thesis, the ferroelectric and ferromagnetic properties in multiferroic $BiFeO_3$ thin films were investigated. The heteroepitaxial constraint created in a film structure by the substrate and the volatile nature of bismuth cause complicated changes to the microstructure and physical properties of $BiFeO_3$ films. Secondary phases, such as, α-Fe_2O_3, γ-Fe_2O_3, and Fe_3O_4 formed spontaneously in the films grown at either relatively high growth temperature or low oxygen pressure. The formation of ferromagnetic γ-Fe_2O_3 and Fe_3O_4 significantly increased the saturation magnetization of the films. To enhance the ferromagnetism of columnar structure of the sample with $BiFeO_3$-Fe_2O_3 thin films, a phase transformation from antiferromagnetic α-Fe_2O_3 to ferromagnetic γ-Fe_2O_3 was induced by annealing under a hydrogen atmosphere followed by annealing in oxygen atmosphere.

The ferroelectricity of $BiFeO_3$ was studied in films with columnar structure of $BiFeO_3$-Fe_2O_3 as well as films with polycrystalline $BiFeO_3$. Both of them showed larger electrical polarization as well as less or no misfit strain compared to single crystalline epitaxial films with single $BiFeO_3$ phase. From our results, the observed increased polarization in thin film structures probably originated from an intrinsic property of $BiFeO_3$ single crystal rather than the misfit strain and/or tetragonal distortion in heteroepitaxial thin film.

To further understand the origin of the ferroelectric properties and enhanced switching of ferroelectric domains in columnar structure of $BiFeO_3$-Fe_2O_3 films, the

relative concentrations of Fe^{2+}, Fe^{3+} and O^{2-} have to be measured by EELS across the two phases to obtain any compositional variations that might exist among the two phases. Also, convergent beam electron diffraction (CBED) is required to investigate the strain distribution and difference in strain relaxation near the interfacial area and center of $BiFeO_3$ columns.

In an effort to enhance the structural, magnetic, and electrical properties of the $BiFeO_3$ films, we investigated various ways for improving the crystallinity of the films using a new technique called flux-mediate epitaxy (FME), and achieved single crystal-like thin films with large grains, smooth surfaces and without impurity phases.. Compared to PLD grown films FME films showed improved dielectric properties (higher dielectric constant and lower leakage current).

The present studies also include the possible applications of magnetoelectric coupling effects, in noble spintronic devices in which magnetoresistance and exchange bias are controlled by ME effects. We investigated this effect using a Co/Pt multilayer on Cr_2O_3 thin films. We achieved an extremely smooth interface between Co/Pt and the Cr_2O_3 layer (RMS ~ 0.3 nm) to reduce unexpected effects from roughness, and more importantly, enhanced resistance of the Cr_2O_3 film. We were able to apply sufficiently high electric field 150 times higher than the applied field on earlier single crystal experiments. Despite our high quality sample and the high field, the thin film device exhibited no significant ME effect on exchange bias in the sensitivity range of our equipment. However, in this work, we showed an efficient way for controlling the exchange bias field and its sign by sweeping the magnetic field with an offset during cooling. We controlled the sign of the exchange bias and

the shape of the hysteresis loops, i.e., single/dual hysteresis loops of the out-of-plane magnetized Co/Pt layers by sweeping a magnetic field with various offsets during magnetic field cooling.

In addition, we demonstrated for the first time the dynamic observation of strain-mediated ME coupling effect using ferromagnetic Fe-Ga and ferroelectric $BaTiO_3$ bilayer thin film structure. The reversible switching of magnetic domains in the ferromagnetic layer was observed using in-situ Lorenz TEM while increasing an applied electric field and inducing strain on the ferroelectric layer. This is the first direct observation of strain-mediated ME coupling, especially, control of magnetic domains by strain induced from an electric field. We observed direct evidence for strain-mediate ME coupling from the strain propagation and reversible switching of magnetic domains by an applied electric field in Lorenz TEM.

A more detailed analysis of the Lorentz TEM images should be carried out to obtain an estimate for α, the magnetoelectric coupling, and to estimate the amount of strain on the sample after the application of the electric field. We should also be able to estimate the domain wall energy by estimating the work necessary to move it. Also, additional attempts can be challenging, for example, the shape dependence on switching of Fe-Ga magnetic single domains or the control of magnetic domains by applying an electric field along two different orientations. For the shape dependence, electrodes with circular, oval and square shape could be compared.

References

1 W. Eerenstein, N. D. Mathur, and J. F. Scott, Nature **442,** 759 (2006).
2 P. Weiss, J. Phys. **6**, 661 (1907).
3 E. C. Stoner, Philos. Mag. **15**, 1080 (1933).
4 G. A. Smolenskii and I. E. Chupis, Sov. Phys. Usp. **25**, 475 (1962).
5 S. Alexander and S. Shtrikman, Solid State Commun. **4**, 115 (1966).
6 E. Fischer, G. Gorodetsky and R. M. Hornreich, Solid State Commun. **10**, 1127 (1972).
7 Hill, N. A., J. Phys. Chem. B **104,** 6694 (2000).
8 N. Hur, S. Park, P. A. Sharma, J. S. Ahn, S. Guha and S. -W. Cheong, Nature **429**, 392 (2004).
9 Ryu, J., Vásquez Carazo, A., Uchino, K.& Kim, H. –E. Jpn. J. Appl. Phys. **40**, 4948 (2001).
10 S. X. Dong, J. F. Li, and D. Vieland, Appl. Phys. Lett. 83, 2265 (2003.)
11 V. J. Folen, G. T. Rado and E. W. Stalder, Phys. Rev. Lett. **6**, 607 (1961).
12 G. T. Rado and V. J. Folen, Phys. Rev. Lett. **7**, 310 (1961).
13 E. Ascher, H. Rieder, H. Schimid, and H. Stössel, J. Appl. Phys. **37**, 1404 (1966).
14 F. Bertaut, F. forrat, and P. Fang, C. R. Acad. Sci. **256**, 1958 (1963).
15 V. A. Bokov, G. A. Smolenskiĭ, S. A. Kizhaev, and I. E. MyI'nikova, Sov. Phys. Solid State **5**, 2646 (1964).
16 I. G. Ismailzade and S. A. Kizhaev, Sov. Phys. Solid State **7**, 236 (1965).
17 J. Chappert, Phys. Lett. **18**, 229 (1965).
18 M. Eibschütz and H. J. Guggenheim, Solid State Commun. **6**, 737 (1968).
19 L. Holmes, M. Eibshütz, and H. J. Guggenheim, ibid. **7**, 973 (1969).
20 J. Wang, J. B. Neaton, H. Zheng, V. Nagarajan, S. B. Ogale, B. Liu, D. Viehland, V. Vaithyanathan, D. G. Schlom, U. V. Waghmare, N. A. Spaldin, K. M. Rabe, M. Wuttig, R. Ramesh, Science **299**, 1719 (2003).
21 K.Y. Yun, M. Noda, M. Okuyama, H. Seki, H. Tabata and K. Saito, J. Appl. Phys. **96**, 3399 (2004).
22 Yu. F. Popov, A. M. Kadomtseva, G. P. Vorobev, A. K. Zvezdin, Ferroelectrics, **162**, 135 (1994).
23 J. R. Teague, R. Gerson, W. J. James, Solid State Commun. **8**, 1073 (1970)
24 V. A. Murashav, D. N. Rakov, V. M. Ionov, I. S. Dubenko, Y. U. Titov, Ferroelectrics, **162**, 11 (1994).
25 Van Run, A. M. J. G., Terrell, D. R., and Scholing, J. H., J. Mater. Sci. **9**, 1710 (1974).
26 Nan, C. –W, et al. Appl. Phys. Lett. **81**, 3831 (2002).
27 Cai, N., Nan, C. –W, Zhai, J. and Lin, Y. Appl. Phys. Lett. **84**, 3516 (2004).
28 Srinvasan, G. et al. Phys. Rev. B **65**, 134402 (2002).
29 Lee, M. K. et al. Appl. Phys. Lett. **77,** 3547 (2000).
30 J. Van Suchtelen, Philips Res. Rep. **27**, 28 (1972).
31 J. Van Den Boomgaard, D. R. Terrelll, R. A. J. Born, and H. F. J. I. Giller, J. Mater. Sci. **9**, 1705 (1974).

32 A. Hanumaiah, T. Bhimasankaram, S. V. Suryanaryana, and G. S. Kumar, Bull. Mater. Sci. **17**, 405 (1994).
33 J. Van Den Boomgaard, A. M. J. G. Van Run, and J. Van Suchtelen, Ferroelctrics **14**, 727 (1976).
34 W. E. Kramer, R. H. Hopkins, and M. R. Danel, J. Mater. Sci. Lett. **12**, 409 (1977).
35 G. Harshe, J. P. Dougherty, and R. E. Newnham, Int. J. Appl. Electromagn. Mater. **4**, 145 (1993).
36 M. Avellaneda and G. Harshe, J. Intell. Mater. Syst. Struct. **5**, 501 (1994).
37 D. N. Astrov, Sov. Phys. JETP **11**, 708–709 (1960).
38 G. A. Smolenskiĭ and I. E. Chupis, Sov. Phys. Usp. **25**, 475 (1982).
39 G. A. Smolenskiĭ, Fizika Tverdogo Tela **4**, 1095 (1962).
40 D. N. Astrov, Sov. Phys. JEPT **13**, 729 (1961).
41 J. R. Hattrick-Simpers, L. Dai, M. Wuttig, I. Takeuchi, and E. Quandt, Rev. Sci. Instrum. **78** 106103 (2007)
42 W. Eerenstein M. Wiora, J. L. Prieto, J. F. Scott, and N. D. Mathur, Nature. Mat. **6**, 348-351 (2007).
43 P. Grünberg, . R. Schreiber, Y. Pang, M. B. Brodsky, and H. Sowers, Phys. Rev. Lett. **57** 2442 (1986).
44 M. N. Baibich, J. M. Broto, A. Fert, F. Nguyen Van Dau, F. Petroff, P. Eitenne, G. Creuzet, A. Friederich, and J. Chazelas Phys. Rev. Lett. **61** 2472 (1988).
45 M. N. Baibich *et al.* Phys. Rev. B **39** 4828 (1989).
46 J. S. Moodera, Lisa R. Kinder, Terrilyn M. Wong, and R. Meservey, Phys. Rev. Lett. **74** 3273 (1995).
47 G.A. Prinz, Science **282,** 1660 (1998).
48 J. Grollier, V. Cros, A. Hamzic, J. M. George, H. Jaffrès, A. Fert, G. Faini, J. Ben Youssef, and H. Legall, Appl. Phys. Lett. **78** 3663 (2001).
49 S. Urazhdin, Norman O. Birge, W. P. Pratt, Jr., and J. Bass, Appl. Phys. Lett. **84**, 1516 (2004).
50 Ch Binek and B Doudin, Magnetoelectrics with magnetoelectrics. J. Phys.: Condens. Matter **17** (2005) L39.
51 H. Béa, M Bibes, A. Barthélémy, K. Bouzehouane, E. Jacquet, A. Khodan, J.-P. Contour, S. Wyczisk, A. Forget, D. Lebeugle, D. Colson and M. Viert, Appl. Phys. Lett**. 87**, 072508 (2005).
52 M. Murakami, S. Fujino, S.-H. Lim, L. G. Salamanca-Riba, M. Wuttig, I. Takeuchi, H. Sugaya, T. Hasegawa and S. E. Lodland, Appl. Phys. Lett. **88**, 112505 (2006).
53 Y. –Y. Li Phys. Rev. **101**, 1450 (1956).
54 A. J. Koch, J. J. Becker, A. E. Berkowitz, W. J. Schuele and P. J. Flanders, J. Appl. Phys. **39**, 1261 (1968).
55 Y. –H. Chu, Q. Zhan, et al. Adv. Mater. **18**, 2307 (2006).
56 D. Lebeugle, D. Colson, A. Forget, and M. Viret, Appl. Phys. Letts. **91** 022907 (2007).
57 K.Y. Yun, M. Noda, M. Okuyama, H. Seki, H. Tabata and K. Saito, J. Appl. Phys. **96**, 3399 (2004).

58 J. R. Teague, R. Gerson, W. J. James, Solid State Commun. **8,** 1073 (1970).
59 Yu. F. Popov, A. M. Kadomtseva, G. P. Vorobev, A. K. Zvezdin, Ferroelectrics **162**, 135 (1994).
60 V. A. Murashav, D. N. Rakov, V. M. Ionov, I. S. Dubenko, Y. U. Titov, Ferroelectrics, **162**, 11 (1994).
61 J. Li, J. Wang, M. Wuttig, R. Ramesh, N. Wang, B. Ruette, A. P. Pyatakov, A. K. Zvezdin, D. Viehland Appl. Phys. Lett. **84**, 255261 (2004).
62 M. Murakami, S. Fujino, S.-H. Lim, B. Varughese, H. Sugaya, T. Hasegawa, S.E. Lofland, L. G. Salamanca-Riba, M. Wuttig, I. Takeuchi, Appl. Phys. Lett. **88**, 112505 (2006).
63 S. H. Lim, M. Murakami, W. L. Sarney, S. Q. Ren, A. Varatharajan, V. Nagarajan , S. Fujino, M. Wuttig, I. Takeuchi, L. Salamanca-Riba, Adv. Funct. Mater. **17**, 2594 (2007).
64 H. Béa, M. Bibes, A. Barthélémy, K. Bouzehouane, E. Jacquet, A. Khodan, J. -P. Contour, S. Fusil, F. Wyczisk, A. Forget, D. Lebeugle, D. Colson, M. Viret, Appl. Phys. Lett. **87**, 072508 (2005).
65 W. Eerenstein, F. D. Morrison, J. Dho, M. G. Blamire, J. F. Scott and N. D. Mathur, Science **307**, 1203a (2005).
66 C. Ederer and N. A. Spaldin, Phys. Rev. B **71**, 060401 (2005).
67 B. J. Kim, E. T. Lee and G. E. Jang, Thin Solid films **341**, 79 (1999).
68 J. W. Matthews and W. A. Jesser, Acta Metall. **15**, 595 (1967).
69 J. W. Matthews, A. E. Blakeslee and S. Mader, Thin Solid Films **33**, 253 (1976).
70 G. A. Smolenskii and I. E. Chupis, Sov. Phys. Usp. **25**, 475 (1982).
71 W. Eerenstein, N. D. Mathur, and J. F. Scott, Nature **442,** 759 (2006).
72 Ch Binek and B. Doudin, J. Phys.: Condens. Matter **17**, L39 (2005).
73 J. Dho, X. Qi, H. Kim, J. L. MacManus-Driscoll, and Mark G. Blamire Adv. Mater. **18,** 1445 (2006).
74 J. F. Scott, Science **315**, 954 (2007).
75 N. Hur, S. Park, P. A. Sharma, J. S. Ahn, S. Guha and S.-W. Cheong, Nature (London) **429**, 392 (2004).
76 M. Murakani, S. Fujino, S. -H. Lim, B. Varughese, H. Sugaya, T. Hasegawa, S.E. Lofland, L. G. Salamanca-Riba, M. Wuttig, and I. Takeuchi, Appl. Phys. Lett. **88**, 112505 (2006).
77 H. Béa, M. Bibes, A. Barthélémy, K. Bouzehouane, E. Jacquet, A.Khodan, J.-P. Contour, S. Wyczisk, A. Forget, D. Lebeugle, D. Colson, and M. Viert, Appl. Phys. Lett. **87**, 072508 (2005).
78 S. H. Lim, M. Murakami, W. L. Sarney, S. Q. Ren, A. Varatharajan, V. Nagarajan, S. Fujino, M. Wuttig, I. Takeuchi, L. Salamanca-Riba, Adv. Funct. Mater. **17** 2594 (2007).
79 D. Lebeugle, D. Colson, A. Forget, and M. Viret Appl. Phys. Lett. **91** 022907 (2007).
80 Ederer and N. A. Spaldin, Phys. Rev. B **71**, 060401 (2005).
81 X. Qi, J. Dho, M. Blamire, Q. Jia, J. S. Lee, S. Foltyn, J. L. MacManus-Driscoll, J. Magnetism and Magnetic Materials, **283** 415 (2004).

82 K. Y. Yun, D. Ricinschi, T. Kanashima, M. Okuyama, Appl. Phys. Lett. **89** 192902 (2006).
83 J. Dho, X. Qi, H. Kim, J. L. MacManus-Driscoll, and Mark G. Blamire Adv. Mater. **18** 1445 (2006.)
84 J. F. Scott *et al*., Science **246**, (1989).
85 H. Park, J. Jung, D. Min, S. Kim, and S. Hong, Appli. Phys. Lett. **84** 1734 (2004).
86 Y. Kim, Y. Cho, S. Hong, S. Bühlmann, H. Park, D. –K. Min, S. –H. Kim, and K. No, Appl. Phys. Letts. **89**, 162907 (2006).
87 J. Y. Li, R. C. Rogan, E. Ustundag and K. Bhattacharya, Nature Mat. **4**, 776 (2005)
88 H. F. Kay and J. W. Dunn, Philo. Mag. **7,** 2027 (1962).
89 S. B. Ren, C. J. Lu, J. S. Liu, H. M. Shen, and Y. N. Wang, Phys. Rev. B. **54** 14337 (1996).
90 T. Zhao, A. Scholl, F. Zavaliche, K. Lee, M. Barry, A. Doran, M. P. Cruz, Y. H. Chu, C. Ederer, N. A. Spaldin, R. R. Das, D. M. Kim, S. H. Baek, C. B. Eom, and R. Ramesh, Nature Mat. **5**, 823 (2006)
91 R. Kretshmer and K. Binder, Phys. Rev. B **20**, 1065 (1979.)
92 P. Wurfel, I. P. Batra, and J. T. Jacobs, Phys. Rev. Lett. **30**, 1218 (1973).
93 A. Gruverman, A. Kholkin, A. Kingon, and H. Tokumoto, Appl. Phys. Lett. **78**, 2751 (2001).
94 A. Gruverman, Appl. Phys. Lett. **75**, 1452 (1999).
95 R. Takahashi, Y. Yonezawa, M. Ohtani, M. Kawasaki, K. Nakajima, T. Chikyow, H. Koinuma, and Y. Matsumoto, Adv. Funct. Mater. **16**, 485 (2006)
96 R.Takahashi, Y. Matsumoto, T. Kohno, M. Kawasaki, H. Koinuma, J. Cryst. Growth **262**, 308 (2004).
97 R. Takahashi, Y. Yonezawa, M. Ohtani, M. Kawasaki, Y. Matsumoto, H. Koinuma, Appl. Surf. Sci. **252**, 2477 (2006).
98 R. Takahashi, Y. Tsuruta, Y. Yonezawa, T. Ohsawa, H. Koinuma, and Y. Matsumoto, J. Appl. Phys. **101**, 033511 (2007).
99 Yu. E. Rogomskaya, Yu. Ya. Tomashpol'skii, Yu. N. Venevtsev, V. M. Petrov, and G. S. Zhdanov, Sov. Phys. JEPT **23**, 47 (1996).
100 M. Mahesh Kumar, V. R. Palkar, K. Srinvas, S. V. Suryanarayana, Appl. Phys. Lett. **76**, 2764 (2000).
101 M. Li, J. L. MacManus-Driscoll, Appl. Phys. Lett. **87**, 252510 (2005).
102 Ch. Binek, A. Hochstrat, X. Chen, P. Borisov, W. Kleemann, and B. Doudin, J. Appl. Phys. **97**, 10C514 (2005); Ch. Binek and B. Doudin, J. Phys.: Condens. Matter **17**, L39 (2005)
103 W. H. Meiklejohn, C. P. Bean, Phys. Rev. **102** 1413 (1956).
104 D. N. Astrov. Sov. Phys. JETP **11**, 708 (1960).
105 I. E. Dzyaloshinskii, Sov. Phys. JEPT **10**, 628 (1960).
106 D. N. Astrov, Soviet Phys. JETP **13**, 729 (1961).
107 V. J. Folen, G. T. Rado, and E. W. Stalder, Phys. Rev. Lett. **6**, 607 (1961).
108 S. Shtrikman and D. Treves, Phys. Rev. **130**, 986 (1963).
109 P. Borisov, A. Hochstrat, X. Chen, W. Kleemann, and Ch. Binek, Phys. Rev. Lett. **94** 117203 (2005).

110 X. Chen, A. Hochstrat, P. Borisov, and W. Kleemann, Appl. Phys. Lett. **89**, 202508 (2006).
111 W. H. Meiklejohn and C. P. Bean, Phys. Rev. **102**, 1413 (1956).
112 M. Kiwi, J. of Magn. Magn. Mater. **234**, 584 (2001).
113 S. Brück, J. Sort, V. Baltz, S. Suriñach, J. S. Muñoz, B. Dieny, M. D. Baro, and J. Nogués, Adv. Mater. **17** 2978 (2005).
114 S. Shtrikman and D. Treves, Phys. Rev. **130** 986 (1963).
115 Y. -H. Chu, L. W. Martin, M. B. Holcomb, M. Gajek, S. -J. Han, Q. He, N. Balke, C. -H. Yang, D. Lee, W. Hu, Q. Zhan, P. -L. Yang, A. Fraile-Rodríguez, A. Scholl, S. X. Wang & R. Ramesh, Nature. Mat., **7** 478 (2008).
116 Marc De Graef and Yimei Zhu, J. of Appl. Phys. **89,** 7177 (2001).
117 D. Lebeugle et al. Appl. Phys. Letts. **92** 022907 (2007).
118 H. Zheng et. al, Science **303**, 661 (2004)
119 [Ch Binek and B. Doudin, J. Phys.: Condens. Matter **17** L39 (2005).